Since 2012

IJAET

International Journal of Automotive Engineering and Technologies

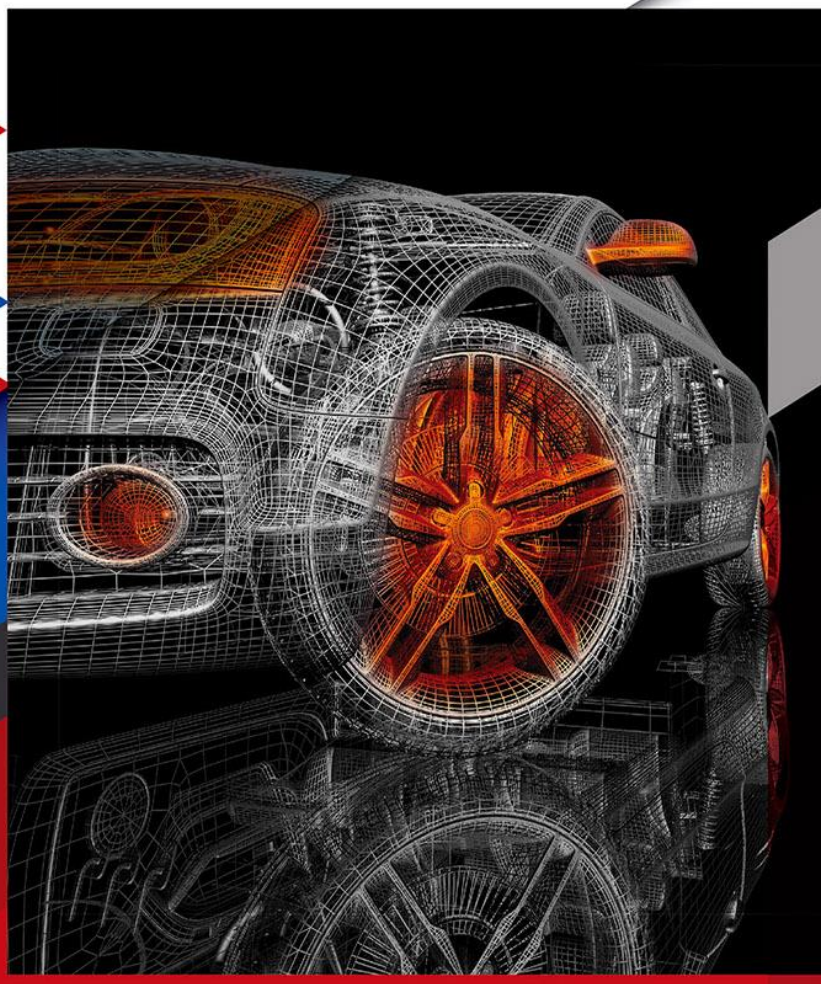

e-ISSN 2146-9067

e-mail: editorofijaet@gmail.com

Editor: Prof. Dr. Murat CİNİVİZ

International Journal of Automotive Engineering and Technologies

e-ISSN: 2146-9067, **Period:** Quarterly

Founded: 2012, **Publisher:** Murat CİNİVİZ

Year : 2024

Volume : 13

Number : 4

https://dergipark.org.tr/tr/pub/ijaet

12.	Prof. Dr. Apostolos PESİRİDİS
13.	Dr. Mohammad AL ZUBİ
14.	Dr. Öğr. Üyesi Fatih AYDIN
15.	Dr. Öğr. Üyesi Mehmet DEMİRALP
16.	Prof. Dr. Tanzer ERYILMAZ
17.	Prof. Dr. Fatih AKSOY
18.	Prof. Dr. Habib GÜRBÜZ
19.	Doç. Dr. Aleksandr KABANOV

Language Editor

1.	DR. Öznur YEMEZ

e-ISSN: 2146 - 9067

International Journal of Automotive Engineering and Technologies

journal homepage:
https://dergipark.org.tr/en/pub/ijaet

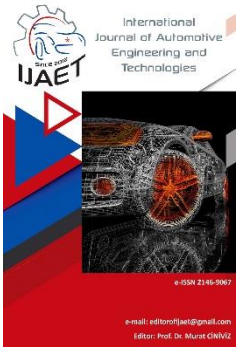

Original Research Article

Impact of turnip biodiesel-diesel blends on engine performance and fuel properties: a comparative analysis

Fatih Aydın[1 *], Hidayet Oğuz[2], Seda Şahin[3], Hüseyin Öğüt[4], Fatma Kayaçetin[5]

[1,2] Necmettin Erbakan University, Faculty of Engineering, Konya, Türkiye.
[3,4] Selçuk University, Faculty of Agriculture, Konya, Türkiye.
[5] Ankara University, Faculty of Agriculture, Ankara, Türkiye.

ARTICLE INFO

Orcid Numbers

1. 0000-0003-4828-0649
2. 0000-0002-0988-1516
3. 0000-0003-1743-9530
4. 0000-0001-8862-8684
5. 0000-0002-7029-2825

Doi: 10.18245/ijaet.1527288

* Corresponding author
fatihaydin@erbakan.edu.tr

Received: Agu 2, 2024
Accepted: Oct 01, 2024

Published: 31 Dec 2024

Published by Editorial Board Members of IJAET

ABSTRACT

The imperative for alternative energy sources has become increasingly evident due to the rising impacts of climate change and greenhouse gas emissions. Biodiesel has emerged as a prominent contender among alternative fuels, offering advantages such as low toxicity, biodegradability, and favorable emission profiles. However, its production faces significant cost burdens, mainly from the expense of vegetable oil. Mustard, with its high oil content in seeds, presents a promising alternative oil source for biodiesel production. This study evaluates the effects of blending biodiesel derived from Brassica rapa ssp. Oil turnip seeds with diesel fuel on fuel properties and engine performance. Transesterification was employed for biodiesel production, and experimental fuels were prepared with varying biodiesel ratios. Engine performance tests, energy analyses, and uncertainty analyses were conducted, revealing a decrease in torque, power, and an increase in specific fuel consumption with higher biodiesel ratios. Energy analysis showed an increase in fuel energy flow with engine speed. Overall, the study contributes to the understanding of Brassica rapa biodiesel production and its application in internal combustion engines.

Keywords: biodiesel, energy analyses, engine performance, diesel engine,fuel properties.

1. Introduction

In contemporary times, the imperative for the development of alternative energy sources has been underscored by the escalating impacts of climate change and the concomitant rise in greenhouse gas emissions. This pressing need is further compounded by the swift depletion of fossil fuel reservoirs [1-2] and the enactment or prospective enactment of legislative measures aimed at curbing vehicular exhaust emissions, prompting numerous scholars to delve into the exploration of alternative fuel utilization modalities [3]. Biodiesel has emerged as a prominent contender among alternative fuels, with blends of biodiesel and diesel fuel garnering significant popularity. Renowned for its applicability in internal combustion engines, biodiesel offers distinct

advantages over other forward-looking alternative fuels owing to its attributes of low toxicity, biodegradability, favorable lubricating properties, and commendable emission profiles [4-5]. However, the production of biodiesel is beset by significant cost burdens, primarily stemming from the production expenses associated with vegetable oil. Notably, the procurement of seeds, constituting 78% of biodiesel production costs, accounts for a substantial portion of the overall expenditure [6]. Predominantly, palm oil (Elaeis oliefera), soybean (Glycine max), sunflower (Helianthus annuus), and rapeseed (Brassica napus) represent the lion's share of global oil production, collectively exceeding 80% [7-8]. These crops, primarily cultivated for alimentary purposes, potentially engender competition between biodiesel production and food provision sectors. Furthermore, the utilization of non-edible oils for biodiesel synthesis is constrained by the indirect impact on food production resultant from the utilization of arable land [3]. Consequently, researchers are increasingly exploring avenues beyond traditional food manufacturing sectors in pursuit of alternative high-quality oil sources for biofuel applications [7-8]. One such promising source is mustard, an ancient spice dating back to antiquity. With a rich historical legacy tracing back 3000 years [9], mustard finds versatile application in both culinary and industrial domains, particularly within the spice and energy sectors. Key species within the mustard genus, including Sinapis alba syn., Brassica alba, S. arvensis syn. B. arvensis, B. juncea, B. rapa syn. B. campestris, and B. nigra, constitute integral components of Turkey's indigenous flora [10]. These species boast diverse compositions, featuring glycosides, arachidic acid, sinabin, lignoceric acid, among other compounds, in their oils. Notably, the pronounced presence of erucic acid renders these oils unsuitable for culinary purposes [11]. Previous investigations have revealed a significantly elevated percentage (25-35%) of seed oil within Turkey's mustard flora [12-14]. In light of these findings, it is evident that mustard holds considerable promise as a viable alternative oil source for biodiesel production. Addressing the burgeoning cost concerns associated with biodiesel manufacturing necessitates innovative approaches that capitalize on the unique attributes of mustard and other non-traditional oil sources, thereby fostering sustainable advancements within the realm of biofuel production. Eryilmaz and Öğüt (2011) [15] conducted a study to examine the performance impacts of various blending ratios of mustard oil biodiesel in a diesel engine. The formulated fuels were evaluated in a four stroke, three cylinders, 60 HP, direct injection diesel engine, and compared with conventional diesel fuel in terms of torque, power, fuel consumption, and smoke density. It was elucidated that the maximum torque for all fuel blends, namely B_{100}, B_{20}, and B_2, was observed at 1200 min^{-1}. The investigations involving diesel, B_{100}, B_{20}, and B_2 blends yielded the highest overall efficiencies of 34.348% at 1300 min^{-1}, 36.103% at 2000 min^{-1}, 36.911% at 1200 min^{-1}, and 34.565% at 1200 min^{-1}, respectively. It was noted that as the blending ratios increased, the exhaust smoke emissions exhibited greater reductions across all engine speeds when compared to conventional diesel fuel. Aysal et al. (2014) [16] examined the impact of biodiesel fuel derived from mustard oil-diesel blends at different proportions on engine performance and exhaust emissions. With increasing biodiesel ratio, there was a decrease in both power and torque output of the internal combustion engine, accompanied by a rise in SFC. Furthermore, comparisons were made among the NO_x and CO emissions of biodiesel, diesel fuels, and biodiesel-diesel fuel blends. It was observed that the emission values of mustard oil biodiesel were lower than those of diesel fuel. Bannikov (2011) [17] investigated the combustion and emission characteristics of biodiesel derived from mustard oil in a single-cylinder, 4-stroke, direct injection, naturally aspirated, 5 kW, air-cooled diesel engine, and compared them with those of diesel fuel. The findings revealed that the utilization of mustard oil biodiesel led to an increase in specific fuel consumption, a decrease in NO_x emissions and smoke density, a slight increase in CO emission, and no significant change in HC emission when compared to diesel fuel. Additionally,

combustion analysis indicated that biodiesel usage resulted in earlier injection initiation, a shortened ignition delay period, a reduction in maximum heat release rate, and cylinder pressure. Yeşilyurt et al. (2019) [18] employed the CCD response surface methodology to optimize biodiesel production from yellow mustard seed oil. The study encompassed 30 experiments aimed at examining the effects of various variables on biodiesel yield. A second-degree polynomial model effectively forecasted the biodiesel yield, achieving a 96.695% yield under the optimized conditions. These findings underscored the efficacy of RSM in maximizing biodiesel yield through the fine-tuning of reaction parameters. Mitrovic et al. (2020) [19] undertook a study highlighting the potential favorable effects of white mustard oil-based biodiesel on sustainable development, akin to other oilseed crops. These effects encompass bolstering energy security, stimulating economic growth, and advocating environmental conservation. Nevertheless, the authors underscored the need for additional research and analysis to conduct a thorough comparison between white mustard oil and alternative feedstocks for biodiesel production.

The primary objective of this study is to evaluate the effects of blending biodiesel derived from Brassica rapa ssp. Oil turnip seeds, specifically the Br-2-Kaan variety candidate, with diesel fuel on fuel properties and engine performance. The central aim of this research is to assess the feasibility and energy efficiency of these biofuel blends. Emphasis is placed on the utilization of Brassica rapa ssp. Oil turnip seeds as an alternative source for biodiesel production. This plant species holds considerable significance due to its widespread presence in Turkey's natural flora and its high oil content in its seeds. The study investigates the impact of biodiesel fuel obtained from this plant on crucial parameters such as engine performance and energy analysis.

The contributions of this study to the field can be delineated as follows:

- It examines the viability of Brassica rapa ssp. oil turnip seeds as a potential alternative oil source for biodiesel production, emphasizing the significance of this plant within the bioenergy sector.
- Through the evaluation of engine performance, it investigates the energy efficiency and environmental ramifications of biodiesel-diesel fuel blends.

By employing methods such as energy analysis and uncertainty analysis, it provides a more comprehensive assessment of the energy balance and efficiency of biodiesel-diesel mixtures.

2. Materials and Method

Transesterification was employed for the production of biodiesel from Brassica Rapa oil at the pilot production facility established at Selçuk University Faculty of Agriculture, Department of Agricultural Machinery and Technologies Engineering [20]. For biodiesel synthesis, a mixture comprising 20% crude Brassica Rapa oil, CH_3OH, and 3.5g NaOH per liter of oil was utilized to generate methoxide. The mixture underwent heating to 55 ºC, followed by the addition of methoxide, and an 8-hour incubation period for glycerol precipitation and subsequent separation. Subsequently, the temperature was raised to 75ºC to eliminate the remaining methyl alcohol from the crude biodiesel. Washing was carried out at 50ºC, with the wash water being separated from the methyl ester. Finally, the drying process at 100ºC yielded biodiesel. Material fuels were prepared by incorporating Brassica Rapa biodiesel at volumetric ratios of 5%, 10%, 20%, and 50% into diesel oil. Diesel fuel sourced from Shell, complying with EN 590 standards, was employed. The properties of the material fuels are comparatively illustrated in detailed in Table 1.

In the experiments, an internal combustion diesel engine with a power of 15 HP and torque of 60 Nm was utilized. The experiments were conducted in accordance with EN 1231 standards to measure specific fuel consumption, torque, and power values. The ester content of the biodiesel produced in this study is determined to be 96.5%.

3. Estimation of Uncertainty and Error Analysis

Uncertainty analysis is used in experimental studies to determine the accuracy and repeatability of data.

Table 1. Measurement results of material fuels

Typical	The Monads	Turnip Oil	B_{100}	D_{100}	$B_{50}D_{50}$	$B_{20}D_{80}$	$B_{10}D_{90}$	B_5D_{95}	Standards	
									EN 14214	ASTM D6751
Density (at 15°C)	g/cm^3	908.5	862.7	827.2	848.9	836.7	830.6	829.7	0.86-0.90	-
Kinematic Viscosity (at 40°C)	mm^2/s	42	5.9	2.9	3.96	3.47	3.26	3.01	3.5-5.0	1.9-6.0
pH	——	5	5	5	5	5	5	5	-	-
CFPP	°C	-12	-4	-11	-6	-7	-8	-9	-	Min. +5
Cloud Point	°C	-10	-1.5	-7.8	-3	-5	-6	-7.1	-	-3 to -12
Pour Point	°C	-15	-16	<-20	<-20	<-20	<-20	<-20	-	-15 to -16
Freezing Point	°C	-17	-18	<-20	<-20	<-20	<-20	<-20	-	-
Calorific Value	Cal/gr	-	9833	11053	10242	10869	10882	10906	-	-
Flash Point	°C	-	130	68	100	80	77	73	≥120	≥130
Water Content	ppm	302.11	173.63	19.64	137.29	109.65	94.61	52.36	≤500	≤500
Color	ASTM	2.7	2.2	0.7	1.7	1.5	1.3	1.2	-	-
Copper Rod Corrosion	——	1a	1a	1a	1a	1a	1a	1a	Class 1	No.3 max.

Thus, it may be possible to identify the sources of uncertainty and to reduce the amount and ratio in the system. It is calculated by Equation of n independent variables (y_1,…, y_n) and uncertainty ratios (z_1, …, z_n). (1) [21, 22].

$$W_R = \left[\left(\frac{\partial R}{\partial y_1} z_1\right)^2 + \left(\frac{\partial R}{\partial y_2} z_2\right)^2 + \cdots\cdots\cdots + \left(\frac{\partial R}{\partial y_n} z_n\right)^2\right]^{1/2} \quad (1)$$

Based on the above equation, the state of the uncertainty ratio equations for the braking power of the motor test setup Eq. (2). Where z_τ and z_n are the uncertainty ratios of the braking torque and engine speed [23].

$$Wp_b = \left[\left(\frac{\partial p_b}{\partial n} z_n\right)^2 + \left(\frac{\partial p_b}{\partial \tau} z_\tau\right)^2\right]^{1/2} \quad (2)$$

Below is a power calculation for D_{100} fuel.

$$P = \frac{n*L*F}{9549}(kW) \quad (3)$$

Moment is measured in Nm. Speed is measured in min^{-1}. Power is measured in watts.

n: 1000 min^{-1} ± 50

P: 7.483 HP = 7.483 / 1.36 = 5.503 kW
L: 0.35 m±0.01

F: 150.135 N ± 0.01

$$\frac{\partial P}{\partial F} = \frac{n*L}{9549} = \frac{1000*0.35}{9549} = 0.037 \quad (4)$$

$$\frac{\partial P}{\partial L} = \frac{n*F}{9549} = \frac{1000*150.135}{9549} = 15.723 \quad (5)$$

$$\frac{\partial P}{\partial n} = \frac{L*F}{9549} = \frac{0.35*150.135}{9549} = 0.006 \quad (6)$$

$$W_P = \sqrt{\begin{bmatrix}(0{,}037)^2 * (0{,}01)^2 \\ +\,(15{,}723)^2 * (0{,}01)^2 \\ +\,(0{,}006)^2 * (50)^2\end{bmatrix}} \quad (7)$$

$$W_p = 0.317$$

$$\%W_p = \frac{W_p}{P} * 100 = \frac{0.317}{5.503} * 100 = 5.75\% \quad (8)$$

The results of uncertainty analysis are given in table 2 for all measurements.
Error Bars give a general idea of how accurate measurement helps to show estimated error or uncertainty. This is done using the notation, the original chart, and the markings drawn on the data points. Error bars are plotted with uncertainty analysis in experiments.

4. Energy Analysis

Combustion process in internal combustion engines; It provides the movement of piston

Table 2. Results of uncertainty analysis

Speed, min^{-1}	Power, %	D_{100}		$B_{50}D_{50}$		$B_{20}D_{80}$		$B_{10}D_{90}$		B_5D_{95}	
		T, %	SFC %	T, %	SFC %	T, %	SFC %	T, %	SFC %	T, %	SFC %
1000	5.759	0.600	0.106	0.606	0.106	0.604	0.106	0.607	0.109	0.575	0.100
1100	5.369	0.624	0.111	0.626	0.112	0.625	0.110	0.627	0.114	0.623	0.113
1200	5.052	0.636	0.116	0.635	0.114	0.627	0.115	0.638	0.118	0.639	0.117
1300	4.791	0.651	0.120	0.656	0.120	0.664	0.125	0.661	0.128	0.662	0.126
1400	4.574	0.676	0.137	0.685	0.131	0.679	0.133	0.684	0.139	0.678	0.131
1500	4.390	0.707	0.154	0.698	0.140	0.699	0.141	0.692	0.150	0.698	0.139
1600	4.234	0.711	0.131	0.725	0.121	0.716	0.122	0.725	0.129	0.721	0.121
1700	4.100	0.743	0.109	0.736	0.111	0.738	0.107	0.760	0.136	0.743	0.106
1800	3.985	0.759	0.108	0.766	0.102	0.759	0.106	0.761	0.104	0.757	0.105
1900	3.884	0.761	0.093	0.779	0.087	0.779	0.094	0.789	0.119	0.777	0.099
2000	3.796	0.804	0.091	0.799	0.088	0.798	0.096	0.806	0.090	0.805	0.090
2100	3.719	0.824	0.083	0.823	0.081	0.820	0.094	0.839	0.091	0.825	0.086
2200	3.651	0.823	0.075	0.829	0.078	0.816	0.084	0.828	0.091	0.829	0.082
2300	3.590	0.842	0.057	0.827	0.050	0.850	0.060	0.837	0.069	0.841	0.070
2400	3.536	0.882	0.037	0.882	0.033	0.891	0.039	0.864	0.044	0.883	0.042

by converting the chemical energy of the fuel into heat energy and converting the heat energy released into mechanical energy in the cylinder [24]. In internal combustion engines, not all of the fuel energy released as a result of the combustion of fuel can be converted into work [25]. Energy analysis gives an idea to calculate energy changes [26].

$$\sum \dot{m}_{in} = \sum \dot{m}_{out} \quad (9)$$

$\dot{m}_{in}$: The inlet mass that consisting of air and fuel

$\dot{m}_{out}$: The outlet mass consisting of exhaust gases

$$\dot{E}_{fuel} = \dot{W} + \dot{Q}_{lost} \quad (10)$$

$\dot{E}_{fuel}$: The fuel energy rate

$\dot{W}$: Brake power

$\dot{Q}_{lost}$: The lost energy rate

$$\dot{E}_{fuel} = \dot{m}_{fuel}.Hu \quad (5)$$

$\dot{m}_{fuel}$: Flow rate (Mass)

Hu : Calorific value (Lower)

The reason for the low calorific value of the fuel in this process is that the water released in the vapor phase at the end of combustion has the maximum combustion temperature [22]. In the literature, the calorific value (lower) of the fuel is used in calculations.

$$\dot{W} = (\tau.n.\pi)/30 \quad (5)$$

5. Result and Discussion

5.1. Engine torque

The variation of torque values in the experiments performed at full load in the use of D_{100}, $B_{50}D_{50}$, $B_{20}D_{80}$, $B_{10}D_{90}$ and B_5D_{95} fuel mixtures is shown in Figure 1. Maximum torque (engine) was measured as 53.723 Nm in D_{100} fuel at 1200 min^{-1}. Comparison to D_{100} fuel, $B_{50}D_{50}$ fuel produced 3.639%, $B_{20}D_{80}$ fuel 3.421%, $B_{10}D_{90}$ fuel 1.481% and B_5D_{95} fuel 0.437% less torque.

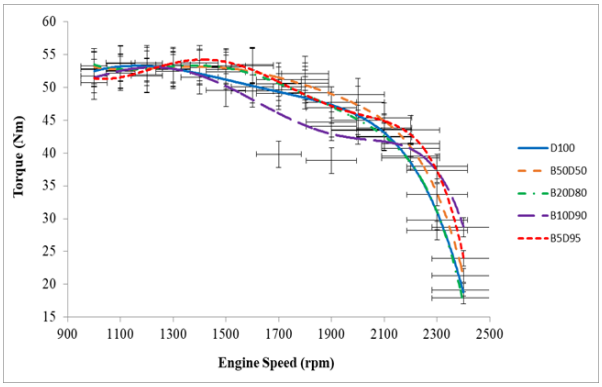

Figure 1. Torque values related to engine speed

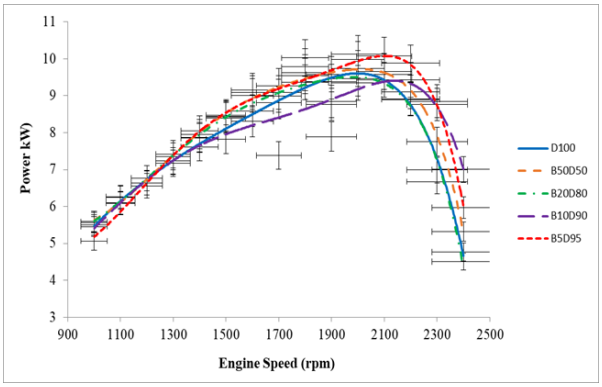

Figure 2. Power values related to engine speed

5.2. Engine power

The variation of power values in the experiments performed at full load in the use

of D_{100}, $B_{50}D_{50}$, $B_{20}D_{80}$, $B_{10}D_{90}$ and B_5D_{95} fuel mixtures is shown in Figure 2. Maximum power (engine) was measured as 10.120 kW in D_{100} fuel at 2000 min^{-1}. Comparison to D_{100} fuel, $B_{50}D_{50}$ fuel produced 7.658%, $B_{20}D_{80}$ fuel 6.511%, $B_{10}D_{90}$ fuel 3.705% and B_5D_{95} fuel 1.442% less power.

5.3. Specific fuel consumption

The variation of fuel consumption (specific) values in the experiments performed at full load in the use of D_{100}, $B_{50}D_{50}$, $B_{20}D_{80}$, $B_{10}D_{90}$ and B_5D_{95} fuel mixtures is shown in Figure 3. Minimum fuel consumption (specific) was measured as 326.425 g/kWh in D100 fuel at 1500 min^{-1}. Comparison to D_{100} fuel, $B_{50}D_{50}$ fuel used 10.475%, $B_{20}D_{80}$ fuel 8.967%, $B_{10}D_{90}$ fuel 7.184% and B_5D_{95} fuel 2.309% more specific fuel consumption.

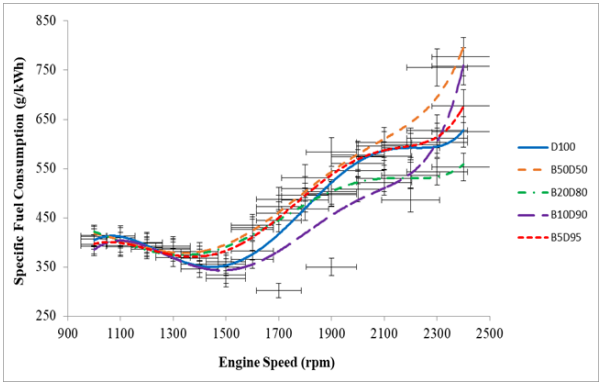

Figure 3. Specific fuel consumption values related to engine speed

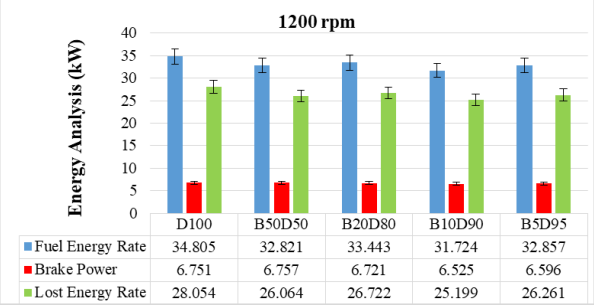

Figure 4. Energy analytics of fuels at a maximum torque of 1200 min^{-1}

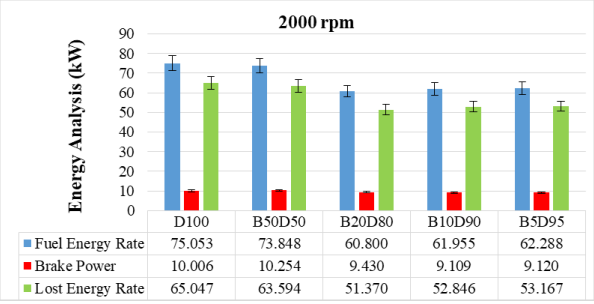

Figure 5. Energy analytics of fuels at a maximum power of 2000 min^{-1}

5.4. Energy analytics

Figure 4 and Figure 5 show the energy analysis results for maximum torque and maximum power cycles of the experiments with material fuels. For all fuels, it was determined that the fuel energy flow increased with the engine speed.

6. Conclusions

In this study, biodiesel production was conducted using Brassica rapa ssp. Oily turnip seeds from the Br-2 (Kaan variety candidate) genotype. The oily turnip obtained from the Br-2 genotype underwent transesterification and was blended with biodiesel at volumetric ratios of 50%, 20%, 10%, and 5%. This resulted in the creation of experimental fuels denoted as D_{100}, $B_{50}D_{50}$, $B_{20}D_{80}$, $B_{10}D_{90}$, and B_5D_{95}, respectively. The fuel properties were examined, and single-cylinder diesel engine performance tests, energy analyses, and uncertainty analyses were performed. The obtained data are presented graphically. In the test results, the maximum torque was measured as 53.723 Nm at 1200 min^{-1} for D_{100} fuel. Compared to D_{100} fuel, $B_{50}D_{50}$ fuel exhibited a 3.639% decrease in torque, while $B_{20}D_{80}$ fuel showed a 3.421% decrease, $B_{10}D_{90}$ fuel displayed a 1.481% decrease, and B_5D_{95} fuel demonstrated a 0.437% decrease. Similarly, the maximum power was measured as 10.120 kW at 2000 min^{-1} for D_{100} fuel. Compared to D_{100} fuel, $B_{50}D_{50}$ fuel showed a 7.658% decrease in power, while $B_{20}D_{80}$ fuel exhibited a 6.511% decrease, $B_{10}D_{90}$ fuel displayed a 3.705% decrease, and B_5D_{95} fuel demonstrated a 1.442% decrease. This trend is attributed to the lower calorific value and higher viscosity of biodiesel, as indicated in Table 1. The decrease in torque and power correlates with the proportion of biodiesel in the blend fuels. The minimum specific fuel consumption in D_{100} fuel at 1500 min^{-1} was measured as 326.425 g/kWh. Compared to D_{100} fuel, $B_{50}D_{50}$ fuel showed a 10.475% increase in specific fuel consumption, while $B_{20}D_{80}$ fuel exhibited an 8.967% increase, $B_{10}D_{90}$ fuel displayed a 7.184% increase, and B_5D_{95} fuel demonstrated a 2.309% increase. This is attributed to the lower heating value of biodiesel compared to

D_{100} fuel, as shown in Table 1. The increase in specific fuel consumption is consistent with the ratio of biodiesel in the blended fuels. Energy analysis results are provided for the maximum torque speed of 1200 min^{-1} and the maximum power speed of 2000 min^{-1} for the experimental fuels. It was observed that as engine speed increased, fuel energy flow increased for all fuels. This is due to the independent nature of the lower calorific values of the fuels relative to engine speed, resulting in an increase in fuel flow rate with engine speed.

In conclusion, the addition of Brassica rapa ssp. biodiesel to diesel fuel at volumetric ratios of 5%, 10%, 20%, and 50% yielded negative results in terms of performance. While these test fuels can be utilized without engine modifications, they are likely to incur losses in engine performance. This study contributes to the literature on Brassica rapa biodiesel production and its application in internal combustion engines.

Credit Authorship Contribution Statement

Fatih Aydın: Formal analysis, original draft, software, supervision, conceptualization, methodology. **Hidayet Oğuz:** Software – methodology, formal analysis. **Seda Şahin:** Software – methodology, formal analysis. **Hüseyin Öğüt:** Software – methodology, formal analysis. **Fatma Kayaçetin:** Software – methodology, formal analysis.

Authors' Conflicts of Interest

There are no financial interests or personal relationships that may have affected the work in this article.

Statement of Industrial Relevance

With this study, It examines the viability of Brassica rapa ssp. oil turnip seeds as a potential alternative oil source for biodiesel production, emphasizing the significance of this plant within the bioenergy sector.

Data availability statement

Authors do not have permission to share data.

Statement of Novelty

The novelty of this study is that Through the evaluation of engine performance, it investigates the energy efficiency and environmental ramifications of biodiesel-diesel fuel blends. By employing methods such as energy analysis and uncertainty analysis, it provides a more comprehensive assessment of the energy balance and efficiency of biodiesel-diesel mixtures.

Acknowledgments

This study was supported by Necmettin Erbakan University, Selçuk University and Ankara University operating in Turkey.

7. References

1. Solmaz, H., Ardebili, S. M. S., Aksoy, F., Calam, A., Yılmaz, E. and Arslan, M., Optimization of the operating conditions of a beta-type rhombic drive stirling engine by using response surface method, Energy, 198, 117377, 2020.
2. Tabanlıgil Calam, T., Investigation of the electrochemical behavior of phenol using 1H-1, 2, 4-triazole-3-thiol modified gold electrode and its voltammetric determination, Journal of the Faculty of Engineering and Architecture of Gazi University, 35 (2), 2020.
3. Solmaz, H., Sürer, E., Yılmaz, E., Calam, A. and İpci, D., Investigation of the effect of carbon nanotube addition to diesel-biodiesel blend on engine performance and exhaust emissions, Journal of the Faculty of Engineering and Architecture of Gazi University, 38 (2), 2023.
4. Khedri, B., Mostafaei, M. and Ardebili, S. M. S., Flow-mode synthesis of biodiesel under simultaneous microwave–magnetic irradiation, Chinese Journal of Chemical Engineering, 27 (10), 2551-2559, 2019.
5. Solmaz, H., Ardebili, S. M. S., Calam, A., Yılmaz, E. and İpci, D., Prediction of performance and exhaust emissions of a CI engine fueled with multi-wall carbon nanotube doped biodiesel-diesel blends using response surface method, Energy, 227, 120518, 2021.
6. Yilmaz, E., Solmaz, H., Polat, S. and Altin, M., Effect of the three-phase diesel emulsion fuels on engine performance and exhaust emissions, Journal of the Faculty of Engineering and Architecture of Gazi University, 28 (1), 2013.
7. Singh, S. and Singh, D., Biodiesel production through the use of different sources and characterization of oils and their esters as

the substitute of diesel: a review, Renewable and sustainable energy reviews, 14 (1), 200-216, 2010.
8. Blume, R. Y., Lantukh, G. V., Levchuk, I. V., Lukashevych, K. M., Rakhmetov, D. B. and Blume, Y. B., Evaluation of potential biodiesel feedstocks: camelina, turnip rape, oil radish and Tyfon, The Open Agriculture Journal, 14 (1), 2020.
9. Kayacetin, F., Botanical characteristics, potential uses, and cultivation possibilities of mustards in Turkey: a review, Turkish Journal of Botany, 44 (2), 101-127, 2020.
10. Babaç, M. T., Possibility of an information system on plants of South-West Asia with particular reference to the Turkish plants data service (TUBIVES), Turkish Journal of Botany, 28 (1), 119-127, 2004.
11. Wendlinger, C., Hammann, S. and Vetter, W., Various concentrations of erucic acid in mustard oil and mustard, Food chemistry, 153, 393-397, 2014.
12. Tonguc, M. and Erbaş, S., Evaluation of fatty acid compositions and some seed characters of common wild plant species of Turkey, Turkish Journal of Agriculture and Forestry, 36 (6), 673-679, 2012.
13. Kayacetin, F., Önemli, F., Yilmaz, G., Kinay, A., Hatipoğlu, H., Kivilcim, M. N., Nimet, K., Arzu, K. and Sefaoğlu, F., Effect of row spacing on yield, yield components and crude oil of autumn and spring sowed mustard (Sinapis arvensis L.) in eight locations of Turkey, Journal of Agricultural Sciences, 24 (4), 471-487, 2018.
14. Kayaçetin, F., Önemli, F., Yilmaz, G., Khawar, K. M., Kinay, A., Hatipoğlu, H., Kivilcim, M. N., Nimet, K., Arzu, K. and Sefapğlu, F., Growing degree day and seed yield relationships in mustard (Brassica Juncea L.) under different sowing seasons and locations of Turkey, Journal of Agricultural Sciences, 25 (3), 298-308, 2019.
15. Eryilmaz, T. and Öğüt, H., The effect of the different mustard oil biodiesel blending ratios on diesel engines performance, Energy Education Science and Technology Part A-Energy Science and Research, 28 (1), 2011.
16. Aysal, F. E., Aksoy, F., Şahin, A., Aksoy, L. and Yıldırım, H., Optimization of Biodiesel Production from Mustard Oil and Engine Performance Tests, Afyon Kocatepe University Journal of Science and Engineering, 14 (2), 1-9, 2014.
17. Bannikov, M., Combustion and emission characteristics of Mustard biodiesel, 6th International Advanced Technologies Symposium (IATS'11), Turkey, 1-5, 2011.
18. Yeşilyurt, M.K., Arslan, M. and Eryılmaz, T., Application of Response Surface Methodology for The Optimization of Biodiesel Production from Yellow Mustard (Sinapis Alba L.) Seed Oil, International Journal of Green Energy, 16.1: 60-71, 2019.
19. Mitrovic, P.M., Stamenkovic, O.S., Bankovic-Ilic, I., Djalovic, I.G., Njezic, Z.B., Farooq, M., and Veljkovic, V.B., White Mustard (Sinapis alba L.) Oil in Biodiesel Production: A review. Frontiers in Plant Science, 11, 299, 2020.
20. Öğüt, H.,Akınerdem, F., Pehlivan, E., Aydın, M.E. and Oğuz, H., Investigation of biodiesel production processes from some oil crops in Turkey and its use in diesel engines in terms of agriculture, environment, food, chemistry and technology: DPT Project No:2004/7 Bioenergy 2004 Symposium, İzmir/Türkiye, 2004.
21. Holman J.P., Experimental methods for engineers, Eighth edition, New York, USA. McGraw-Hill Series in Mechanical Engineerring, 2012.
22. Öğüt H., Oğuz H. and Aydin F., Experimental analysis of energy, performance and noise emissions for biodiesel fuel obtained from animal waste fat, Environmental Progress and Sustainable energy, 41(5):e13847, 2022.
23. Kul, B.S. and Ciniviz, M., An evaluation based on energy and exergy analyses in SI engine fueled with waste bread bioethanol-gasoline blends, Fuel, Volume 286, 119375, 2021.
24. Sayın, B., An Experimental Study on Energy and Exergy Analysis for a Diesel Engine Using Bio-Fuel, Ms thesis, Selçuk University, Konya, 2014.
25. Boles, M.A. and Çengel, Y. A., Thermodynamics: An Engineering Approach, Fifth Edition, McGraw-Hill, New York, USA, 2006.
26. Abedin, M.J., Masjuki, H.H., Kalam,

M.A., Sanjid, A., Rahman, S.M.A. and Mssum, B.M., Energy Balance Of Internal Combustion Engines Using Alternative Fuels, Renewable and Sustainable Energy Reviews, 26, Pages 20-33, 2013.

e-ISSN: 2146 - 9067

International Journal of Automotive Engineering and Technologies

journal homepage:
https://dergipark.org.tr/en/pub/ijaet

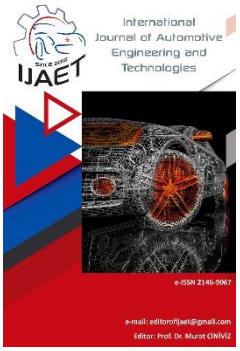

Original Research Article

Modeling the aerodynamic performance of unmanned aerial vehicle (UAV) propellers with multifidelity method

Hakan Ünsal[1, *], Mesut Düzgün[2]

[1,* 2] Gazi Üniversitesi, Fen Bilimleri Enstitüsü, Otomotiv Mühendisliği, Ankara, Türkiye.

ARTICLE INFO

Orcid Numbers

1. 0000-0002-9896-9877
2. 0000-0003-0582-4183

Doi: 10.18245/ijaet.1485834

* Corresponding author
nermaux97@gmail.com

Received: May 17, 2024
Accepted: Oct 16, 2024

Published: 31 Dec 2024

Published by Editorial Board Members of IJAET

ABSTRACT

In this study, an artificial neural network (ANN) based method is discussed to determine the aerodynamic performance of propellers used for Unmanned Aerial Vehicles (UAVs). Here, wind tunnel test data was used to obtain data for propellers without test data. First, wind tunnel test data was converted to a specific format using Python and modeling was done using ANN. With this modeling process, it was seen how close the model obtained with artificial neural networks produced results to the data obtained from wind tunnel tests. This study allows for more precise analysis of the aerodynamic performance of UAV propellers and optimization of their design. This approach provided a very accurate modeling of the aerodynamic performance of UAV propellers and took an important step towards determining the performance of propellers without wind tunnel test data. The obtained data constitutes a valuable resource for optimizing the design and performance of UAVs.

Keywords: Unmanned Aerial Vehicles (UAV), Propeller, Artificial Neural Network, Modeling, Internal-Combustion Engine.

1. Introduction

Wind tunnel tests and simulations play an important role in evaluating the design and performance of UAVs. Wind tunnel tests are used to determine the aerodynamic properties of the UAV and optimize its performance. Additionally, thanks to simulations, different flight scenarios can be modeled and the behavior of the UAV can be predicted. One of the important elements affecting the aerodynamic performance of UAVs is propellers. Propellers enable the UAV to stay in the air by converting the power produced by the engine into thrust force. Therefore, the aerodynamic design of propellers must be done carefully, considering factors such as efficiency and noise. During the propeller selection process of unmanned aerial vehicles (UAV), a detailed analysis is made using various methods and techniques. The basis of these analyzes are research and testing methods such as computer-aided design (CAD), fluid dynamics (CFD) analyses, artificial neural networks, machine learning, flight tests and wind tunnel experiments [1]. Artificial neural networks and machine learning techniques are used to predict and

optimize propeller performance. These technologies, which have the ability to learn from complex datasets, enable more precise and efficient results in propeller design. Flight tests are important to verify propeller performance in real-world conditions and optimize the design. In these tests, the UAV is flown in different weather conditions and altitudes to evaluate its propeller performance [6]. Finally, wind tunnel tests are also used in the propeller selection process. In these experiments, the aerodynamic properties of UAV propellers are tested in different wind conditions and their performance is evaluated [3]. Integration of these various methods is critical in determining the optimal propeller design and ensuring optimum performance of the UAV. In this study, artificial neural networks and machine learning applications were preferred to determine the aerodynamic behavior of UAV propellers. Technologies such as artificial neural networks and machine learning play an important role in simulations and data analysis. Artificial neural networks are artificial intelligence models capable of learning from complex datasets. Machine learning, on the other hand, is based on the ability of algorithms to learn from datasets and recognize patterns. These technologies are used to obtain more precise results in UAV design and performance analysis and in determining the aerodynamic behavior of propellers. In order to determine the aerodynamic performance of propellers for unmanned aerial vehicles, datasets will be compared using artificial neural networks and methods will be followed to obtain data representing the real environment. The focus is on integrating wind tunnel test data of UAV propellers and thus achieving the closest result to reality.

2. Literature Review

Gamble, investigated the effects of Reynolds number on propeller performance in this study. It was found that the geometric features of the propeller, such as shape, twist, and blade chord, are highly dependent on Reynolds number. In wind tunnel tests, propellers produced by APC, which include glass-filled epoxy for high torsional strength, were used [1].

Figure 1. APC Propeller [1]

Figure 1 shows a propeller belonging to the APC propeller. APC 18x12 and APC 18x8 propellers were tested at 7 different rotation speeds for different Reynolds numbers ranging from 400,000 to 502,000 and 1,080,000 to 1,213,000 respectively. It has been found that efficiency, thrust coefficient, power coefficient and slope increase when the number of Reynolds increases. It was determined that the efficiency of the APC 18x12 propeller increased by 5% by increasing the Reynolds number from 400,000 (1,700 rpm) to 1,155,000 (4850 rpm). It can be seen that the same thrust force is produced at lower speeds as the pitch is reduced while the diameter is kept constant. In other words, as the pitch or pitch/diameter ratio increases, efficiency increases, and the propeller produces thrust at higher advance rates. In conclusion, experimental results show that Reynolds number has a strong effect on small propellers. Therefore, the designer must take the Reynolds number into account.

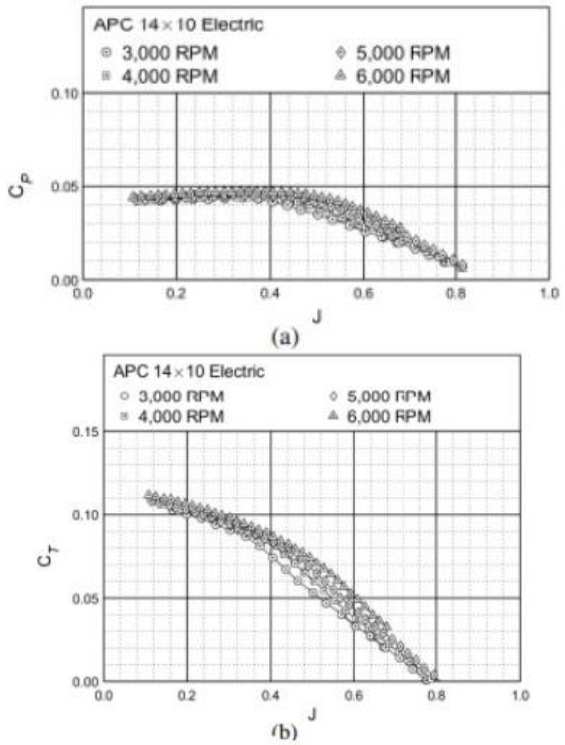

Figure 2. Wind Tunnel performance of APC 14×10 Thin Electric Propeller: (a) Thrust coefficient (Ct), (b) Power coefficient (Cp) [2]

Dantsker and colleagues observed from wind tunnel performance tests that, for a given

propeller diameter, as the pitch angle increases, the thrust, power, and efficiency coefficient curves shift upwards and to the right. Figure 2 shows the Ct and Cp values of the 14x10 APC propeller as they vary according to the Advance Ratio from the wind tunnel test results. This observation indicates a trend where, as the advance ratio of a propeller increases, the thrust, power, and efficiency coefficients tend to have higher values, which is an expected general trend. It should be noted that for propellers with high diameter and pitch ratio, the performance curves are incomplete due to the 80 ft/s speed limit set by the propeller balance cover's structural design. Similarly, it is expected that, for a given propeller diameter, increasing the pitch angle will result in higher static (zero-speed) thrust and power coefficients. This study focuses on how propellers behave under different conditions in real-world environments [2]. The Blade Element Momentum (BEM) model is presented and used for performance predictions of sUAS propellers. Several corrections have been proposed for the BEM model to capture the unique characteristics of rotating flow in low Reynolds number propellers. Notably, corrections such as the use of aerodynamic databases produced by XFOIL, stall corrections, Mach corrections, and the inclusion of the model's angular flow components are included. For the specific propeller geometries addressed in this study, the BEM model predictions follow the expected general trends for fixed-pitch propellers. The BEM model has been validated through a series of wind tunnel tests, and positive comparisons have been made between the predicted and measured theoretical trends.

In Figure 3, part (a) presents the relationship between Ct, which likely represents a thrust coefficient, and J across different configurations: "10x5," "10x6," and "10x7." Both analytical (solid lines) and experimental (markers) results are shown for each configuration. The analytical results are represented by continuous lines, with each color indicating a different blade or propeller type. The experimental data, depicted with error bars, generally aligns well with the analytical curves but shows more variance. In part (b), the relationship between Cq, likely a torque coefficient, and J is illustrated for the same configurations. The torque coefficients (Cq) values are lower than those of thrust coefficients (Ct), suggesting that the torque coefficient is smaller in magnitude. While the analytical and experimental trends are similar, the experimental data appears to have a larger error margin. Overall, both graphs demonstrate that the analytical models generally match the experimental data, although there are some discrepancies and variations, indicating that experimental conditions or modeling assumptions may have impacted the results.

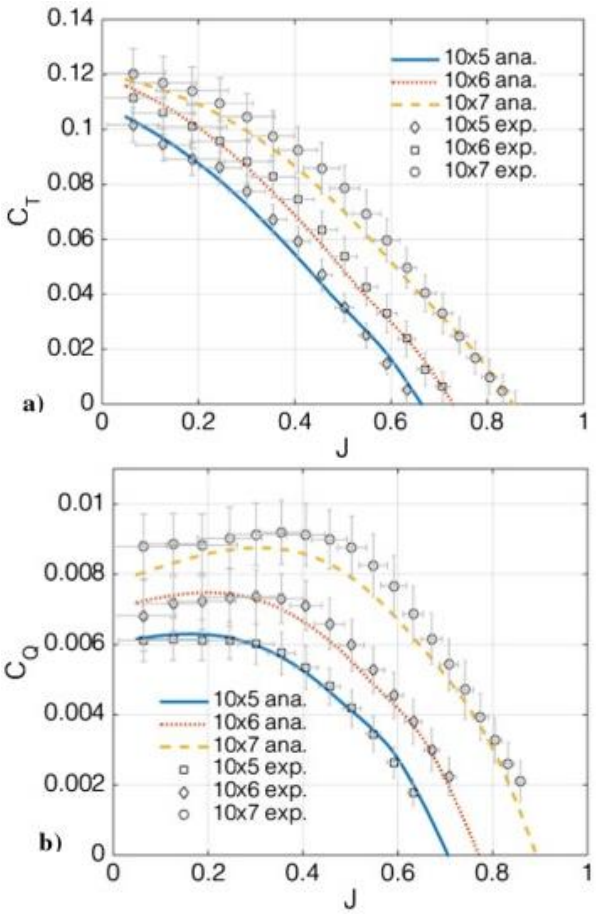

Figure 3. Figure Analytical and experimental (a) thrust coefficients (Ct), (b) torque coefficients (Cq) for APC Propeller [3]

McCrink and colleagues found similar results in their full-power tests to those reported in previous studies on small-scale propellers. A new constant Reynolds number test was introduced to demonstrate the scaling effects on propeller efficiency. Comparisons between experimental and model-based performance measurements highlight the importance of including Reynolds number dependence in the

analysis of small-scale thrust systems. The presented and validated BEM model is highly useful for propeller design for sUAS, especially since the operating Reynolds numbers of these propellers are low, where viscous effects are predominantly significant. Additionally, the general power model for sUAS thrust systems enables high-fidelity vehicle performance predictions for sUAS and determination of vehicle performance during flight tests and routine operations [3].

In his study, Bağçe, determined the performance of mini aircraft propellers through static and dynamic tests. A propeller testing setup was designed and assembled to evaluate the static performance of the propellers. This setup was also placed inside a wind tunnel. In the static tests, thrust, power, and efficiency values for four different Turbotek propellers were obtained as a function of propeller rotational speed. These data were compared with the calculation results from Turbotek, Computational Fluid Dynamics (CFD) analysis, and the static test results. In the dynamic tests, the variation of thrust coefficient, power coefficient, and efficiency values of these four Turbotek propellers as a function of advance ratio was obtained. The experimental results were compared with the analytical and CFD results provided by Turbotek, and the experimental results were found to be successful [4].

Demirhan analyzed the fuel consumption performance of a commercial aircraft using an artificial neural network model. The data were modeled using a feedforward neural network and trained with high-accuracy simulation data (operational flight plans). Subsequently, real flight data from the Quick Access Recorder (QAR) were used to adjust the model's hyperparameters. Ten models with the least errors were selected and tested with a portion of the QAR data. After a statistical comparison among these ten models, the best model was chosen. Finally, a classification process for flights with fuel consumption prediction errors exceeding the three-sigma limit was described. Although the model was created using only five key parameters (takeoff weight, air distance, average cruise Mach number, altitude parameter, and fuel mileage deviation), it demonstrated a high level of accuracy. Additionally, the study proposes an additional method for identifying abnormal fuel consumption [5].

In Figure 4, a propeller motor setup within a wind tunnel is shown. This setup is used to test the aerodynamic performance of the propeller. The large fan at the end of the tunnel generates airflow through the tunnel, allowing for analysis of the propeller's effects. Most UAVs use propellers operating at low Reynolds numbers ranging from 50,000 to 100,000. Although sufficient data for these propellers are lacking, the performance of propellers for larger aircraft is well-documented. Therefore, in this study, tests were conducted at the University of Illinois, Urbana-Champaign, where the performance of 79 propellers with diameters ranging from 9 to 11 inches was determined, and static thrust measurements were taken. The subsonic wind tunnel at the University of Illinois, Urbana-Champaign, is reported to have a rectangular cross-section of 2.8 x 4.0 ft (0.853 x 1.219 m) and a maximum flow speed of 160 mph (71.53 m/s) [6].

Figure 4. Wind Tunnel Used for Propeller Testing [6]

Whitmore and colleagues (2012) revisit and enhance the classical first-order design tool known as the Blade Element Momentum (BEM) theory. Blade element theory analyzes a propeller blade by dividing it into segments and evaluating each element individually. In Figure 5, the relationship between the advance ratio and both the thrust coefficient and the power coefficient is shown. In part (a), the thrust coefficient is compared across test data, Analytical BEM, and Nonlinear BEM models. The test data, displayed with error bars, generally aligns well with both models, though there is a slight divergence at higher advance ratios. In part (b), the power coefficient is

similarly compared, indicating good agreement between the test data and both models. However, slight discrepancies appear as the advance ratio increases. Overall, both graphs demonstrate that the Analytical and Nonlinear BEM models accurately capture the trends in the test data, with minor deviations at higher advance ratios. However, blade element theory alone lacks the capability to predict the inflow velocity required to complete the flow field of the propeller. By combining blade element and momentum theories, a combined low-order prediction tool known as the Blade Element Momentum (BEM) theory is created. The BEM theory uses momentum theory to calculate the local induced velocity and incorporates this information into the blade element model. The conventional method used to close the nonlinear BEM equations involves a small local angle of attack and assumptions of low local induced drag across all sections as proposed by McCormick. McCormick also assumes that the amount of local induced drag negligibly reduces the local propeller thrust coefficient. While these assumptions allow for a closed-form solution, they are known to be inaccurate at high advance ratios and for the inner radius of the blade. This paper presents a nonlinear solution method that avoids these flawed and simplifying assumptions and offers a general improvement over known analytical methods for the BEM model. Calculations using two BEM solution methods are compared with wind tunnel test data collected for a small radio-controlled (RC) aircraft propeller. The solution methods are compared, and it is shown that the traditional linear solution predicts propeller performance with high accuracy, especially at high advance ratios [7].

Hang Zhu and colleagues (2021) present an analysis of a model to calculate the requirements and aerodynamic performance of propellers for rotorcraft unmanned aerial vehicles (UAVs). Based on blade element momentum theory, the aerodynamic forces on a blade element are examined and utilized. The symbolic NACA0012 airfoil model is used as an example to validate the model's accuracy. An experimental system designed and constructed to test the aerodynamic

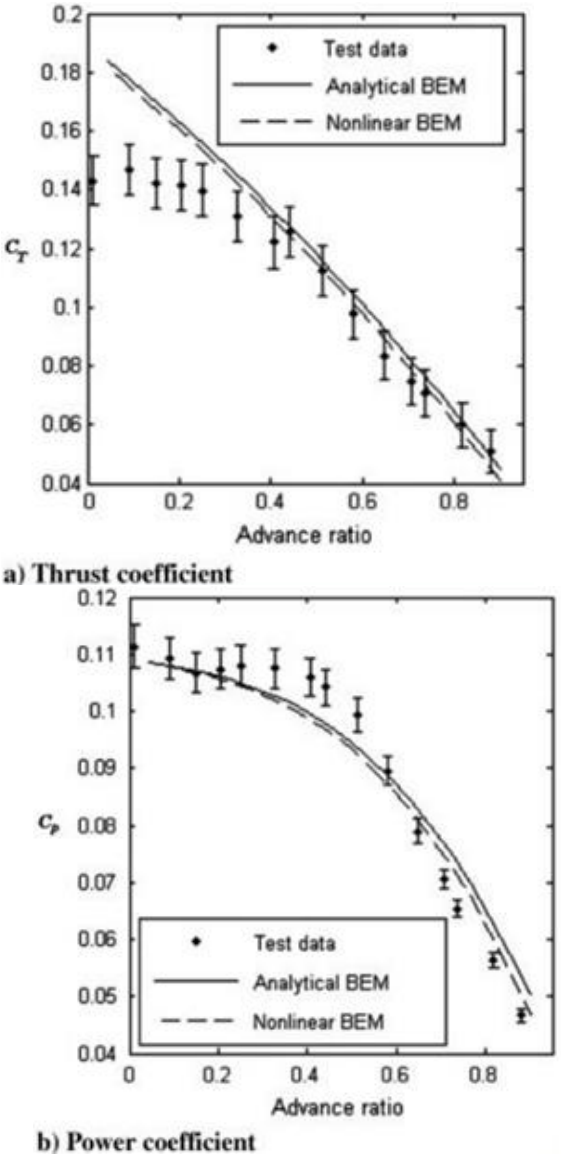

Figure 5. Comparisons of a) Thrust Coefficient (Ct) and b) Power Coefficient (Cp) for the APC 8x8 Thin Electric Propeller [7]

performance of propellers is used to evaluate six different types of APC propellers. Additionally, data processing software is developed to perform single-step calculations of three propeller parameters (airfoil drag power, induced velocity, and efficiency) for plotting aerodynamic graphs. The results of the experiment show that the thrust and torque of the propeller increase with rotational speed, propeller diameter, and pitch. The newly developed system and software provide more precise torque measurements and greater stability under current experimental conditions. Experimental data, including propeller speed, thrust, and torque, are used to analyze the aerodynamic performance of APC propellers. The chosen propeller type for the

experiment is one of the most commonly used for UAVs, making the experimental data more convincing for assisting in propeller selection for UAVs [8].

In their 2021 study, Zbigniew Czy and colleagues investigate the impact of propeller geometry on the aerodynamic performance of propellers. In Figure 6, the Thrust/Power ratio is shown for different PWM ratios. One of the factors affecting propeller performance is the propeller pitch. This parameter indicates the distance a propeller will advance during one rotation. The key aspect is to determine the pitch at which the propeller performance is optimal. In this study, the aerodynamic performance of propellers with different pitches is tested using a wind tunnel, and experimental results are obtained. The tests were conducted in a subsonic wind tunnel. As a result of the study, the values of dimensionless coefficients for thrust force, torque, power, efficiency, and thrust-to-power ratio were calculated. The results allow for the selection of the most suitable solution when these coefficients are used as criteria. It is shown that there is a decrease in the force produced per unit power at higher airflow speeds; however, high-pitch propellers were observed to perform better at higher airflow speed ranges [9].

Onay and colleagues (2012) compared the design, analytical-based analysis results, and performance test results of two propellers intended for unmanned aerial vehicles (UAVs). In Figure 7, the comparison of results obtained through BEM and experimental methods for the XOAR 26x12 propeller is shown. Dynamic tests of the two UAV propellers were conducted in a wind tunnel and compared with the results of the Blade Element Momentum (BEM) analysis. The study revealed that the results obtained from Computational Fluid Dynamics (CFD) closely matched the BEM analysis results. This indicates that the BEM analysis method can be used for propeller optimization [10].

In their 2024 study, Xiaojing Wu and colleagues investigated the efficiency of electric propulsion systems used in unmanned aerial vehicles (UAVs).

The study highlights the conflict between accuracy and design efficiency in optimization designs when using Computational Fluid Dynamics (CFD) and Propeller Theory methods. To address this, the study introduces a high-accuracy artificial neural network-based optimization framework for electric aircraft propellers.

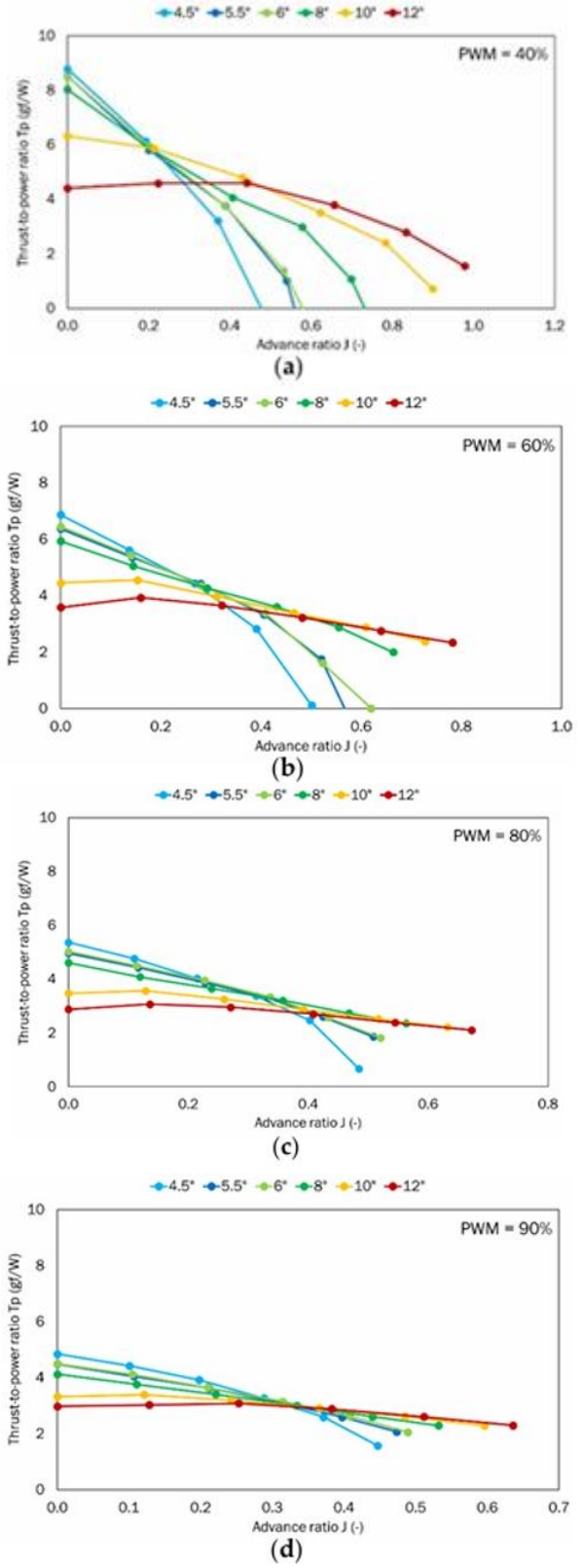

Figure 6. Thrust-to-Power Ratio as a Function of Advance Ratio for the Tested Propeller Set at Different PWM Values: (a) 40%; (b) 60%; (c) 80%; (d) 90% [9].

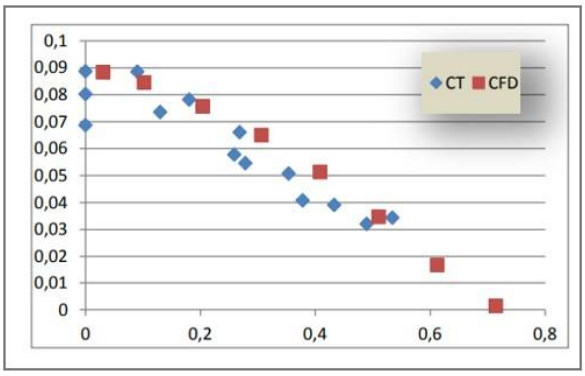

Figure 7. Comparison of Thrust Coefficient (Ct) Values Obtained Experimentally and with the Blade Element Momentum (BEM) Analysis Method for the XOAR 26x16 Propeller [10]

This method is based on high-accuracy CFD numerical simulations and combines low-order Blade Element Momentum Theory (BEMT) knowledge with fewer CFD simulations to achieve higher model accuracy. This method improves the propeller's cruising efficiency from a point of 82.3% designed by CFD and BEMT to 87.1% using the newly employed method. It has been shown that this method offers advantages in optimization effectiveness and efficiency compared to single-order optimization approaches [11].

3. Applications

Obtaining a Wind Tunnel Data Set

Propeller tests were conducted in the UIUC low-turbulence subsonic wind tunnel. The wind tunnel is an open-return type with a 7.5:1 contraction ratio. Here, many variable sizes and pitches of the APC propeller were tested. These tests were carried out by changing many parameters such as RPM and Speed of the propellers. As a result of these tests, UIUC has compiled the wind tunnel test results into a test data set and shared it with the companies using this propeller.

Artificial Neural Network Model

The Artificial Neural Network (ANN) model is a model generally used in the fields of machine learning and artificial intelligence. ANN is a computational model inspired by the functioning of biological neural networks and is used to solve various complex problems. In this study, the artificial neural network (ANN) model will be established with wind tunnel data. Here, the artificial neural network model will be taught wind tunnel test data of propellers of different sizes and different pitch combinations, and as a model output, it will be aimed to predict propeller combinations without wind tunnel test data with the help of the wind tunnel test data model. Here, while the model is being established, changes will be made to the model according to the state of learning the test data of the model, and the most optimum artificial neural network model will be found.

Creating Wind Tunnel Models

Thrust coefficients (Ct) and Power coefficients (Cp) values were arranged before creating the model according to the variable RPMs in different propeller diameters and pitch combinations in the Wind Tunnel data set. This data Set is divided into Ct/Cp for "Sport" type propeller wind tunnel and Ct/Cp for "Thin Electric" type propeller wind tunnel. Before creating wind tunnel models, the data will be examined and the necessary data editing procedures for the models have been carried out. For the use of APC propellers in the modeling of propellers with variable diameter and pitch combinations tested in the wind tunnel, there are actual test data in the wind tunnel regarding 30 different diameter and pitch combinations of the "Sport" propeller type propellers between 1000 RPM and 10000 RPM. In addition, there are actual test data performed in the wind tunnel on propellers of the "Thin Electric" propeller type, in the range of 1000 RPM and 10000 RPM, in 34 different diameter and pitch combinations. These data are arranged so that the "Sport" and "Thin Electric" type propeller data are side by side in the format "RPM J V Ct Ct_Predited Cp Cp_Predicted Typed p".

APC Propeller Sport Type Data Set Ct (Thrust Coefficient) Prediction Model Creation

With the wind tunnel data set, first a model will be created using the wind tunnel data set for the "Sport" type propeller. Before creating the model, the independent variables to be used in the training process of the model were determined. These variables are the X_train dataset. "RPM J Predicted_Ct Diameter Pitch V" values will be used for the x_train data set. These values are the features given as input to

the model and help the model estimate the Ct value for the wind tunnel by using these features. The reason why these values were chosen as x_train is that these values are the main factors that determine propeller performance. RPM (number of revolutions), J (advance coefficient), Diameter (diameter), Pitch (pitch) and V (speed) are important features that directly affect the performance of the propeller. It is important for the model to learn these factors that determine the estimated Ct value. Y_train training set is the dependent variable that the model tries to learn during the training process. So, Ct will be used for y_train. While determining the hyperparameters of the model, different combinations were used, and the models were tested. In this way, the parameters were finalized by trial-and-error method. The hyperparameters used for the Wind Tunnel "Sport" type propeller Ct prediction model are as follows:

- 5 Layers
- 1 Input Layer, 3 Layers, 1 Output Layer
- Batch Size 16
- 1000 Epochs,
- 256 Neurons in layers except Output Layer
- Mean Squared Error (MSE) Loss Function
- ReLU Activation Function
- Adam Optimization Algorithm
- Standard Scaler
- Validation (X_test, y_test)
- Test Size 1%

With these determined parameters, the artificial neural network (ANN) model for the wind tunnel was trained.

For the artificial neural network (ANN) model created for wind tunnel Ct prediction, the number of layers and the number of neurons in the layer were adjusted to be the most optimum values at which the model would perform best, based on previous studies and trial and error method. According to the created model "Epochs" values, the point at which the model performs best will be determined. Accordingly, the “Epochs” value will be determined.

When the loss function and R2 performances of the models are examined according to 2 different "Epochs" values, Model 1 has lower loss function performance and R2 score. This shows that Model 1 performs better. When evaluating the number of "Epochs", it is seen that there is no need for more "Epochs" values since the performance of the model is quite good for 1000 "Epochs".

Table 1. Wind Tunnel “Sport” Ct Sequential Model Structure

Wind Tunnel “Sport” Ct Sequential Model		
Layer (type)	**Output Shape**	**Parameter**
Dense	252	1764
Dropout	252	0
Dense	168	42504
Dropout	168	0
Dense	84	14196
Dropout	84	0
Dense	42	3570
Dropout	42	0
Dense	1	43
Total Parameter = 62077		Trainable Parameter = 62077

Table 2. Comparison of model performances according to Wind Tunnel Ct Forecast Model “Epoch” Values according to Loss functions and R2 method

Model No	**1**	**2**
Model Type	Wind Tunnel “Sport” Ct Forecast Model	Wind Tunnel “Sport” Ct Forecast Model
Epochs	1000	2000
MAE	0.032211390	0.056139356
MSE	0.001689722	0.0077393565
RMSE	0.17947532	0.2369374517
R^2	0.99833180	0.993742881

When the Loss-Validation Loss graphs are examined in Figure 8, it is seen that the Loss and Validation Loss values overlap at 1000 "Epochs". In this case, it appears that the model is not overfit. The fact that the loss values encountered during the training of the model are low and stable shows that the model works well in both the training and validation phases. This helps predict that the model can give good results against new data. When the graphics are evaluated, model 1 will be preferred for the wind tunnel Ct prediction model since the model performance shows good performance for 1000 "Epochs" value. Model 1 will be trained with the wind tunnel data set.

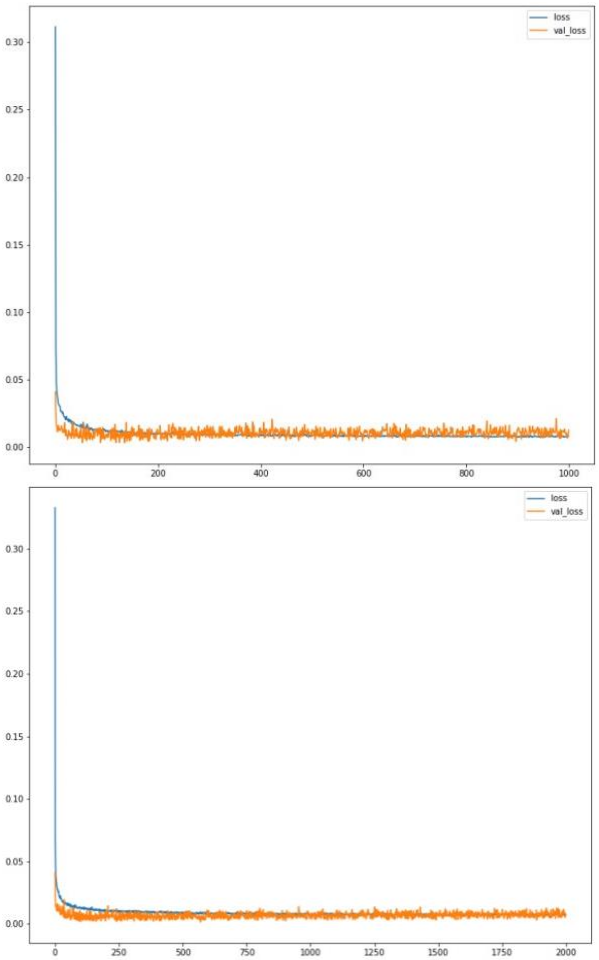

Figure 8. Wind Tunnel "Sport" Type Propeller Ct Forecast Model (top) 1000 "Epoch" and (bottom) 2000 "Epoch" (Blue - Loss, Orange - Validation Loss)

APC Propeller Sport Type Data Set Ct (Thrust Coefficient) Prediction Model Training and Outputs

After the hyper parameters and "Epochs" value determined for the wind tunnel Ct prediction model, the artificial neural network (ANN) model was trained with the data set.

When the "Predictions-Real Values" graph in Figure 9 is examined, it is seen that the graph shows a linear relationship. This shows that the model's predictions are quite close to the actual values and the performance of the model is very good. The fact that the points are regularly distributed around the ideal line shows the consistency of the model predictions and that the model has learned the data set well in general. Using an artificial neural network (ANN) model, the performance of the model was evaluated with the data set.

When the performance of the wind tunnel "Sport" Ct prediction model is examined, it is seen that the performance of the model is almost the same as the real data set. Here, it is predicted that the predicted performance of the model is good and that it will make a good prediction for different propeller combinations.

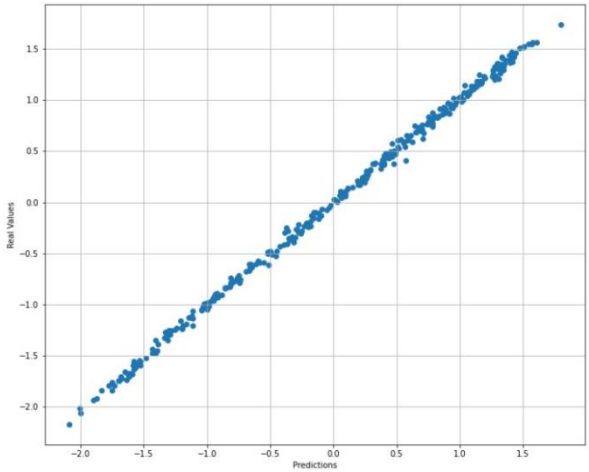

Figure 9. Wind Tunnel "Sport" Ct Forecast Model Predictions-Real Values

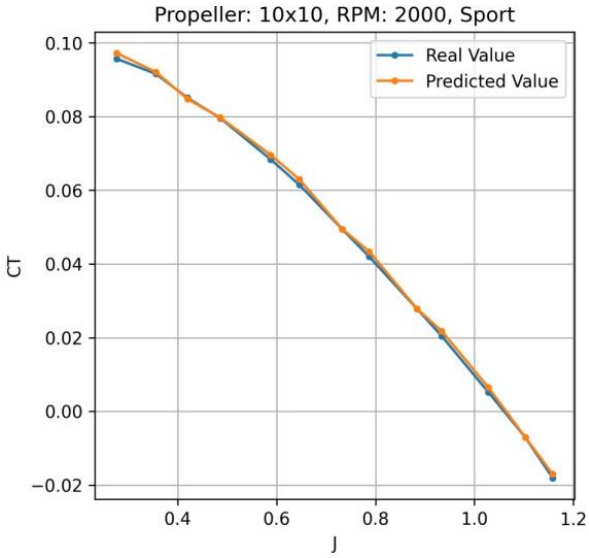

Figure 10. Wind Tunnel "Sport" Type Propeller Ct Forecast Model 10x10 Propeller 2000 RPM Model Performance

APC Propeller Sport Type Data Set Cp (Power Coefficient) Prediction Model Creation

Wind tunnel data set was used to create the wind tunnel "Sport" Cp prediction model. While creating the model and determining the model parameters, the previously created wind tunnel model was taken as reference. The hyperparameters used for the Wind Tunnel "Sport" type propeller Cp prediction model are as follows:

- 5 Layers
- 1 Input Layer, 3 Layers, 1 Output Layer

- Batch Size 4
- 500 Epochs,
- 256 Neurons in layers except Output Layer
- Mean Squared Error (MSE) Loss Function
- ReLU Activation Function
- Adam Optimization Algorithm
- Standard Scaler
- Validation (X_test, y_test)
- Test Size 1%

The determined parameters were determined based on the variables according to the prediction performance of the model and the Loss-Validation Loss graph. A neural network (ANN) model was trained according to these hyperparameters

Table 3. Wind Tunnel "Sport" CP Sequential Model Structure

Wing Tunnel "Sport" Cp Sequential Model		
Layer (type)	Output Shape	Parameter
Dense	252	1764
Dropout	252	0
Dense	168	42504
Dropout	168	0
Dense	84	14196
Dropout	84	0
Dense	42	3570
Dropout	42	0
Dense	1	43
Total Parameter = 62077		Trainable Parameter = 62077

The artificial neural network (ANN) model structure created for wind tunnel Cp prediction was created based on previous models. In order for the model to give the best performance, different "Epochs" values were tested for the established model structure.

Models trained with different "Epochs" values were examined. Among these Examined models, Model 1 has the lowest MSE and the highest R2. This shows that Model 1 performs better than other models. Since the models performed very well according to the examined "Epochs" values, the number of "Epochs" was limited to 2000 for comparison. When the Loss-Validation Loss graphs of the models for different "Epochs" values are examined, it appears that the graphs show almost similar behavior. Although the Loss and validation Loss values of the graph with an

Table 4. Comparison of model performances according to Wind Tunnel Cp Forecast Model "Epoch" Values according to Loss functions and R2 method

Model No	**1**	**2**	**3**
Model Type	Wind Tunnel "Sport" Ct Forecast Model	Wind Tunnel "Sport" Ct Forecast Model	Wind Tunnel "Sport" Cp Forecast Model
Epochs	500	1000	2000
MAE	0.03589336	0.05087223	0.043748091
MSE	0.002298777	0.00520541	0.00403422
RMSE	0.189455449	0.225548752	0.20916044
R^2	0.997517669	0.99659612	0.996350194

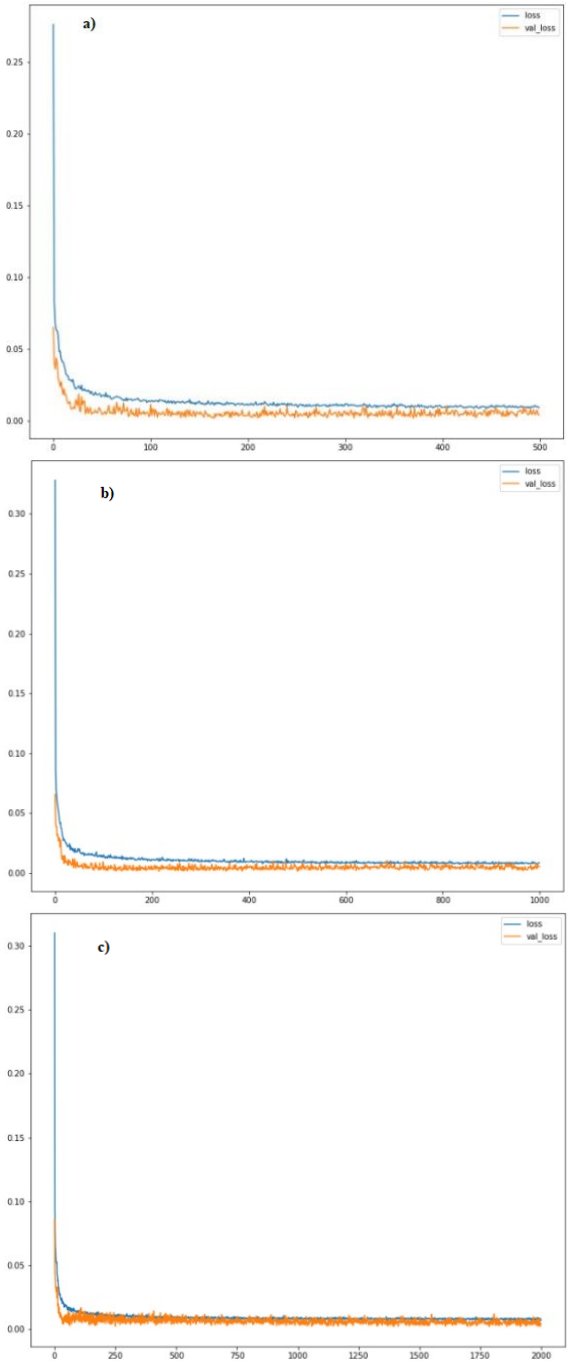

Figure 11. Wind Tunnel "Sport" Type Propeller Cp Prediction Model a) 500 "Epoch" and b) 1000 "Epoch" c) 2000 "Epoch" (Blue - Loss, Orange - Validation Loss)

"Epochs" value of 500 in Figure 11 do not overlap completely, this does not matter in terms of the performance of the model. Because the loss and validation loss values do not overlap, it generally indicates that the model can generalize well and is not overfitting. This shows that the model does not overfit the training data and can perform well with new data. When the Loss-Validation Loss graphs are examined, as well as the loss function performances and R2 results of the models, it can be seen that the model that performs well is Model 1, Model 1 will be trained for the wind tunnel "Sport" Cp prediction model.

APC Propeller Sport Type Data Set Cp (Power Coefficient) Prediction Model Training and Outputs

The Cp prediction model, which will be created using the wind tunnel data set, was trained with the artificial neural network (ANN) model data set after the determined hyperparameters and "Epochs" value.

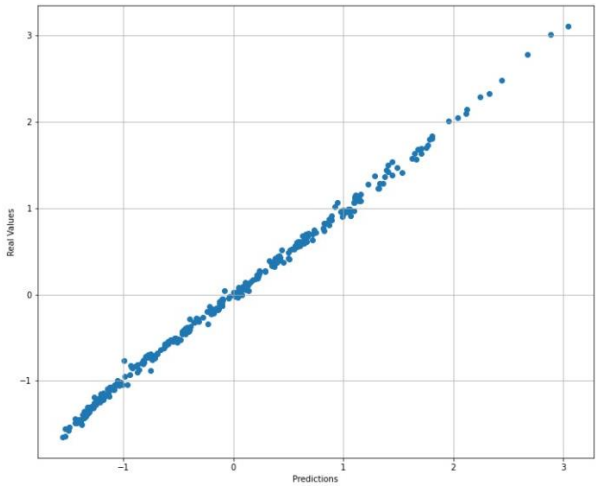

Figure 12. Wind Tunnel "Sport" CP Forecast Model Predictions-Real Values

When the Predictions-Real Values graph in Figure 12 is examined, it shows that the model and its predictions are consistent according to the behavior of the points in the graph, and that the model has learned the data set well in general. With the model trained with the wind tunnel data set, the performance of the model was examined according to propeller and RPM values in different combinations.

When the prediction ability of the model is examined, it is seen that the Cp predictions make a close prediction to the values in the data set according to the variable J (Advance ratio) values.

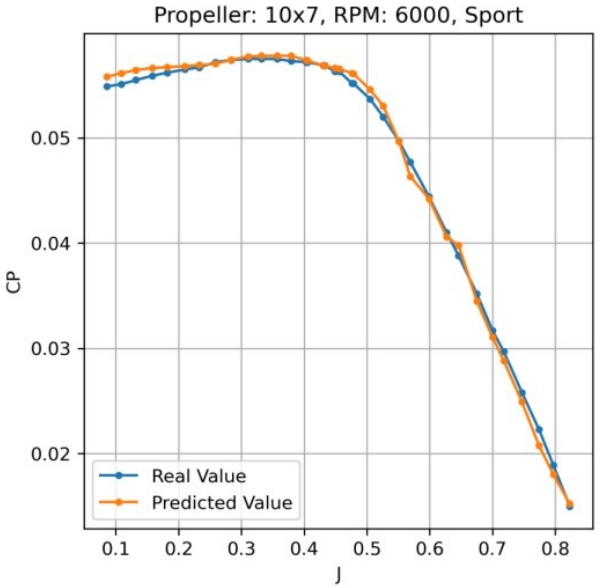

Figure 13. Wind Tunnel "Sport" Type Propeller CP Forecast Model 10x7 Propeller 6000 RPM Model Performance

APC Propeller Thin Electrical Type Data Set Ct (Thrust Coefficient) Prediction Model Creation

While creating the "Thin Electric" type propeller Ct prediction model, wind tunnel data set was initially used. Previous wind tunnel models were taken as a basis in the process of establishing the model and determining its parameters. The initial hyperparameters determined for the "Thin Electric" type propeller Ct prediction model are as follows:

- 5 Layers
- 1 Input Layer, 3 Layers, 1 Output Layer
- Batch Size 4
- 500 Epochs,
- 256 Neurons in layers except Output Layer
- Mean Absolute Error (MAE) Loss Function
- ReLU Activation Function
- Adam Optimization Algorithm
- Standard Scaler
- Validation (X_test, y_test)
- Test Size 1%

Artificial neural network (ANN) model structure will be established with the determined parameters. According to these parameters, the artificial neural network (ANN) model will be trained. Parameters can

be changed according to the performance of the model.

Table 5. Wind Tunnel "Thin Electric" Ct Sequential Model Structure

Wing Tunnel "Thin Electric" Ct Sequential Model		
Layer (type)	Output Shape	Parameter
Dense	252	1764
Dropout	252	0
Dense	168	42504
Dropout	168	0
Dense	84	14196
Dropout	84	0
Dense	42	3570
Dropout	42	0
Dense	1	43
Total Parameter = 62077		Trainable Parameter = 62077

The model structure was determined by reference to previous models. It has been observed that models previously trained in this determined structure showed high prediction performance. The number of "Epochs" that would give the best performance with this model structure was determined by trial and error method.

Table 6. Comparison of model performances according to Wind Tunnel "Thin Electric" Ct Estimation Model "Epoch" Values according to Loss functions and R2 method

Model No	**1**	**2**
Model Type	Wind Tunnel "Thin Electric" Ct Forecast Model	Wind Tunnel "Thin Electric" Ct Forecast Model
Epochs	500	1000
MAE	0.03377714	0.04106794
MSE	0.0018278	0.00286244
RMSE	0.18378559	0.20265226
R^2	0.99827756	0.9974655550

The performance of models trained according to different "Epochs" values was compared. When comparing between two models, the model with lower error values is generally considered better. Therefore, in this case, it can be seen that the MAE, MSE, RMSE and R values of Model 1, which has a value of 500 epochs, are lower. Since the model learned the data set with good performance even at low Epochs numbers, there was no need for high Epochs values.

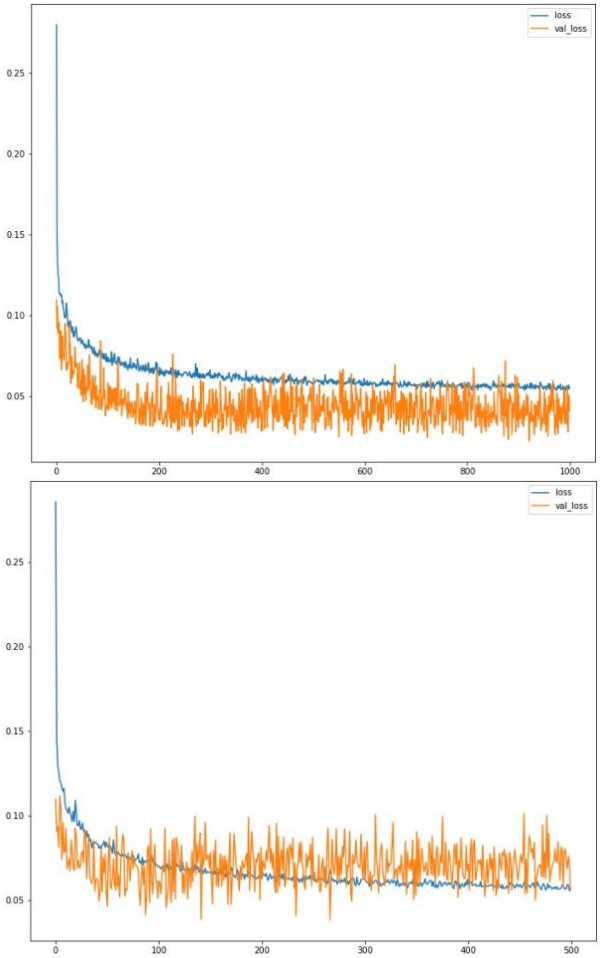

Figure 14. Wind Tunnel "Thin Electric" type propeller Ct Prediction Model (left) 500 "Epoch" and (right) 1000 "Epoch" (Blue - Loss, Orange - Validation Loss)

When the Loss-Validation Loss graphs are examined, it appears that the Loss values and Validation Loss values show similar behavior. Although these behaviors are not very stable compared to other models, the data set learning performance of the models is quite good. When the graph of the model with an "Epochs" value of 500 is examined in Figure 14, it is seen that the model generally shows a good learning performance during the training process and there is no overfitting problem. Since the difference between training and validation losses is small, it can be said that the model generalizes well to both training data and unvalidated data. However, the fluctuation of training loss indicates that the learning rate may be too high, or some training examples are forced by the model. But in general, it seems that the predicted performance of the model will be good. Model 1, that is, the model with an "Epochs" value of 500, will be preferred for training with the data set.

APC Propeller Thin Electric Type Data Set Ct (Thrust Coefficient) Prediction Model Training and Outputs

The model will be trained using the wind tunnel data set using the created model structure and the determined hyperparameters. After the artificial neural network (ANN) model is trained with the training data set, the performance of the model will be examined.

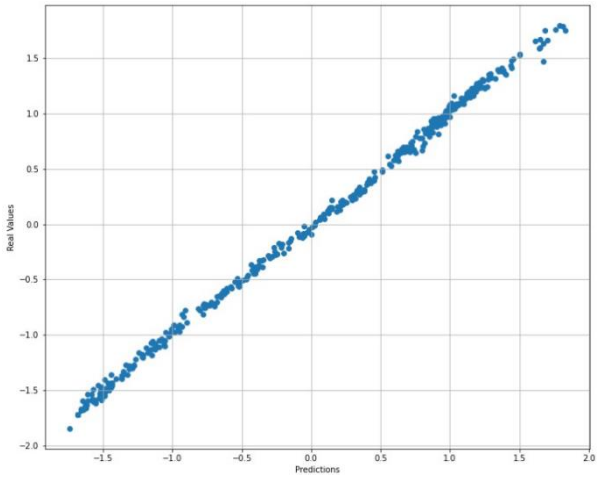

Figure 15. Wind Tunnel "Thin Electric" Ct Forecast Model Predictions-Real Values Graph

When you look at the Predictions-Real Values graph in Figure 15, you can see that there is a clear linear relationship in the graph. This indicates that the predictions of the model are very close to the real values and the performance of the model is quite good and the model performs well in learning the data set. The prediction performance of the artificial neural network (ANN) model trained with the data set was examined.

Model prediction performance is very close to real data. The model performance output shows that the model can predict well both the propeller combinations in the data set and the propeller combinations not in the data set

APC Propeller Thin Electrical Type Data Set Cp (Power Coefficient) Prediction Model Creation

While creating the wind tunnel "Thin Electric" Cp prediction model, previous wind tunnel prediction models were taken as reference. Wind tunnel "Thin Electric" data set was used as the data set. For the wind tunnel "Thin Electric" Cp artificial neural network (ANN) prediction model, the following hyperparameters were determined for the model.

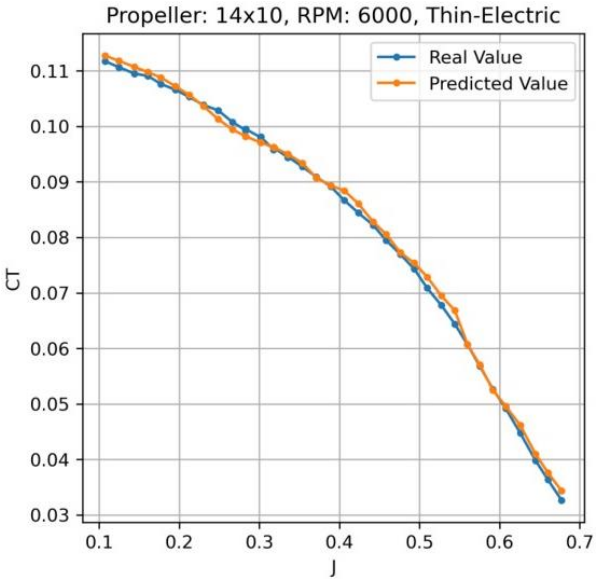

Figure 16. Wind Tunnel "Thin Electric" Type Propeller Ct Forecast Model 14x10 Propeller 6000 RPM Model Performance

- 5 Layers
- 1 Input Layer, 3 Layers, 1 Output Layer
- Batch Size 16
- 1000 Epochs,
- 256 Neurons in layers except Output Layer
- Mean Absolute Error (MAE)Loss Function
- ReLU Activation Function
- Adam Optimization Algorithm
- Standard Scaler
- Validation (X_test, y_test)
- Test Size 1%

Artificial neural network (ANN) model structure will be established according to the determined parameters. This model structure was created based on the structure of artificial neural network (ANN) models created with previously good performing simulation and wind tunnel data sets.

It has been observed that the number of layers and neurons is sufficient for previously created artificial neural network (ANN) models. Therefore, there was no need for more layers and number of neurons in the wind tunnel "Thin Electric" Cp prediction model structure. With the created model structure, the model will be trained with different "Epochs" values. "Epochs" values will be determined by trial and error method according to the prediction performance of the model.

Table 7. Wind Tunnel "Thin Electric" Cp Sequential Model Structure

Wind Tunnel "Thin Electric" Cp Sequential Model		
Layer (type)	Output Shape	Parameter
Dense	252	1764
Dropout	252	0
Dense	168	42504
Dropout	168	0
Dense	84	14196
Dropout	84	0
Dense	42	3570
Dropout	42	0
Dense	1	43
Total Parameter = 62077		Trainable Parameter = 62077

Table 8. Comparison of model performances according to Wind Tunnel Cp Forecast Model "Epoch" Values according to Loss functions and R2 method

Model No	**1**	**2**
Model Type	Wind Tunnel "Thin Electric" Cp Forecast Model	Wind Tunnel "Thin Electric" Cp Forecast Model
Epochs	500	1000
MAE	0.0309182	0.030591069
MSE	0.00173574	0.00196366
RMSE	0.17498080	0.17490302
R^2	0.99818197	0.99820711

With the created model structure, the performance of the model was examined for different "Epochs" values. It is seen that the model performs well when training the model with a low number of "Epochs". So there is no need for more Epochs values. In Figures 17 and 18, the models trained with 500 and 1000 "Epochs" values are compared. When these two models are examined, it is seen that the models perform very close to each other when the loss function performance and R2 score are examined. Although the R2 performance of the 2nd model is very close, it is higher, so the 2nd model was preferred to train the prediction model.

Loss-Validation When the loss graphs are examined, it is seen that the graph of the 2nd model shows a generally good learning performance in the process of learning the data set. 2. When the Loss-Validation Loss graph of the model is examined, it is seen that the Loss and Validation Loss values do not increase, so there is no overfitting problem. Since the difference between the training and validation losses of the model is small, it can be said that the model generalizes well to both training data and unvalidated data. Considering the loss function performance, R2 score and Loss-Validation Loss graph for the wind tunnel "Thin Electric" Cp prediction model, it was decided to train the 2nd Model, which has a value of 1000 "Epochs", with the data set and use it as the prediction model.

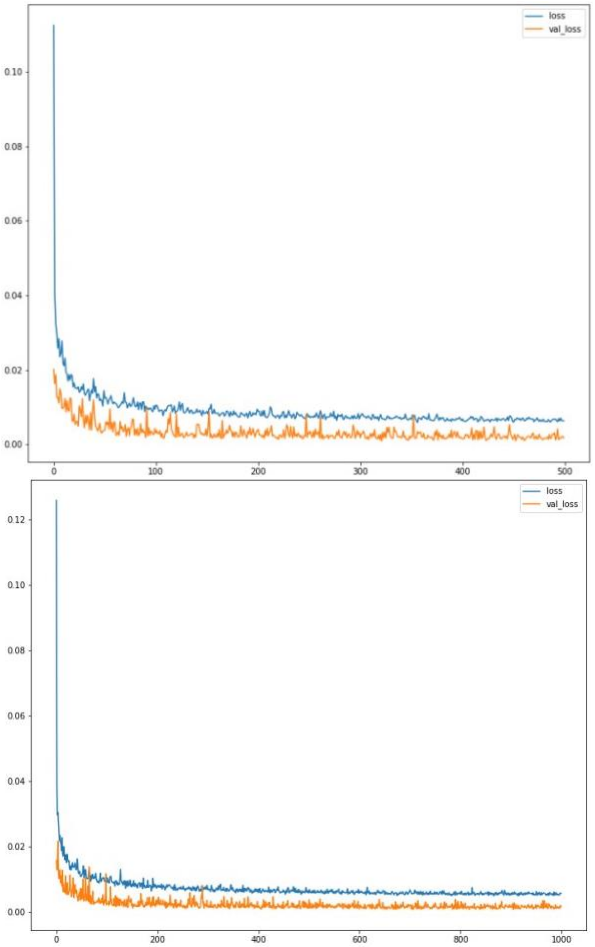

Figure 17. Wind Tunnel "Thin Electric" Type Propeller Cp Prediction Model (left) 500 "Epoch" and (right) 1000 "Epoch" (Blue - Loss, Orange - Validation Loss)

APC Propeller Thin Electric Type Data Set Cp (Power Coefficient) Prediction Model Training and Outputs

After the hyperparameters and "Epochs" value of the model were determined, the model was trained with the wind tunnel data set. After the artificial neural network (ANN) model was trained, the prediction performance of the model was examined.

When the Predictions-Real Values graph in Figure 18 is examined, it is seen that there is a

linear and linear relationship between the prediction and real values.

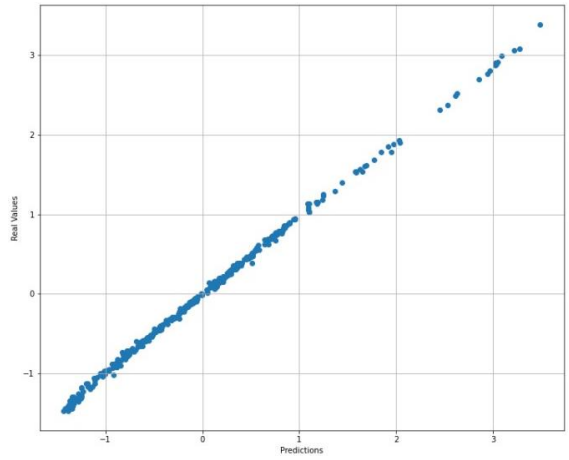

Figure 18. Wind Tunnel "Thin Electric" Cp Forecast Model Predictions-Real Values Graph

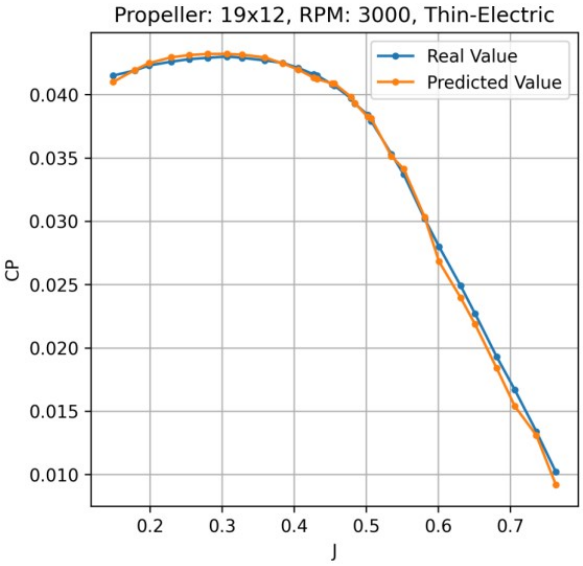

Figure 19. Wind Tunnel "Thin Electric" Type Propeller Cp Forecast Model 19x12 Propeller 3000 RPM Model Performance

This relationship shows that the model has a good performance in learning the data set well. The prediction performance of the artificial neural network (ANN) model trained with the data set was examined.

When the prediction performance of the model is examined, it is seen that it performs well between the real data and the predicted data according to different RPM values and different propeller combinations. The performance of the model in predicting the real data in the data set and the data not in the data set is very good and gives results very close to reality. This model will be used for the wind tunnel "Thin Electric" Cp prediction model.

Comparison of Wind Tunnel Artificial Neural Network Models

Four artificial neural network (ANN) models were created using the wind tunnel data set. These created wind tunnel models will help find Ct (Thrust Coefficient) and Cp (Power Coefficient) for different RPM values of propeller combinations that do not have wind tunnel test data without going to the wind tunnel.

When the four artificial neural network (ANN) models created are examined, it is seen that error metrics such as MAE, MSE and RMSE are at a very low level. These metrics show that the model's predictions are quite close to the actual values. Additionally, the R2 score is very close to 1 in 4 models. This means that the models fit the data set very well and their predictions exactly match the real values.

4. Conclusion

This study explores an approach that utilizes artificial neural networks and machine learning methods to determine the aerodynamic performance of propellers. The primary goal is to estimate the thrust and power values that different propeller combinations will produce without relying on wind tunnel data. The analyses demonstrate that artificial neural networks and machine learning models can accurately model the aerodynamic performance of propeller combinations without wind tunnel data.

Table 9. Artificial Neural Network (ANN) Models for "Sport" and "Thin Electric" type propellers created using the Wind Tunnel dataset and Simulation Forecast dataset

Model type	Epochs	MAE	MSE	RMSE	R^2
Wind Tunnel "Sport" Ct Forecast Model	1000	0.032211390	0.001689722	0.17947532	0.99833180
Wind Tunnel "Sport" Cp Forecast Model	500	0.03589336	0.002298777	0.189455449	0.997517669
Wind Tunnel "Thin Electric" Ct Forecast Model	500	0.03377714	0.0018278	0.18378559	0.99827756
Wind Tunnel "Thin Electric" Cp Estimation Model	1000	0.030591069	0.00196366	0.17490302	0.99820711

This provides a significant advantage by reducing dependence on wind tunnel testing and speeding up the design process. In this study, four different wind tunnel models were created, all of which produced results very close to real-world conditions. The results obtained from the models of propellers with wind tunnel data are very close to the true value of 1, with all four models yielding values that are 99.8% close to the actual value. This indicates how well the models align with reality. These models can accurately predict the thrust (Ct) and power (Cp) coefficient values of propellers without wind tunnel test data. This success is based on the effective use of artificial neural networks and machine learning methods. The results obtained show that these techniques can be successfully applied in the process of modeling the aerodynamic performance of propellers.

5. Suggestions and Evaluations

The artificial neural network models used in this study exhibit similarities to those found in the literature. However, these models can exhibit different behaviors depending on the dataset. Upon examining the models and datasets in the literature, it is observed that the average accuracy rate of the models in this study is 99.9%, which surpasses the accuracy capabilities of all models previously reported in the literature. The findings of this study are significant for accelerating the design process and reducing costs by decreasing reliance on wind tunnel testing. While wind tunnel testing can typically take months, the artificial neural network models used here can provide high-accuracy test data in seconds. Additionally, accurately predicting the thrust and power values of propeller combinations is considered a crucial step in UAV design and optimization. These results suggest that artificial neural networks and machine learning techniques are valuable tools for analyzing and optimizing the aerodynamic performance of propellers.

Nomenclature

UAV : Unmanned Aerial Vehicle
ANN : Artificial Neural Network
CFD : Computational Fluid Dynamics
APC : Propeller Brand
Cp : Power Coefficient
Ct : Thrust Coefficient
BEM : Blade Element Momentum Theory
UAS : Unmanned Aircraft System
CQ : Torque Coefficients
QAR : Quick Access Recorder
RC : Radio Controlled
PWM : Pulse Width Modulation
UIUC : University of Illinois at Urbana-Champaign
MSE : Mean Squared Error Loss Function
MAE : Mean Absolute Error Loss Function
RMSE: Root Mean Squared Error Loss Function
J : Advance Ratio

6. References

1. Dustin Eli Gamble., Automated dynamic propeller testing at low Reynolds numbers, Master of Science Thesis, Oklahoma State University, ProQuest LLC, UMI number: 1474037, 2010.
2. Dantsker, O.D., Caccamo, C., Deters, R.W., and Selig, M.S., "Performance Testing of APC Electric Fixed-Blade UAV Propellers," AIAA Aviation and Aeronautics Forum and Exposition (Aviation 2022), AIAA Paper 2022-4020, Chicago, IL, June 2022.
3. McCrink, M.H. and Gregory, J.W., "Blade Element Momentum Modeling for Low-Re Small UAS Electric Propulsion Systems," AIAA Aviation and Aeronautics Forum and Exposition (Aviation 2015), AIAA Paper 2015-3296, Dallas, TX, June 2015.
4. Bağçe, M., Design and performance evaluations of the propeller of a UAV, Middle East Technical University, Institute of Science, Department of Mechanical Engineering, 2015.
5. Demirhan, O., Identification of the abnormal fuel consumption in a commercial flight by an artificial neural network surrogate model, Middle East Technical University, Institute of Science, Department of Aeronautics and Astronautics Engineering, 2022.
6. Brandt, J.B., Selig, M.S., Propeller Performance Data at Low Reynolds Numbers 49th AIAA Aerospace Sciences Meeting, 4-7, Orlando, FL, AIAA 2011-1255, January 2011.
7. Whitmore, S.A., Merrill, R. S., Nonlinear Large Angle Solution of the Blade Element Momentum Theory Propeller Equations, Utah University, Journal of Aircraft, Vol.49, No.4, Doi:10.2514/1.C

031645. p1126, July 2012.
8. Hang Zhu, Zihao Jiang, Hang Zhao, Siyu Pei, Hongze Li, and Yubin Lan, "Aerodynamic Performance of Propellers for Multirotor Unmanned Aerial Vehicles: Measurement, Analysis, and Experiment" Research Article, School of Mechanical and Aerospace Engineering, Jilin University, Changchun 130025, China, Hindawi Shock and Vibration Volume, Article ID 9538647, 11 pages, 2021. https://doi.org/10.1155/2021/9538647
9. Zbigniew Czyż, Pawel Karpiński, Krzysztof Skiba, "Experimental study of propellers for the electric propulsion system" 2021 IEEE 8th International Workshop on Metrology for AeroSpace (MetroAeroSpace), 2021.
10. Oğuz Kaan Onay, Javid Khalilov, Yashar Ostovan, Ali Ruhşen Çete," İnsansız hava aracı pervanelerinin tasarım, analiz ve test yeteneklerinin geliştirilmesi", IV. Ulusal havacılık ve uzay konferansı UHUK, Hava Harp Okulu, İstanbul, 12-14 Eylül 2012.
11. Xiaojing Wu, Zijun Zuo, Long Ma, Weiwei Zhang, "Multi-fidelity neural network-based aerodynamic optimization framework for propeller design in electric aircraft ", Research Article, Northwestern Polytechnical University, Xi'an, 710072, PR China, 2024.

e-ISSN: 2146 - 9067

International Journal of Automotive Engineering and Technologies

journal homepage:
https://dergipark.org.tr/en/pub/ijaet

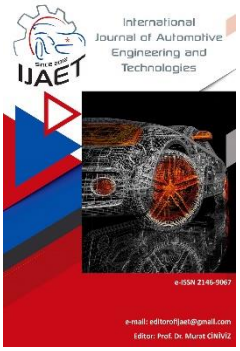

Original Research Article

IoT based a low cost battery monitoring system using ESP8266 and Arduino IoT cloud platform

Mustafa Aydın[1, *], İsmail Gürbüz[2]

[1,* 2] Pamukkale University, Faculty of Technology, Automotive Engineering Department, Kınıklı Campus, Denizli, Türkiye.

ARTICLE INFO

Orcid Numbers

1. 0000-0002-6187-6722
2. 0000-0002-1762-9388

Doi: 10.18245/ijaet.1553298

* Corresponding author
mustafa_aydin@pau.edu.tr

Received: Sep 20, 2024
Accepted: Oct 16, 2024

Published: 31 Dec 2024

Published by Editorial Board Members of IJAET

ABSTRACT

It is crucial to ensure the longevity of batteries in electric and hybrid vehicles in order to solidify their position in the market. Monitoring the life, capacity, and health of battery pack has become a major concern for users. The proper functioning and long-term durability of electric and hybrid vehicle batteries depend on accurately assessing their properties. In this study, a 6S battery module was created using NCR18650PF 3300mAh 3.7 V Li-ion batteries, which are increasingly used in electric and hybrid systems. Battery voltage, current, and surface temperature data of the battery module were collected during 500 charge-discharge cycles. Obtained charge-discharge profile, retainable capacity change rates, and the health and charge status of the battery were processed. The collected data showed the expected decrease in charge discharge profiles as documented in the literature. Upon reaching 500 charging cycles, the maintainable capacity of the battery module decreased by 70% compared to its initial state, indicating that the battery module had reached the end of its life. A program was developed using the Arduino IoT cloud system based on the charge-discharge profile and sustainable capacity change data obtained from battery characteristics. The predictions for battery health and state of charge based on the collected sensor data were processed and transferred to the interface in a way that allowed the end user to visualize it. The battery SOC, SOH, temperature, charge-discharge current, and terminal voltage data were displayed in the mobile application via the Arduino IOT Cloud platform with the ESP8266 Arduino card during daily use of the battery module. As a result, a successful module that can provide IoT communication on a lithium-ion battery pack was obtained. Thanks to the developed module, the expected life of the lithium-ion battery pack can be monitored even remotely, as long as it is connected to the internet.

Keywords: Battery State of Health, Battery State of Charge, Electric Vehicle, IoT Cloud, ESP8266.

1. Introduction

Over the years, the use of fuel-fueled vehicles has been a major factor in increasing air pollution on the planet. The emissions released

by fuel vehicles increase the formation of greenhouse gases, causing the hole in the ozone layer to deteriorate. Climate change on the planet due to the conditions of the hole in the layer is one of the obvious consequences seen today [1]. Vehicles have a place in most of our daily lives in terms of transportation and comfort, and their use is a necessity. The electric vehicle project has reemerged because diesel and gasoline cycle processes do not pollute the environment and reduce oil reserves.

Electric vehicles are environmentally friendly because they have less carbon emissions compared to fossil fuel vehicles. Additionally, electric vehicles are a sustainable option due to their energy efficiency and low operating costs [1]. In electric vehicles, the DC motor transmits the drive to all four wheels using the stored electricity needed by the DC motor from the battery pack. They do not harm nature with their zero emission values during operation, but also provide a quiet and comfortable driving opportunity. However, for the development and use of the electric vehicle market to increase, users' concerns about range, rechargeability and battery life should be eliminated [2, 3]. Today, the most suitable battery type for storing the electrical energy needed by an electric vehicle is Li-ion batteries. Although Li-ion batteries are the most efficient, they need improvement. For the use of Li-ion batteries, the cost must decrease, and it is of great importance to be able to estimate batteries [4, 5]. It is difficult to predict battery life in this process because the life of Li-ion batteries can vary depending on the driver's driving style, charge-discharge cycles and the driver's charging habits [6,7].

In order to make a comment about the remaining healthy life of the batteries, instantaneous state of health (SOH) data must be known. Data measurements are made on the battery pack for battery SOH predictions [8]. Applications with real-time measurements are known as direct measurement techniques in literature. Direct measurement techniques include specific measurement techniques such as Ah counting, capacity testing, internal resistance measurement and electrochemical impedance spectroscopy [9 - 11]. Ah counting method can also be seen as Coulomb counting method in some sources. It is one of the most used experimental techniques today when the health status of a battery or batteries is desired to be estimated experimentally. In the Ah counting method, the current supplied to the battery during charging and the current drawn from the battery during discharge are checked [9]. Thus, the instantaneous capacity of the battery can be estimated. In the Ah counting method, it is important for the consistency of the method that the battery enters the charge-discharge cycle in an environment close to room temperature and is charged and discharged with currents that are not very variable. Measurements made and data collected in electric vehicle battery systems are generally used to control system operation. With the measurements performed, SOH and instantaneous state of charge (SOC) calculations of the batteries are made [8]. This information obtained can also be used to examine the system's efficiency within a certain period of time and to increase the future performance of the system. Real-time measurement and analysis become important in terms of timely intervention to malfunctions that may occur in electric vehicle systems. It is also clear that real-time measurement and monitoring systems are needed in hybrid vehicle systems with multiple sources [12 - 14].

In the literature, the regulation and evaluation of the electric vehicle battery system [6, 15], tracking of battery charge amounts [16 - 18] and plug-in battery systems are mentioned in the literature. Data collection systems are known to measure stress and oxidation in systems such as hybrid and electric vehicles [19, 20]. The common features of these records are the use of data records to obtain measurement data and the analysis of these records by transmitting them to computers at certain periods. In this way, different battery characteristic data and counting methods were obtained from the abundances found in the literature, and 500 cycles of real-time charge-discharge expression were carried out during the current count. Data regarding battery current, battery voltage, battery properties and environmental temperature were measured with relevant sensors. With the operating data measurement system, fault errors, battery

charge, health and charge state change and battery characteristics have been obtained, and an infrastructure of the cells is available for life estimation programming.

Arduino IoT Cloud is a cloud-based platform developed by Arduino. This platform, which supports various hardware such as Arduino MKR family boards, Arduino Nano family boards, ESP32 and ESP8266 based boards, facilitates the development of IoT projects. It is also possible to remotely update the project with Arduino IOT Cloud, which is a very easy-to-use platform where devices can be connected, data can be visualized, and the project can be controlled from anywhere. It also offers the opportunity to use the control panel created for the project on either a computer or mobile devices [21].

The Internet of Things (IoT) has revolutionized various domains, including agriculture, energy management, and infrastructure digitalization. Arduino, a popular microcontroller platform, has been extensively used in IoT applications due to its versatility and ease of programming [22]. The integration of Arduino with IoT cloud platforms has enabled real-time data tracking and monitoring in diverse applications [23, 24]. Additionally, the combination of Arduino with cloud computing has expanded the scope of IoT applications, enhancing its capabilities and enabling secure self-configuration of embedded devices [25, 26].

In the context of smart agriculture, Arduino-based IoT systems have been employed for automatic plant watering and environmental monitoring [27, 28]. These systems utilize Arduino microcontrollers to collect data from sensors and transmit it to the cloud for further analysis and decision-making. Furthermore, in the domain of energy management, IoT solutions based on Arduino have been developed for monitoring and controlling electrical energy consumption [29]. These systems enable users to track power consumption in real-time and take measures to conserve energy.

Moreover, the use of Arduino in IoT applications extends to infrastructure digitalization, where it has been integrated with cloud platforms for real-time monitoring of production processes and supply chain maintenance [30]. This integration facilitates the analysis of product life cycles and enhances business models through efficient provisioning and marketing strategies.

The seamless integration of Arduino with IoT cloud platforms has also been leveraged in environmental monitoring systems, such as pollution detection and pressure monitoring [31, 32]. These systems utilize Arduino devices to collect environmental data and transfer it to cloud databases for analysis and visualization. Additionally, the combination of Arduino with cloud computing has significantly enhanced the growth of IoT by ensuring and supporting the quality of service for IoT applications [33]. Many studies in the literature collectively emphasize the potential of Arduino-based IoT systems in monitoring and managing battery-related parameters, such as performance, usage, and environmental conditions, through cloud integration. The utilization of IoT for battery monitoring systems holds significant promise in enhancing the efficiency and reliability of various applications, including electric vehicles, energy management, and environmental monitoring.

The integration of Arduino with IoT cloud platforms has been widely explored in the context of battery monitoring systems Astutiningtyas et al. demonstrated the use of Arduino and cloud for real-time data tracking from a crop field, showcasing the potential for monitoring and controlling environmental parameters, including battery status [22]. Furthermore, the work by focused specifically on an IoT-based battery monitoring system for electric vehicles, emphasizing the relevance of IoT in battery management and maintenance [34]. Additionally, Kezhiyur et al. presented a system for monitoring and controlling electrical energy consumption using IoT, highlighting the applicability of IoT in managing power resources, including battery usage [24]. Moreover, Rusimamto et al. implemented an Arduino-based temperature monitoring system, which can be extended to include battery temperature and performance monitoring in IoT applications [35].

In summary, the integration of Arduino with IoT cloud platforms has facilitated the development of diverse IoT applications,

ranging from smart agriculture and energy management to infrastructure digitalization and environmental monitoring. This integration has not only expanded the capabilities of IoT systems but has also contributed to the efficient and secure deployment of IoT solutions. The integration of Arduino with IoT cloud platforms offers a robust foundation for developing advanced battery monitoring systems, enabling real-time data tracking, analysis, and decision-making to ensure optimal battery performance and longevity.

2. Materials and Methods

2.1. Charging and discharging characteristics of the battery pack

During the creation of the battery pack for the analysis of battery characteristics, 18650 NCR 3300 mAh 3.7 V Li-ion battery cells of the Panasonic brand and 2 pieces of 3-slot plastic Liion battery beds were used to create a 6-series battery pack from Li-ion battery cells. The capacity of the created battery model is 3300 mAh and the terminal voltage is 25.2 V. HX-6S12A brand battery management system (BMS) was used to protect the battery pack and ensure balance between cells. This NCR18650PF type battery produced by Panasonic can typically provide efficiency for 500 charge-discharge cycles. Panasonic NCR18650PF is a cylindrical battery based on Li-ion battery technology. These Li-ion batteries are generally available at a nominal voltage of 3.7 V. While the maximum voltage of the battery is 4.2 V, the cut-off voltage during the discharge process is 2.5 V. In addition, the maximum continuous discharge current of the battery is 3.5 A [37].

A battery charging voltage of 25.2 V was obtained by using a 36 V DC power supply and XL4015 current adjustable DC/DC converter circuit in the charging circuit setup from the charge discharge current counting and temperature measurement data reading circuits. The maximum current on the XL4015 was set to 1.65 A to charge the created battery pack at a rate of 0.5 C. The output voltage of the XL4015 module can also be increased to 25.2 V by fixing it at 25.2 V which is the charging voltage of the battery pack. The battery pack is charged to the full charge voltage of 25.2 V in the charging cycle. The probe of the temperature sensor is fixed on the surface of the battery pack. The ACS712 current sensor is connected to the Arduino Uno board to read the temperature sensor and current data. In order to discharge the battery pack with 4 A, a load bank consisting of 6 12 V 21 W bulbs was created. While creating the load bank, 3 parallel circuits were established with 2 serial bulb connections to obtain 24 V voltage, and it was observed that the created load bank drew 4 A current from the battery, corresponding to a discharge rate of 6/5 C. In the discharge cycle, the battery pack was discharged to the cut-off voltage of 19.2 V, and when the cut-off voltage was reached, the discharge cycle was terminated by the battery management system (BMS). The surface temperature of the battery and the current drawn during discharge were transferred to the computer environment.

Battery surface temperature data taken from the temperature sensor and charge-discharge current data taken from the current sensor were transferred to the computer and converted into a txt file. Figure 1 shows the charge-discharge current counting circuits, and Figure 2 shows the txt file where the battery data is recorded.

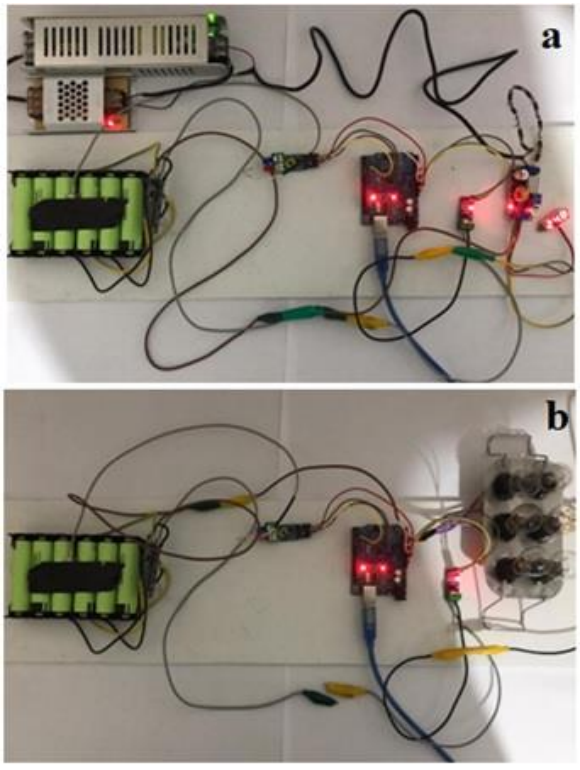

Figure 1. (a) Charging, (b) discharging current counting circuit.

After the initial SOC value was determined,

the battery was subjected to successive charging and discharging cycles, and the instantaneous SOC status was monitored according to the measured current, voltage and temperature values in these cycles, and the capacity value of the battery at the end of each charge-discharge cycle was calculated. The algorithm for the charge discharge cycle life is given in Figure 3.

After completing 500 charge-discharge cycles, the data for each cycle was transferred to Excel. Capacity calculations were then performed for each cycle, and two separate graphs were created to show the capacity change during charging and discharging using the calculated capacity data. The capacity data were used to calculate the capacity change using Equation 1, and the change in capacity was expressed as a percentage.

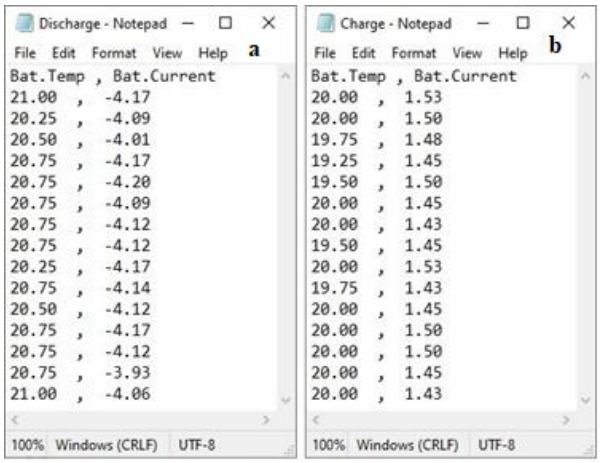

Figure 2. txt file of (a) discharge current, (b) charging current and surface temperature data

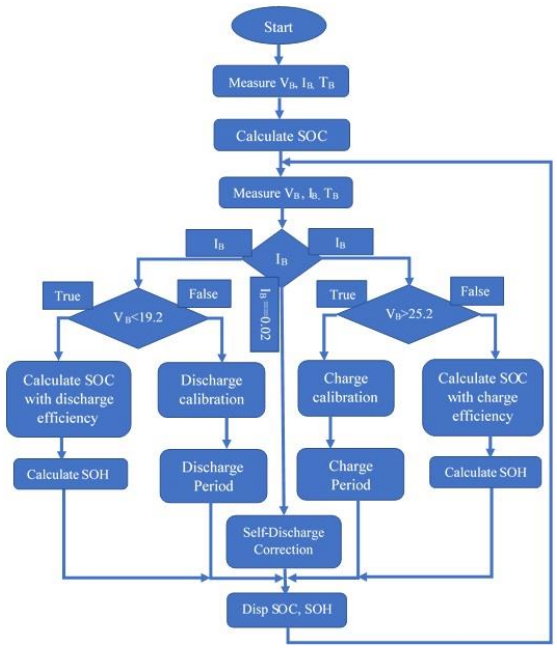

Figure 3. Flowchart of battery charge-discharge cycle

$$SOH(\%) = \frac{Holdable\ Capacity}{Initial\ Capacity} x100 \quad (1)$$

The temperature sensor installed on MAX 6675 was utilized to continuously measure the battery surface temperatures over 500 cycles. The temperature data was recorded and transferred to an Excel spreadsheet, enabling analysis of both current temperature readings and temperature changes during each cycle.

2.2. Determination of the battery pack characteristics

Ensuring the estimated decrease in the charging and carrying capacity of the battery at the end of 500 cycles. It was observed that the initial charging capacity of 3367.21 mAh decreased to 2513.94 mAh when the 500th cycle was reached. On the other hand, the results of 1972.93 mAh achieved in the last cycle of this battery model with an initial performance of 2954.05 mAh were revealed. It has been observed that charging and power capacities decrease after the 150th cycle. In Figure 4, the changing of the charging capacity and in Figure 5, the change graphs of the discharging capacity were shown.

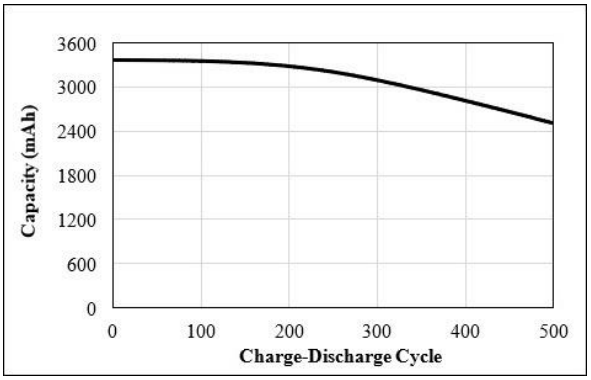

Figure 4. Change of charging capacity depending on the cycle

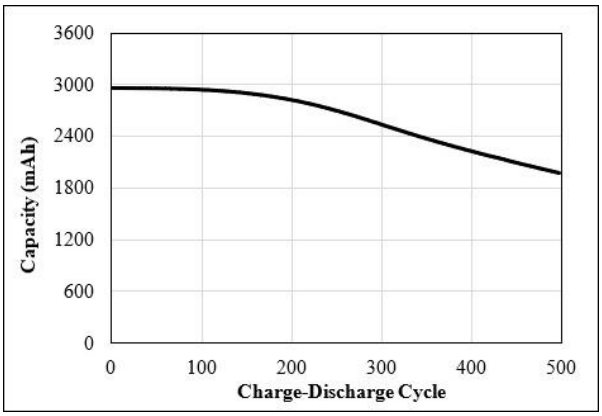

Figure 5. Change of discharging capacity depending on the cycle

As a result of all cycles, rechargeable capacity

decreased to 74.66% and early discharge capacity decreased to 66.70%. According to the information given in the literature, it is accepted that the battery pack reaches EoL (end of life) at 70% capacity, that is, when its capacity decreases [38], and this situation is observed at a certain level. 66.70% with 500 cycles of the battery model used effectively. Table 1 shows the percentage changes of charging and power capacities according to certain cycles.

Table 1. Percentage changes of capacities depending on the cycle

Cycle	Charge (%)	Discharge (%)
0	100.00	100.00
50	99.90	99.87
100	99.61	99.37
150	98.90	98.03
200	97.52	95.43
250	95.21	91.29
300	91.94	85.90
350	87,98	80.38
400	83.67	75.44
450	79.19	70.93
500	74.66	66.70

Battery efficiency is obtained by dividing the discharge capacity by the charging capacity in the relevant charge-discharge cycle, as seen in Equation 2. The battery pack, which had an efficiency of 87.73% in the first cycle, reached the end of its life with an efficiency of 78.48% when it reached the last cycle, the 500th cycle. Figure 6 shows the change graph of battery efficiency depending on the number of cycles.

$$Battery\ Efficiency = \frac{Holdable\ Capacity}{Initial\ Capacity} x100 \quad (2)$$

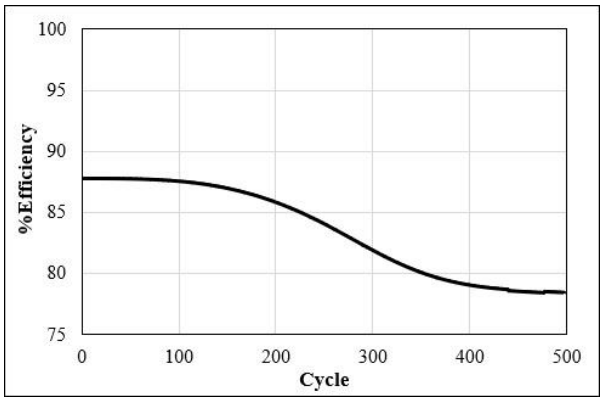

Figure 6. Battery efficiency depending on the number of cycles

It was observed that the battery surface temperature started the discharging phase at 25°C and rose to 45°C during discharging. At the end of the discharge process, the battery pack reached 45°C and were recharged at the same temperature, and when reached within the charging period, the surface temperature reduced to room temperature. Although the charging and discharging times were reduced, the battery surface temperature increased to 45°C during discharge process. It was also observed that, following the completion of the 300th charging phase, the battery was charged to capacity before the battery surface temperature had reached room temperature.

In addition to obtaining the current data and capacity values of each cycle transferred to the Excel environment, the charge curve profile of the relevant cycle was obtained. In the first charging phase of the battery, the CC (constant current) period continued for 2100 s, and then the charging was completed with the CV (constant voltage) period for 1600 s. It was observed that the CC period, which was 2100 seconds in the first charge, decreased to 1515 seconds when the last cycle was reached, while it reached 2500 seconds in the CV period. As expected, the duration of the discharge phase decreased, but no change was observed in the currents. Figure 7 shows the charge profile curves of 3 different cycles.

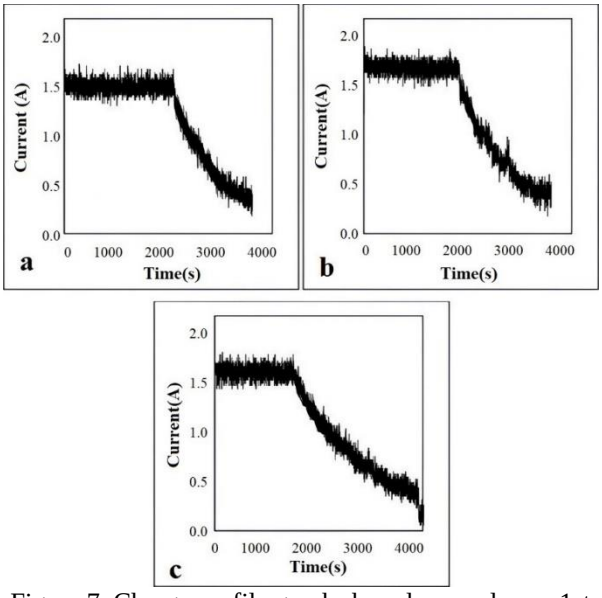

Figure 7. Charge profile graphs based on cycles; a: 1st cycle, b: 250th cycle, c: 500th cycle

2.3. Monitoring of the battery operating parameters on mobile interface

Battery monitoring circuit update has been properly communicated with Arduino IoT Cloud. Battery pack terminal voltage, charging and current currents, battery temperatures and

battery SOH and SOC values were calculated remotely based on these data are also kept in the charging or discharging mode of the battery. The electronic circuit diagram of the battery monitoring system created with ESP8266 is shown in Figure 8. The electronic circuit hardware implementation of the system is shown in Figure 9. The data received from the battery during the charge-discharge cycle is transferred and visualized on the mobile interface through IoT, as depicted in Figure 10. Table 2 provides a comparison of the total cost, the developed low-cost battery monitoring system and the average price of an equivalent device available on the market. The developed low-cost battery monitoring system, as presented in this study, is capable of monitoring battery parameters such as the battery SOC, SOH, temperature, charge-discharge current, and terminal voltage data. All related data were displayed in the mobile application via the Arduino IOT Cloud platform with the ESP8266 Arduino card during daily use of the battery module.

3. Conclusion

In the study, it is carried out, one of the biggest questions of electric and hybrid vehicle users was monitored Li-ion battery data with a mobile interface via Arduino IOT Cloud. The study is based on obtaining characteristic data of the battery module in an electric and hybrid vehicle battery pack and determining the battery health status for each cycle with the obtained data. The extraction process of battery characteristic data lasted for 500 charge-discharge cycles at room temperature. The battery pack completed its charging periods at 25°C room temperature throughout its healthy life and it was observed to warm up to 45°C at the end of the discharge processes.

When the collected data were examined, it was observed that the instantaneous charge state, instantaneous health state and battery efficiency values decreased as expected, with the obtained charge-discharge profiles and cycle-related capacity loss, as in the literature. It was observed that when 500 charge-discharge cycles were reached, the retainable capacity of the battery module dropped below 70% compared to the initial capacity, reaching the end of its usable life. Battery efficiency was obtained by dividing the discharge capacity obtained for each cycle by the charging capacity. It was observed that the efficiency of the battery pack, which was 87.73% in the first cycle, decreased to 78.48% when the last cycle was reached.

As a result, a cost-effective module has been developed that enables IoT communication with lithium-ion battery packs. With this innovative module, it is now possible to predict the lifetime of the lithium-ion battery pack, even when it is located remotely, as long as it is connected to the internet.

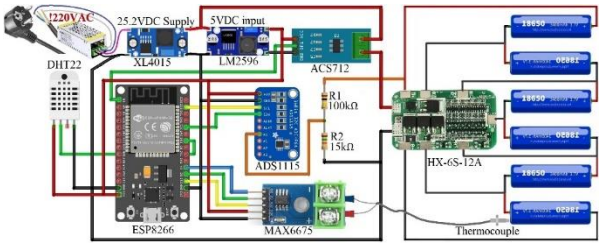

Figure 8. Electronic circuit diagram of battery tracking system functioning with IoT Cloud platform.

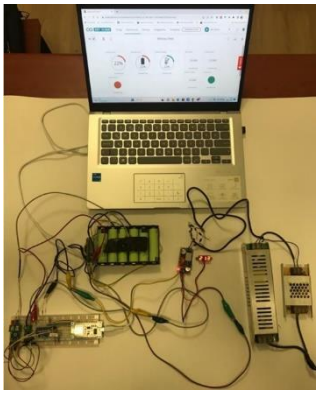

Figure 9. Hardware implemention of system design

Figure 10. Arduino IoT Cloud mobile interface; a) Charging time, b) Discharging time.

Table 2. The total cost of the battery monitoring system and market price comparison

Component	Description	Number	Price (₺)	Total (₺)
ESP8266	To communicate with the Arduino Cloud	1	100	100
DHT22	To obtain working environment humidity and temperature information	1	80	80
ADS1115	To obtain working environment humidity and temperature information	1	90	90
ACS712	To read battery pack charge/discharge currents	1	50	50
LM2596	To convert the 36VDC voltage at the power supply output to 5VDC	1	40	40
15kΩ/100kΩ Res.	To divide the battery terminal voltage to the appropriate voltage level for the ADS1115 input	1	0.30	0.30
MAX6675 Thermocouple	To monitor battery pack surface temperature	1	95	95
36VDC 5A Power Supply	For power supply of battery pack and electronic circuit	1	200	200
				655.30 ₺
Average price of equivalent device commercially available in the market [39].				**10985 ₺**

This study has provided valuable insights for predicting the life and health of Li-ion battery packs used in electric and hybrid vehicles. The results obtained enhance our understanding of Li-ion battery performance over time, which supports the advancement of battery technology and efforts to improve the overall performance of electric and hybrid vehicles.

Acknowledgment

This study was supported by Pamukkale University Scientific Research Projects Coordination Office (PAÜ, BAP, Project Number: 2022FEBE030).

Credit authorship contribution statement

The contribution rates of the authors to the study are equal.

Declaration of Competing Interest

The authors declare that they have no known competing financial interests or personal relationships that could have appeared toinfluence the work reported in this paper.

4. References

1. M. Haidar, K. M. Muttaqi, D. Sutanto, Technical challenges for electric power industries due to grid-integrated electric vehicles in low voltage distributions: A review, Energy Conversion and Management, 86, 689-700, 2014.

2. Z. S. Gelmanova, G. G. Zhabalova, G. A. Sivyakova, O. N. Lelikova, O. N. Onishchenko, A. A. Smailova, S. N. Kamarova, Electric cars. Advantages and disadvantages, In Journal of Physics: Conference Series, 1015, 5, 052029, 2018.

3. H. Özbay, C. Közkurt, A. Dalcalı, M. Tektaş, geleceğin ulaşım tercihi: elektrikli araçlar, akıllı ulaşım sistemleri ve uygulamaları dergisi, 3, 1, 34-50, 2020.

4. D. Deng, Li-ion batteries: basics, progress, and challenges, Energy Science & Engineering, 3, 5, 385-418, 2015.

5. K. Wang, J. Wan, Y. Xiang, J. Zhu, Q. Leng, Wang, M., Y. Yang, Recent advances and historical developments of high voltage lithium cobalt oxide materials for rechargeable Li-ion batteries, Journal of Power Sources, 460, 228062, 2020.

6. S. J. Gerssen-Gondelach, A. P. Faaij, Performance of batteries for electric vehicles on short and longer term, Journal of power sources, 212, 111-129, 2012.

7. Y. N. Wang, Power battery performance detection system for electric vehicles, Procedia computer science, 154, 759-763, 2019.

8. K. Saqli, H. Bouchareb, M. Oudghiri, N. M'Sirdi, An overview of State of Charge (SOC) and State of Health (SOH) estimation methods of Li-ion batteries, IMAACA 2019, 2019.

9. N. Yang, X. Zhang, G. Li, State of charge estimation for pulse discharge of a LiFePO4 battery by a revised Ah counting, Electrochimica Acta, 151, 63-71, 2015.

10. H. G. Schweiger, O. Obeidi, O. Komesker, A. Raschke, M. Schiemann, C. Zehner, P. Birke, Comparison of several

methods for determining the internal resistance of lithium-ion cells, Sensors, 10, 6, 5604-5625, 2010.
11. S. K. Pradhan, B. Chakraborty, Battery management strategies: An essential review for battery state of health monitoring techniques, Journal of Energy Storage, 51, 104427, 2022.
12. P. S, Attidekou, C. Wang, M. Armstrong, S. M. Lambert, P. A. Christensen, A new time constant approach to online capacity monitoring and lifetime prediction of lithium-ion batteries for electric vehicles (EV), Journal of the Electrochemical Society, 164, 9, A1792, 2017.
13. M. Asaad, F. Ahmad, M. S. Alam, Y. Rafat, IoT enabled monitoring of an optimized electric vehicle's battery system, Mobile Networks and Applications, 23, 994-1005, 2018.
14. M. H. Abd Wahab, N. I. M. Anuar, R. Ambar, A. Baharum, S. Shanta, M. S. Sulaiman, H. F. Hanafi, IoT-based battery monitoring system for electric vehicle, International Journal of Engineering & Technology, 7, 505-510, 2018.
15. Z. B. Omariba, L. Zhang, D. Sun, Review of battery cell balancing methodologies for optimizing battery pack performance in electric vehicles, IEEE Access, 7, 129335-129352, 2019.
16. K. Sarrafan, D. Sutanto, K. M. Muttaqi, an electric circuit based EV battery model for runtime prediction and state of charge tracking, In 2017 IEEE Transportation Electrification Conference (ITEC-India), 1-6, 2017.
17. K. Sarrafan, K. M. Muttaqi, D. Sutanto, Real-time state-of-charge tracking system using mixed estimation algorithm for electric vehicle battery system, In 2018 IEEE Industry Applications Society Annual Meeting (IAS), 1-8, 2018.
18. D. Li, J. Ouyang, H. Li, J. Wan, State of charge estimation for LiMn2O4 power battery based on strong tracking sigma point Kalman filter, Journal of power sources, 279, 439-449, 2015.
19. Wang, J. H. Fernandez, A. Massoud, A wireless battery temperature monitoring system for electric vehicle charging, In 2019 IEEE SENSORS, 1-4, 2019.
20. C. Hua, M. Y. Lin, A study of charging control of lead-acid battery for electric vehicles, In ISIE'2000 Proceedings of the 2000 IEEE International Symposium on Industrial Electronics (Cat. No. 00TH8543) 1, 135-140, 2000.
21. Arduino, bring your IoT projects to life quickly, Connect anything to Arduino Cloud. (Accessed:10/01/2024)
https://cloud.arduino.cc/
22. M. Astutiningtyas, M. Nugraheni, S. Suyoto, Automatic plants watering system for small garden, International Journal of Interactive Mobile Technologies (Ijim), 15, 200-207, 2021.
23. S. Zafar, G. Miraj, R. Baloch, D. Murtaza, K. Arshad, An IoT based real-time environmental monitoring system using Arduino and cloud service, Engineering, Technology & Applied Science Research, 8, 4, 3238-3242, 2018.
24. Kezhiyur, P. P. Kumar, S. Banu, G. Rajesh, Monitoring, controlling & conserving of electrical energy using IOT, Interantional Journal of Scientific Research in Engineering and Management, 06, 04, 2022.
25. T. Wang, G. Zhang, A. Liu, Z. Bhuiyan, Q. Jin, A secure iot service architecture with an efficient balance dynamics based on cloud and edge computing, IEEE Internet of Things Journal, 6, 3, 4831-4843, 2019.
26. Puliafito, A. Celesti, M. Villari, M. Fazio, Towards the integration between iot and cloud computing: an approach for the secure self-configuration of embedded devices, International Journal of Distributed Sensor Networks, 11, 12, 286860, 2015.
27. A. Anitha, A. Stephen, L. Arockiam, A hybrid method for smart irrigation system, International Journal of Recent Technology and Engineering, 8, 3, 2995-2998, 2019.
28. R. Winkler, MeteoMex: open infrastructure for networked environmental monitoring and agriculture 4.0., PeerJ Computer Science, 7, e343, 2021.
29. S. Hashmi, C. Ali, S. Zafar, Internet of things and cloud computing-based energy management system for demand side management in smart grid, International Journal of Energy Research, 45, 1, 1007-1022, 2020.
30. T. Muciaccia, P. Tedeschi, Future

scenarios for the infrastructure digitalization: the road ahead, Frontiers in the Internet of Things, 2, 1140799, 2023.
31. J. Pérez-Padillo, J. Morillo, J. Ramírez-Faz, M. Torres-Roldán, P. Montesinos, Design and implementation of a pressure monitoring system based on iot for water supply networks, Sensors, 20, 15, 4247, 2020.
32. Oliver, M. Anuradha, J. Ramya, Automated pollution detection system using iot and aws cloud, International Journal of Innovative Technology and Exploring Engineering, 8, 11, 3955-3960, 2019.
33. H. Bangui, S. Rakrak, S. Raghay, B. Bühnová, Moving to the edge-cloud-of-things: recent advances and future research directions, Electronics, 7, 11, 309, 2018.
34. Sangari, K. Eswaramoorthy, V. Kiranmayee, J. A. Sheeba, D. Sivamani, Iot-based battery monitoring system for electric vehicle, In 2022 IEEE International Conference on Current Development in Engineering and Technology (CCET), 1-5, 2022.
35. P. Rusimamto, E. Endryansyah, L. Anifah, R. Harimurti, Y. Anistyasari, Implementation of arduino pro mini and esp32 cam for temperature monitoring on automatic thermogun iot-based, Indonesian Journal of Electrical Engineering and Computer Science, 23, 3, 1366, 2021.
36. N. Oton, M. T. Iqbal, Low-cost open source IoT-based SCADA system for a BTS site using ESP32 and Arduino IoT cloud, In 2021 IEEE 12th Annual Ubiquitous Computing, Electronics & Mobile Communication Conference (UEMCON), 0681-0685, 2021.
37. Actec, Rechargeable Lithium Ion Batteries, PaqPOWER NCR18650GA Li-Ion battery, (Accessed:10/01/2024) URL https://en.actec.dk/media/documents/EC8A0CA01344.pdf
38. J. Lee, D. Kwon, M. G. Pecht, Reduction of Li-ion battery qualification time based on prognostics and health management, IEEE Transactions on industrial electronics, 66, 9, 7310-7315, 2018.
39. Int1: Akü izleme monitörü, (Accessed:10/01/2024) https://www.hepsiburada.com/victron-enerji-gx-touch-50-aku-izleme-monitoru-p-HBCV00002TB1Z0?magaza=Solar%20A%20Enerji.

e-ISSN: 2146 - 9067

International Journal of Automotive Engineering and Technologies

journal homepage:
https://dergipark.org.tr/en/pub/ijaet

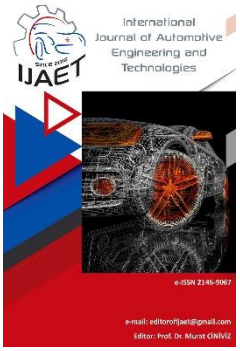

Original Research Article

Comparative conflict analysis of human-driven and autonomous vehicles at signalized intersections

Mustafa Albdairi[1*], Ali Almusawi[2], Syed Shah Sultan Mohiuddin Qadri [3]

[1,* 2] Department of Civil Engineering, Çankaya University, Ankara, Türkiye.
[3] Department of Industrial Engineering, Çankaya University, Ankara, Türkiye.

ARTICLE INFO

Orcid Numbers

1. 0009-0002-6673-363X
2. 0000-0002-4507-2492
3. 0000-0002-2950-3993

Doi: 10.18245/ijaet.1523772

* Corresponding author
c2290007@student.cankaya.edu.tr

Received: Jul 28, 2024
Accepted: Oct 16, 2024

Published: 31 Dec 2024

Published by Editorial Board Members of IJAET

ABSTRACT

Integrating autonomous vehicles (AVs) into urban traffic systems presents both opportunities and challenges, especially at signalized intersections. This study offers a comparative conflict analysis of human-driven vehicles and AVs at a busy four-legged signalized intersection in Balgat, Ankara, Turkey. Using PTV VISSIM for detailed traffic simulation, the research assesses the effects of various AV driving styles - cautious, normal, aggressive, and a mix of all three - at different penetration rates (25% to 100%), alongside standard human-driven vehicle scenarios. The Surrogate Safety Assessment Model (SSAM) is employed to analyze safety implications both before and after intersection design calibration. The findings demonstrate notable differences in conflict points between human-driven and AV scenarios. Before calibration, cautious AV behaviors result in higher conflict points due to increased queuing, while aggressive behaviors reduce conflicts through more efficient traffic flow. Human-driven vehicles exhibit varied conflict levels based on driver behavior. After calibration, significant improvements are observed across all scenarios, with aggressive AVs achieving the greatest reduction in conflict points. This study highlights the potential for AVs to improve intersection safety and efficiency when appropriate design calibration measures are implemented.

Keywords: Autonomous Vehicles, Signalized Intersections, Traffic Simulation, Conflict Analysis, Intersection Design Calibration

1. Introduction

Autonomous vehicles (AVs) are rapidly transforming urban transportation, offering both promising advancements and significant challenges, particularly at signalized intersections (1,2). These intersections are critical nodes in urban traffic management, where the integration of AVs can significantly impact traffic flow and safety (3).

Understanding the dynamics of AVs at these intersections is crucial for developing strategies to optimize their performance and mitigate potential conflicts (4).

As AVs are integrated into existing traffic systems, they introduce complexities that stem from the interaction of both AVs and human-driven vehicles. Signalized intersections, where vehicles from multiple directions converge, are uniquely challenging for AVs (5). Managing this complexity involves interpreting traffic signals, navigating human drivers' unpredictability, and adhering to right-of-way rules.

Moreover, the varied driving behaviors of AVs - ranging from cautious to aggressive - further complicate their interaction with human drivers and other AVs (6). Cautious AVs may prioritize safety and adhere strictly to traffic laws, which can lead to increased queuing and potential delays (7). Conversely, aggressive AVs aim to minimize travel time by taking advantage of gaps in traffic, which may improve flow but also increase the risk of conflicts (8).

The presence of mixed traffic conditions, where human-driven vehicles and AVs share the road, adds another layer of complexity. Human drivers exhibit a wide range of behaviors and decision-making processes that can be unpredictable, making it challenging for AVs to accurately anticipate and react to their actions. This unpredictability can lead to conflicts, such as sudden braking or swerving to avoid collisions. Additionally, AV penetration rates, defined as the proportion of AVs in the overall traffic mix, vary across scenarios, impacting traffic dynamics and the effectiveness of management strategies (9).

Understanding the interaction between AVs and human-driven vehicles at signalized intersections is not only essential for improving traffic efficiency but also for ensuring safety. Studies have indicated that while AVs have the potential to reduce traffic accidents, the transitional phase where both AVs and human-driven vehicles coexist presents significant safety challenges. This study aims to address these challenges by conducting a comprehensive conflict analysis, which will provide insights into how different AV behaviors and penetration rates impact safety and efficiency at signalized intersections. By doing so, it seeks to inform the development of strategies and policies that can facilitate the seamless integration of AVs into urban traffic systems, ultimately leading to safer and more efficient intersections.

The primary problem addressed in this study is the analysis of conflict points associated with the interaction between AVs and human-driven vehicles at signalized intersections. Conflicts, such as near-crashes or sudden braking incidents, can provide valuable insights into the safety and efficiency of traffic systems incorporating AVs. This study seeks to fill the gap in existing research by focusing on conflict analysis, which is a less explored but vital aspect of AV integration in urban traffic.

The objectives of this study are threefold: first, to evaluate the impact of different AV driving behaviors (cautious, normal, aggressive, and a mix of these) on conflict points at a busy four-legged signalized intersection; second, to compare these scenarios with those involving human-driven vehicles; and third, to assess the effects of intersection design calibration on reducing conflict points. By addressing these objectives, the study aims to provide practical recommendations for enhancing traffic safety and efficiency in mixed traffic environments.

2. Literature Review

The integration of autonomous vehicles (AVs) into urban traffic systems has sparked considerable research interest, particularly in understanding how these vehicles interact at signalized intersections. One major area of focus has been the conflict analysis between AVs and human-driven vehicles at these critical junctions. Signalized intersections are complex environments where vehicles from multiple directions converge, necessitating advanced control strategies to ensure smooth and safe traffic flow.

The integration of Connected and Automated Vehicles (CAVs) significantly enhances safety at intersections. (10) examined the impact of CAVs on signalized and unsignalized intersections using the SUMO simulator. Their findings indicate that CAVs reduce conflicts and rear-end collisions, particularly at higher penetration rates, by minimizing human error.

The study utilized car-following models such as Krauss, IDM, and CACC, with CACC notably decreasing rear-end conflicts. These results highlight CAVs' potential to improve road safety and traffic efficiency through advanced driving systems and V2V communication.

(11) Investigated the safety benefits of Automated Speed Advisory Systems (SAS) at signalized intersections. Their study demonstrated that SAS vehicles reduce collision risks and improve driving behaviors by enhancing time to collision and deceleration rates. The simulations showed that SAS vehicles, especially at higher market penetration rates, significantly lower rear-end collision risks. The research also explored various scenarios, including different ranks of SAS vehicles and lane-changing possibilities, confirming SAS's positive impact on intersection safety.

The study by (12) proposed a safety-aware and data-driven predictive control framework for CAVs at signalized intersections in mixed traffic environments. Their approach prioritizes collision avoidance with human-driven vehicles during signal phases, using a recursive least squares algorithm to approximate driving behavior. The effectiveness of the safety-aware control framework was validated through numerical simulations and robust analysis, demonstrating its potential to enhance intersection safety by deriving optimal trajectories for CAVs.

Hashmatullah and Antoniou (13) conducted a simulation-based impact assessment of AVs in urban networks using microscopic traffic models. Their study utilized a particle swarm optimization algorithm to calibrate the model and assess the influence of AV penetration on both safety and traffic efficiency. The results indicated that higher AV penetration rates significantly enhance safety; however, the impact on traffic efficiency was inconsistent. While AVs may slightly increase the average network travel time, the overall safety improvements make their integration beneficial.

A study by Kim, Cho, and Lee (14) explored a novel method using traffic accident data to identify pilot zones for AV safety testing. The approach utilizes a CNN + BiGRU model for accident classification, achieving remarkable accuracy with 100% recall and 99.5% classification accuracy. By employing outlier detection and DBSCAN clustering, the study successfully identified 562 AV-like accident cases from a total of 798. This method provides an efficient solution for selecting pilot zones, enabling effective AV safety validation while potentially reducing testing costs. The findings underscore the importance of using real-world data to enhance AV deployment safety.

However, these studies highlight the broad safety benefits of automation but do not delve into how different AV driving behaviors—such as cautious, normal, and aggressive—may impact these outcomes differently. This study aims to fill this gap by focusing on the distinct driving behaviors of AVs—cautious, normal, and aggressive—and analyzing their respective impacts on traffic conflicts at signalized intersections. By investigating how each of these behaviors affects traffic dynamics and safety outcomes, this research provides a more detailed and behavior-specific understanding of AV integration, offering insights that can inform both traffic management strategies and AV policy development. This focus on behavioral differentiation is what distinguishes our approach from prior studies, offering new insights into the complexities of AV behavior in urban traffic systems.

Figure 1 Geographical Layout of the Signalized Intersection in Balgat, Ankara.

3. Methods

3.1. Study location

The research was conducted at a busy four-legged signalized intersection located in Balgat, Ankara, Turkey, which is shown in Figure 1. This intersection, situated at the crossroads of Kızılırmak and Ufuk Ünv. Cd No:18, 06520 Çankaya/Ankara, features four lanes for both northbound and southbound

traffic, and three lanes for both eastbound and westbound traffic. The selected site provides an excellent real-world scenario with high traffic density, making it ideal for evaluating the effects of Autonomous Vehicles (AVs) on traffic flow and behavior.

3.2. Research methodology overview

To enhance clarity and provide a comprehensive understanding of the research process, the methodology is summarized in the flowchart as shown in Figure 2. The research begins with Data Collection, where the focus is on gathering Traffic Volume Data and Speed Distributions. These datasets are essential for building accurate simulation models.

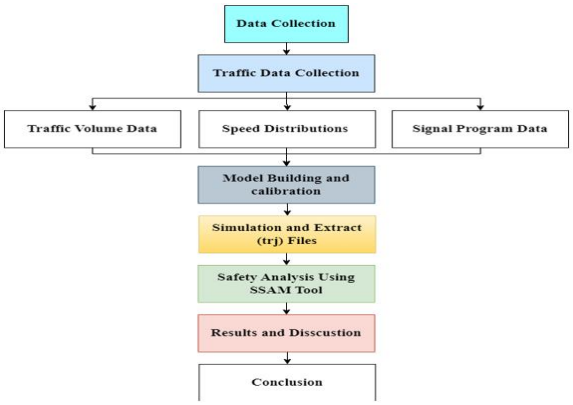

Figure 2 Flowchart of research methodology.

In the Model Building and Calibration phase, the collected data are used to construct a realistic simulation environment and ensure the model reflects real-world conditions accurately. After calibration, simulations are run, and trajectory (trj) files are extracted for analysis.

The Safety Analysis is then conducted using the Surrogate Safety Assessment Model (SSAM) tool, which processes the trajectory files to evaluate potential conflicts and safety metrics. Finally, the results from the safety analysis are interpreted and discussed in the Results and Discussion section, leading to the study's Conclusion.

This systematic approach ensures that the research is both rigorous and transparent, facilitating reproducibility and validation.

3.3. Traffic volume

The traffic volume data was collected through video analysis conducted during peak morning hours from 7:00 to 8:00 AM, as shown in Table 1. The total recorded traffic volume during this period was 5386 vehicles.

Table 1. Traffic movements recorded at the signalized intersection

Direction	Total Vehicles	Right Turn	Straight	Left Turn
N	1793	225	679	889
E	1033	814	157	62
S	1508	244	1228	36
W	1052	28	132	892

3.4. Signal program timing

In the context of signal timing at the studied intersection, Figure 3 illustrates the sequence of green, red, and amber light durations for each traffic direction. Detailed observations were made using video recordings to extract these traffic control parameters. The cycle time, set at 204 seconds, governed the signal sequence. As shown in Figure 3, the green light durations were observed to be 65 seconds for the northbound direction, 46 seconds for the eastbound direction, 50 seconds for the southbound direction, and 19 seconds for the westbound direction. The red and amber light durations were uniformly maintained at 3 seconds each across all directions. These signal timings were meticulously documented to reflect the actual conditions recorded during the video analysis.

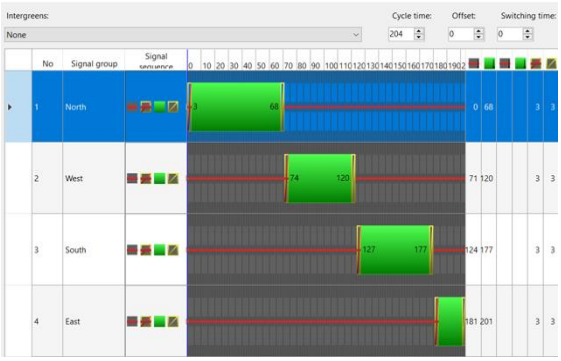

Figure 3 Signal Program Timing of the Signalized Intersection in Balgat, Ankara.

3.5. Desired speed distributions

In assessing the speed distribution for human-driven vehicles at the specified intersection, Figure 4 illustrates the results of the speed observations conducted. This analysis focuses on vehicles traveling north and south during green signals, where the speeds of 20 vehicles were measured over a 150-meter distance using a stopwatch. As depicted in Figure 4, the results show that 40% of the vehicles traveled

at speeds between 20 km/h and 27 km/h, 42.5% between 28 km/h and 36 km/h, and 17.5% between 36 km/h and 39 km/h.

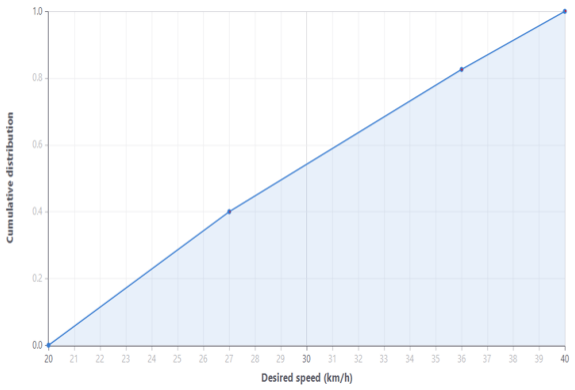

Figure 4 Speed Distribution of Human-Driven Vehicles.

Figure 5 illustrates the speed characteristics of autonomous vehicles (AVs) in the simulations conducted. Whether operating independently or in mixed traffic with human-driven vehicles, AVs consistently maintained speeds between 27 km/h and 31 km/h.

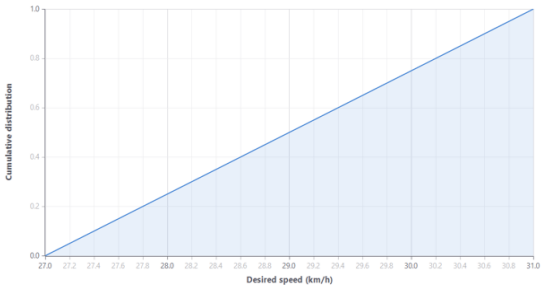

Figure 5 Speed Distribution of Autonomous Vehicles.

3.6. Car-following and lane change models

Table 2 presents the specific driving parameters defining three distinct AV driving behaviors analyzed in this study:

- Cautious AVs: Emphasized safety with a 1.50-meter standstill distance and a 1.5-second gap time, promoting conservative driving.
- Normal AVs: Balanced safety and efficiency, maintaining a 1.50-meter standstill distance but reducing the gap time to 0.9 seconds, with acceleration from standstill set at 3.50 m/s².
- Aggressive AVs: Adopted a closer 1.00-meter standstill distance, a 0.6-second gap time, and higher acceleration of 4.00 m/s², indicating more assertive driving.

Human driving behavior was simulated using the Wiedemann 74 model, which included an average standstill distance of 2.00 meters, an additive safety distance of 2.00 meters, and a multiplicative safety distance of 3.00 meters to reflect realistic driver responses and variability.

Table 2. Parameters for av car following models.

Parameter	Cautious	Normal	Aggressive
Standstill distance	1.50 m	1.50 m	1.00 m
Gap time distribution	1.5 s	0.9 s	0.6 s
'Following' distance oscillation	0.00 m	0.00 m	0.00 m
Threshold for entering 'Following'	-10.00	-8.00	-6.00
Negative speed difference	-0.10	-0.10	-0.10
Positive speed difference	0.10	0.10	0.10
Distance dependency of oscillation	0.00	0.00	0.00
Oscillation acceleration	0.10 m/s^2	0.10 m/s^2	0.10 m/s^2
Acceleration from standstill	3.00 m/s^2	3.50 m/s^2	4.00 m/s^2
Acceleration at 80 km/h	1.20 m/s^2	1.50 m/s^2	2.00 m/s^2

The lane change model parameters were adjusted for different AV driving behaviors and human drivers to simulate realistic driving scenarios. Advanced merging was enabled for all vehicle categories, while cooperative lane change was activated only for AVs. The safety distance reduction factor varied, with AV cautious at 1.00 meters, AV normal at 0.60 meters, AV aggressive at 0.75 meters, and human drivers at 0.60 meters. Minimum clearance was set at 1.00 meters for AV cautious and 0.50 meters for the other modes. The maximum deceleration for cooperative braking was -2.50 m/s² for AV cautious, -3.00 m/s² for AV normal, -6.00 m/s² for AV aggressive, and -3.00 m/s² for human drivers. (17)

The lane change model parameters were adjusted for different AV driving behaviors and human drivers to simulate realistic driving scenarios. Advanced merging was enabled for all vehicle categories, while cooperative lane change was activated only for AVs. The safety distance reduction factor varied, with AV cautious at 1.00 meters, AV normal at 0.60 meters, AV aggressive at 0.75 meters, and

human drivers at 0.60 meters. Minimum clearance was set at 1.00 meters for AV cautious and 0.50 meters for the other modes. The maximum deceleration for cooperative braking was -2.50 m/s² for AV cautious, -3.00 m/s² for AV normal, -6.00 m/s² for AV aggressive, and -3.00 m/s² for human drivers.

3.7. Intersection design calibration

Figure 6 illustrates the real-world queuing behavior observed for the east and westbound lanes during the calibration process. Initially designed with two lanes, the observed traffic volumes required an adjustment to three lanes in the simulation model to better reflect actual traffic conditions.

Figure 6 Real-world Vehicle Queuing Scenario in East and West Bound Lanes. (18)

Additionally, given the high traffic volume, it was determined that lane changes should be restricted but still allowed at exit links as illustrated in figure 7. To achieve this, each lane was modeled as a separate link for each direction. This approach aligns the simulation more closely with observed traffic behaviors, enhancing the accuracy of the model.

Figure 7 Intersection design calibrated for no lane changes: each lane as a separate link.

3.8. Conflict points analysis

Figure 8 illustrates the conflict analysis process used in this study, highlighting the identification and recording of conflict points using VISSIM's built-in conflict analysis and the Surrogate Safety Assessment Model (SSAM) tools. The primary data obtained from the simulation included the number of crossing conflicts, rear-end conflicts, and lane-change conflicts. These conflict points were meticulously analyzed to assess traffic safety. Additionally, the mean time-to-collision (TTC) was calculated to provide further insights into the severity of potential conflicts. The data was analyzed to compare the total number of conflicts and the mean TTC across different scenarios, allowing for an assessment of how various AV behaviors and penetration rates affect traffic safety at intersections. This comparison provided valuable insights into the influence of AVs on intersection safety.

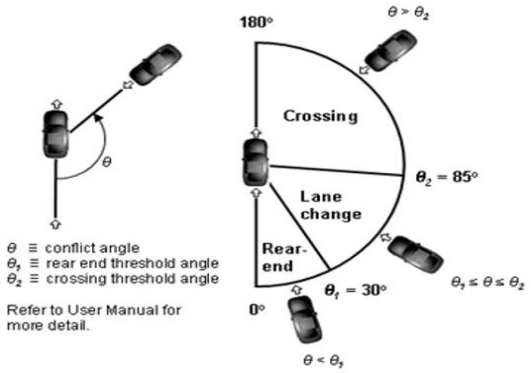

Figure 8 SSAM Angles Used for Analysis. (13)

3.9. Scenarios overview

Table 3 presents the 21 scenarios examined in this study, which investigate the interactions between human-driven and automated vehicles at intersections. These scenarios explore various AV behaviors, including aggressive, normal, and cautious, to capture the diverse dynamics of real-world traffic. This comprehensive approach ensures that the full range of potential AV impacts on traffic flow and safety are thoroughly evaluated.

Table 3. Overview of Autonomous Vehicle Scenarios

Scenarios	Cautious	Normal	Aggressive	Human
1	0%	0%	0%	100%
2	25%	0%	0%	75%
3	0%	25%	0%	75%
4	0%	0%	25%	75%
5	0%	0%	0%	75%
…	…	…	…	…
21	25%	25%	25%	25%

4. Results and Discussion

4.1. Impact of AV on conflicts point before calibration

The impact of AVs on conflict points was evaluated by comparing different AV behaviors and penetration rates before and after calibrating the intersection design.

Various types of conflicts, such as crossing conflicts, rear-end conflicts, lane-change conflicts, total conflicts, and Mean Time to Collision (TTC), were analyzed to determine how the integration of AVs influences safety at signalized intersections.

Figure 9 illustrates the number of crossing conflicts observed before and after calibration at the intersection. Initially, the intersection design resulted in higher crossing conflicts, particularly with cautious AV behavior. With 100% human-driven vehicles, there were 31 crossing conflicts. When cautious AVs were introduced at penetration rates of 25%, 50%, 75%, and 100%, the crossing conflicts decreased to 27, 7, 12, and 1, respectively. Normal AV behavior exhibited crossing conflicts of 15, 18, 8, and 1 at the same penetration rates. In contrast, aggressive AV behavior recorded 21, 10, 7, and 0 crossing conflicts. These results indicate that cautious and normal AVs can significantly reduce crossing conflicts, particularly at higher penetration rates.

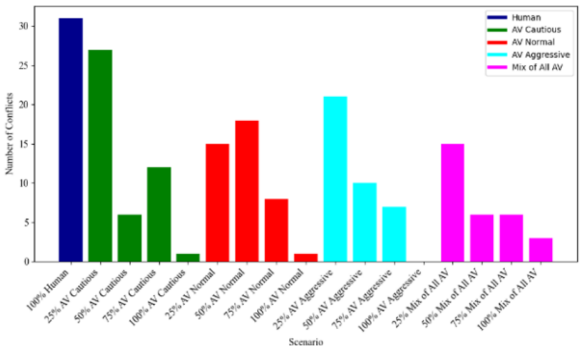

Figure 9 Crossing Conflicts for Different AV Behaviors and Penetration Rates Before Calibration.

Figure 10 illustrates the variation in rear-end conflicts across different AV behaviors. With 100% human-driven vehicles, there were 49 rear-end conflicts recorded. When cautious AVs were introduced at penetration rates of 25%, 50%, 75%, and 100%, the number of rear-end conflicts increased to 41, 57, 66, and 80, respectively. Normal AV behavior exhibited rear-end conflicts of 36, 52, 54, and 50 at the same penetration rates. In contrast, aggressive AV behavior recorded 50, 70, 97, and 96 rear-end conflicts. These findings suggest that cautious AVs tend to increase rear-end conflicts, while normal and aggressive AVs show mixed impacts depending on the penetration rate.

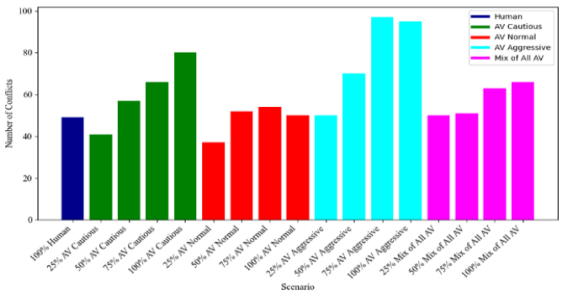

Figure 10 Rear-End Conflicts for Different AV Behaviors and Penetration Rates Before Calibration.

Figure 11 illustrates the influence of AV behavior on lane-change conflicts. With 100% human-driven vehicles, the number of lane-change conflicts recorded was 27. When cautious AVs were introduced at penetration rates of 25%, 50%, 75%, and 100%, the lane-change conflicts increased to 34, 32, 52, and 42, respectively. Normal AV behavior resulted in 23, 22, 26, and 35 lane-change conflicts at the same penetration rates. Conversely, aggressive AV behavior showed counts of 24, 21, 14, and 29 lane-change conflicts. These results indicate that normal AV behavior tends to reduce lane-change conflicts, while cautious and aggressive behaviors can lead to higher lane-change conflicts at certain penetration rates.

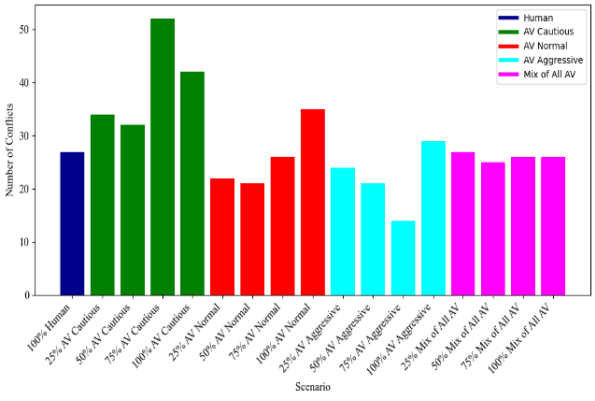

Figure 11 Lane-Change Conflicts for Different AV Behaviors and Penetration Rates Before Calibration.

Figure 12 presents the total number of conflicts across all types, highlighting the significant impact of AV behaviors and penetration rates. In the scenario with 100% human-driven vehicles, a total of 107 conflicts were recorded. The introduction of cautious AVs resulted in total conflicts of 102, 96, 130, and 123 at penetration rates of 25%, 50%, 75%, and 100%, respectively. In contrast, normal AV behavior recorded 74, 92, 88, and 86 total conflicts across the same penetration rates.

Aggressive AV behavior led to totals of 95, 101, 118, and 125 conflicts. Notably, the mixed AV behavior scenario demonstrated a moderate reduction in total conflicts, with counts of 93, 83, 96, and 96 as the penetration rates increased.

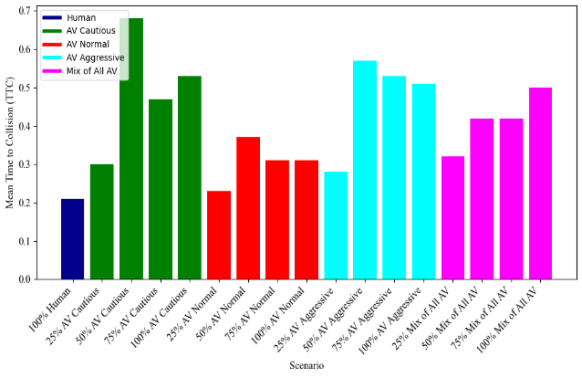

Figure 12 Total Conflicts for Different AV Behaviors and Penetration Rates Before Calibration.

Figure 13 illustrates the Mean Time to Collision (TTC) values, which provide insights into the severity of potential conflicts at the intersection. In the human-driven vehicle scenario, Mean TTC was recorded at 0.21 seconds. For cautious AVs, the Mean TTC values were 0.3, 0.68, 0.47, and 0.54 seconds at penetration rates of 25%, 50%, 75%, and 100%, respectively. Normal AV behavior exhibited Mean TTC values of 0.24, 0.37, 0.31, and 0.31 seconds, while aggressive AV behavior recorded values of 0.27, 0.57, 0.54, and 0.51 seconds. These findings suggest that cautious AVs lead to an increase in Mean TTC, indicating less severe but more frequent conflicts, while normal and aggressive AV behaviors maintain a relatively consistent Mean TTC.

4.2. Impact of AV on conflicts point after calibration

Figure 14 presents the results after calibration, showing a significant reduction in conflict points. In the scenario with human-driven vehicles, there were 14 crossing conflicts. Cautious AVs exhibited 18, 4, 0, and 0 conflicts at penetration rates of 25%, 50%, 75%, and 100%, respectively. Normal AVs recorded 16, 7, 3, and 0 conflicts, while aggressive AVs showed 11, 3, 2, and 0 conflicts. These results indicate a marked improvement in traffic safety following the calibration adjustments.

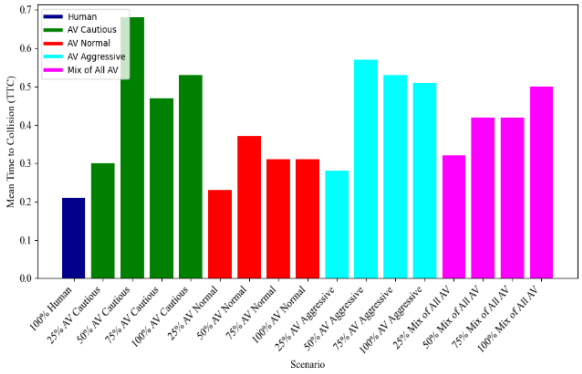

Figure 13 Mean Time to Collision (TTC) for Different AV Behaviors and Penetration Rates Before Calibration.

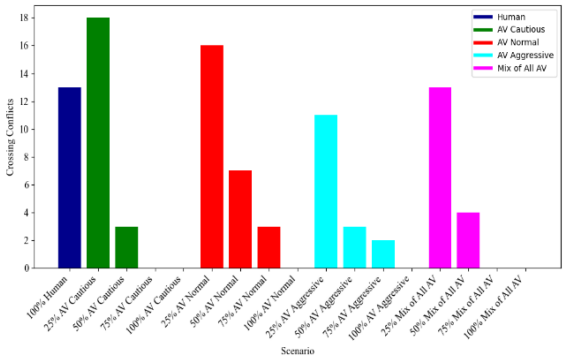

Figure 14 Crossing Conflicts for Different AV Behaviors and Penetration Rates After Calibration.

Figure 15 illustrates the results for rear-end conflicts following the calibration. In the scenario with human-driven vehicles, there were 15 rear-end conflicts recorded. Cautious AVs exhibited 9, 8, 7, and 5 conflicts at increasing penetration rates. Normal AVs showed 8, 8, 11, and 7 conflicts, while aggressive AVs recorded 9, 11, 14, and 12 conflicts. These findings highlight the varying impact of different AV behaviors on rear-end conflict occurrences.

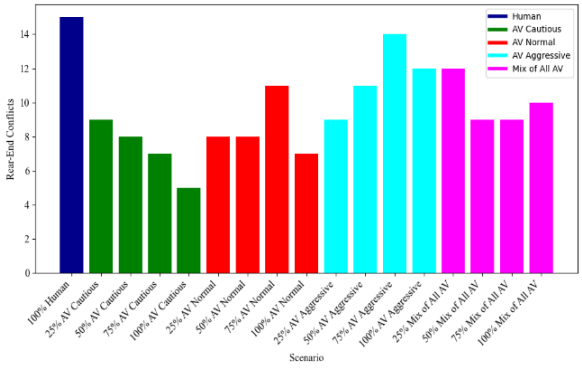

Figure 15 Rear-End Conflicts for Different AV Behaviors and Penetration Rates After Calibration.

Figure 16 shows the results for lane-change conflicts following the calibration. Lane-change conflicts were minimal post-

calibration, with human-driven vehicles recording 0 conflicts. Cautious AVs exhibited 1, 1, 1, and 3 conflicts at increasing penetration rates. Normal AVs had 0, 4, 2, and 2 conflicts, while aggressive AVs recorded 1, 2, 4, and 7 conflicts.

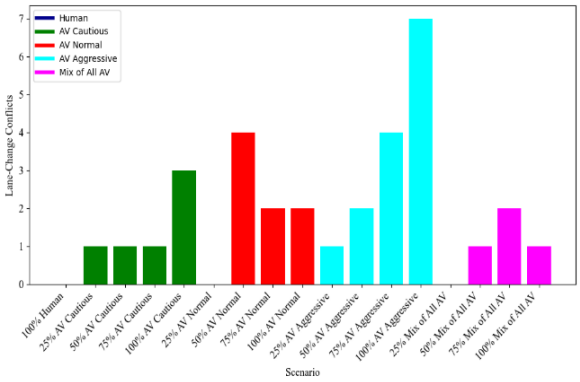

Figure 16 Lane-Change Conflicts for Different AV Behaviors and Penetration Rates After Calibration.

Figure 17 illustrates the total conflicts observed during the study. Human-driven vehicles recorded 29 total conflicts. Cautious AVs showed a decrease in conflicts, with totals of 28, 13, 8, and 8 at increasing penetration rates. Normal AVs had 24, 19, 16, and 10 conflicts, while aggressive AVs recorded 21, 16, 19, and 20 conflicts. These findings suggest that cautious AV behavior is associated with a significant reduction in total conflicts, particularly at higher penetration rates.

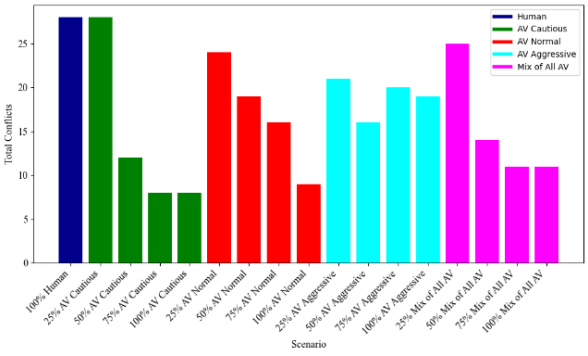

Figure 17 Total Conflicts for Different AV Behaviors and Penetration Rates After Calibration.

Figure 18 illustrates the Mean Time to Collision (TTC) observed in the study. Mean TTC increased post-calibration, indicating less severe conflicts. Human-driven vehicles had a Mean TTC of 0.48 seconds. Cautious AVs recorded Mean TTC values of 0.3, 0.42, 0.55, and 0.35 seconds. Normal AVs exhibited Mean TTC values of 0.32, 0.23, 0.57, and 0.43 seconds, while aggressive AVs showed values of 0.37, 0.58, 0.79, and 0.72 seconds. These results suggest that the post-calibration adjustments contributed to a reduction in conflict severity across all vehicle types.

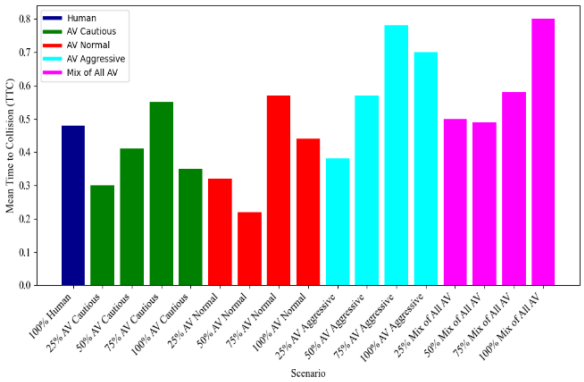

Figure 18 Mean Time to Collision (TTC) for Different AV Behaviors and Penetration Rates After Calibration.

5. Conclusion

After calibration, normal AV behavior balanced safety and efficiency, cautious AVs increased Mean Time to Collision (TTC), aggressive AVs reduced crossing conflicts but increased rear-end conflicts, and mixed AV improved overall safety. These findings underscore the need for tailored intersection designs to optimize AV integration and enhance traffic safety and efficiency.

These findings underscore the importance of designing intersection controls tailored to specific AV behaviors, with the aim of optimizing both traffic safety and efficiency. Future research should focus on real-world AV deployments to validate these simulation-based insights. Additionally, investigating the impact of varying AV penetration rates, vehicle-to-infrastructure (V2I) communication, and human-AV interaction in more complex traffic scenarios will be crucial for advancing the safe integration of AVs into urban networks. The development of dynamic signal control systems that can adapt to different AV driving behaviors and changing traffic conditions will also be essential for enhancing overall traffic management.

CRediT authorship contribution statement

Mustafa Albdairi: Conceptualization, Methodology, Software, Writing - Original Draft. Ali Almusawi: Supervision, Validation, Resources, Writing - Review & Editing. Syed Shah Sultan Mohiuddin Qadri: Data Curation, Investigation, Formal Analysis, Review &

Editing.

Declaration of Competing Interest

The authors declare that they have no known competing financial interests or personal relationships that could have appeared to influence the work reported in this paper.

Data availability

The datasets generated during and/or analyzed during the current study are available from the corresponding author on reasonable request.

Acknowledgement

The authors would like to thank Çankaya University for providing the necessary resources and tools to carry out this research. Special thanks to the Department of Civil Engineering and the Department of Industrial Engineering for their support and guidance throughout the study.

6. References

1. A. Karbasi and S. O'Hern, "Investigating the impact of connected and automated vehicles on signalized and unsignalized intersections safety in mixed traffic," Future Transportation, vol. 2, no. 1, pp. 24-40, 2022.
2. Albdairi, Mustafa, Ali Almusawi, and Syed Shah Sultan Mohiuddin Qadri, "Impact of Autonomous Vehicle Driving Behaviors on Signalized Intersection Performance: A Review," Usak University Journal of Engineering Sciences, vol. 7, no. 1, pp. 14-26, June 2024.
3. W. Do, N. Saunier, and L. Miranda-Moreno, "Safety benefits of automated speed advisory systems at signalized intersections," Transportation Research Record, vol. 2677, no. 3, pp. 551-564, 2023.
4. A. I. Mahbub, V.-A. Le, and A. A. Malikopoulos, "Safety-Aware and Data-Driven Predictive Control for Connected Automated Vehicles at a Mixed Traffic Signalized Intersection," IFAC-Papers online, vol. 55, no. 24, pp. 51-56, 2022.
5. G. Bathla et al., "Autonomous vehicles and intelligent automation: Applications, challenges, and opportunities," Mobile Information Systems, vol. 2022, no. 1, p. 7632892, 2022.
6. M. Khayatian et al., "A survey on intersection management of connected autonomous vehicles," ACM Transactions on Cyber-Physical Systems, vol. 4, no. 4, pp. 1-27, 2020.
7. E. Namazi, J. Li, and C. Lu, "Intelligent intersection management systems considering autonomous vehicles: A systematic literature review," IEEE Access, vol. 7, pp. 91946-91965, 2019.
8. E. F. Ozioko, J. Kunkel, and F. Stahl, "Road intersection coordination scheme for mixed traffic (human-driven and driverless vehicles): A systematic review," in Science and Information Conference, Springer, pp. 67-94, 2022.
9. S. K. Jayaraman et al., "Pedestrian trust in automated vehicles: Role of traffic signal and AV driving behavior," Frontiers in Robotics and AI, vol. 6, p. 117, 2019.
10. I. R. Khan, Interaction Between Autonomous Vehicles and Other Road Users—A Simulation Study. The University of Alabama in Huntsville, 2023.
11. M. Martínez-Díaz, F. Soriguera, and I. Pérez, "Autonomous driving: a bird's eye view," IET Intelligent Transport Systems, vol. 13, no. 4, pp. 563-579, 2019.
12. J. Wang, Y. V. Pant, L. Zhao, M. Antkiewicz, and K. Czarnecki, "Enhancing safety in mixed traffic: Learning-based modeling and efficient control of autonomous and human-driven vehicles," IEEE Transactions on Intelligent Transportation Systems, 2024.
13. H. Sadid and C. Antoniou, "A simulation-based impact assessment of autonomous vehicles in urban networks," IET Intelligent Transport Systems, 2024. doi: 10.1049/itr2.12537.
14. S. Kim, M.-J. Cho, and Y. Lee, "Exploration of traffic accident-based pilot zones for autonomous vehicle safety validation," Electronics, 2024. doi: 10.3390/electronics13173390.
15. Federal Highway Administration, "Surrogate Safety Assessment Model (SSAM) User Manual," U.S. Department of Transportation, Publication No. FHWA-HRT-08-050, 2008. Available at: https://highways.dot.gov/sites/fhwa.dot.gov/files/FHWA-HRT-08-050.pdf.

16. A. Osman, “Evaluation of the Impact of Automated Driven Vehicles on Traffic Performance at Four-leg Signalized Intersections,” Linköping University, Department of Science and Technology, Communications and Transport Systems, Linköping University, Faculty of Science & Engineering, 2023.
17. Almusawi, A., & Albdairi, M. “The Impact of Increasing Traffic Volume on Autonomous Vehicles in Roundabout,” Akıllı Ulaşım Sistemleri Ve Uygulamaları Dergisi, 2024.
18. A. Almusawi, M. Albdairi, and S.S.S.M. Qadri, "Integrating Autonomous Vehicles (AVs) into Urban Traffic: Simulating Driving and Signal Control," Applied Sciences, vol. 14, no. 19, pp. 8851, Oct. 2024. doi: https://doi.org/10.3390/app14198851.

e-ISSN: 2146 - 9067

International Journal of Automotive Engineering and Technologies

journal homepage:
https://dergipark.org.tr/en/pub/ijaet

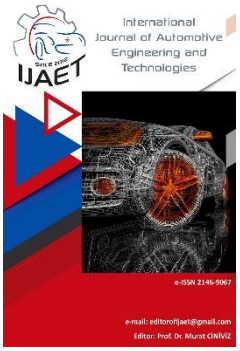

Original Research Article

Condition monitoring of internal combustion engines with vibration signals and fault detection by using machine learning techniques

Yunus Emre Karabacak[1*]

[1,*]Karadeniz Technical University, Trabzon, Türkiye.

ARTICLE INFO

Orcid Numbers

1. 0000-0002-0268-3656

Doi: 10.18245/ijaet.1251886

* Corresponding author
karabacak@ktu.edu.tr

Received: Jul 28, 2024
Accepted: Oct 16, 2024

Published: 31 Dec 2024

Published by Editorial Board Members of IJAET

ABSTRACT

Internal combustion engines are frequently used in transportation, power plants, and in many other applications for industrial purposes. For this reason, it is very important that the maintenance is done systematically and that the faults are detected correctly. In this study, two different methods were used for the detection of the healthy internal combustion engine (H) and faulty internal combustion engines (single-cylinder misfire-F1, two-cylinder misfire-F2). In the first method, classical signal features were extracted from engine vibration measurements and used in the training of artificial neural networks (ANNs) and support vector machine (SVM). In the second method, convolutional neural networks (CNNs), a deep learning method in which features are extracted automatically, are used. Spectrograms of engine vibration signals were used to train pre-trained CNNs with different structures. Spectrograms were obtained by applying short-time Fourier transform (STFT) to vibration signals. The results of GoogleNet and ResNet-50 models trained with spectrograms were compared with the results obtained from models based on ANNs and SVM.

Keywords: Fault detection, Internal Combustion Engines, Neural Networks, Deep Learning, Condition Monitoring, Vibration Signals

1. Introduction

Internal combustion engines are used in many vehicles such as cars, trucks, ships, submarines, and aircraft. They are also preferred in applications such as agriculture, transportation, and electricity generation facilities. For this reason, the maintenance of internal combustion engines and the exact detection of their faults are extremely critical issues for performance, safety, and reliability. The processes that take place inside the internal combustion engine are extremely complicated and hard to model analytically. Therefore, modern techniques of machine learning (supervised learning, unsupervised learning, reinforcement learning, and deep learning) are used in combustion control and optimization, estimation of emission values, and design or optimization of engine elements in internal combustion engines [1].

2. Literature Review

In the literature, there are a limited number of

studies on the detection of faults such as knocking, misfiring, or deterioration of engine elements in the internal combustion engine with machine learning techniques. In their study, Jafarian et al. [2] placed four vibration sensors in different positions of an automobile engine and investigated various faults, including misfire and valve clearance, using the data obtained by the sensors under various operating conditions. They also classified the engine state using various machine learning techniques with the signal features obtained using fast Fourier transform (FFT). Li et al. [3] developed an intelligent diagnostic method for marine diesel engines using instantaneous angular velocity information. In their work, they performed the implementation and evaluation of a technique based on the combination of empirical mode decomposition, independent component analysis, and support vector machine (SVM). Moosavian et al. [4] developed an intelligent diagnostic approach based on acoustic and vibration signals using a combination of sensor fusion and classifier and used artificial neural networks (ANN) and SVM techniques to diagnose spark plug faults in an internal combustion engine. Saharma et al. [5] performed the detection of misfire faults in an internal combustion engine using the features extracted from the vibration signals and the decision tree algorithm. Devasenapati et al. [6] used decision trees for feature selection and classification to identify misfire faults in a four-stroke four-cylinder internal combustion gasoline engine. Castresana et al. [7] utilized a multi-output ANN model to obtain a complete performance map of a ship's diesel engine. Wang et al. [8] proposed a new diagnostic method through hybrid algorithm-based multidimensional feature extraction for the detection of undiagnosed engine faults that affect the normal operation of vehicles. Cai et al. [9] presented a new method for diagnosing diesel engines by combining back propagation neural networks, known as Bayesian networks, with a rule-based algorithm. Kowalski et al. [10] used the extracted features by monitoring various signals produced by the engine as inputs for a feedforward neural network-based classification algorithm. Karatuğ and Arslanoğlu [11] developed a condition-based maintenance system for fault diagnosis in ship engine systems using ANN and illustrated three scenarios. Flett and Bone [12] used machine learning methods to detect valve spring and valve clearance faults in diesel engines and compared their methods with each other in terms of performance. Wang et al. [13] diagnosed the faults of a diesel engine based on adaptive wavelet packets and empirical mode decomposition and used fractal dimension features for this purpose. Basurkoa and Uriondo [14] developed a condition-based maintenance strategy for medium-speed diesel engines used on ships. They trained a feed-forward neural network to build the engine performance model and detected the engine's fuel consumption and fault condition. In the study by Küçüksarıyıldız et al. [15], specific fuel consumption for a 60 HP tractor was evaluated under different conditions of axle load, tire pressure, and drawbar force. The results were also predicted using ANN, with the best model demonstrating high accuracy in its predictions. Togun and Baysec [16] developed an ANN model to predict torque and brake specific fuel consumption of a gasoline engine using spark advance, throttle position, and engine speed. Based on experimental data, the model was trained and tested, showing satisfactory accuracy. The ANN model is also presented as an explicit mathematical function. Çay et al. [17] developed an ANN model to predict brake specific fuel consumption, effective power, average effective pressure, and exhaust gas temperature of a methanol engine. Based on experimental data from a four-cylinder engine, the model achieved regression values close to 1, RMS values below 0.015, and mean errors under 3.8%, demonstrating its effectiveness in predicting engine performance. Parlak et al. [18] studied an ANN model using a back propagation algorithm to predict specific fuel consumption and exhaust temperature of a Diesel engine at different injection timings. The model achieved a mean absolute relative error of less than 2% compared to experimental results, indicating strong consistency and making it a useful tool for preliminary thermal engineering analyses.

Looking at the studies in the literature, it can be seen that vibration analysis is the prominent

approach in diagnosing the faults of internal combustion engines. In addition, studies using modern machine learning techniques in the detection of engine faults are also extremely limited. With the effective use of modern machine learning techniques, engine faults can be diagnosed. Therefore, in this study, two methods based on machine learning and vibration analysis are utilized for the detection of internal combustion engine faults. Accordingly, vibration signals were classified using two different machine-learning methods. In the first method, ANN and SVM models are trained with classical features extracted from their signals. In the second method, spectrograms were obtained from vibration signals and CNN models were used to detect engine faults. Engine vibration data shared by Randall in his Vibration-based Condition Monitoring book [19] were utilized to validate the two methods presented. Finally, the results obtained from the methods were compared in terms of performance.

3. Materials and Methods

3.1 General information

In a diesel engine, the thermodynamic energy obtained by the ignition of the air-fuel mixture in the cylinder is converted into mechanical energy via the slider-crank mechanism. Fig. 1 shows an inline 6-cylinder internal combustion engine with a 1-5-3-6-2-4 ignition pattern.

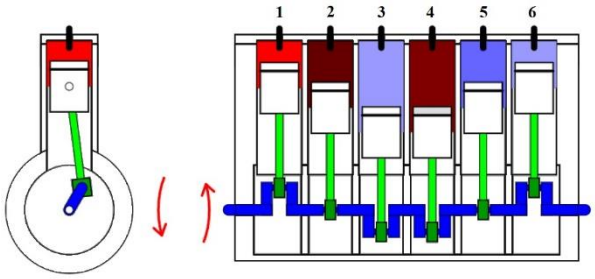

Fig. 1 6-cylinder internal combustion engine

Significant vibrations occur in engines due to factors such as oscillating and rotating parts, cyclical changing of gas pressure due to combustion, and inertia forces of moving parts. These vibrations usually occur as torsional vibration, longitudinal vibration, and mixed vibrations. Torsional vibrations are mainly caused by the cyclic gas pressure in the cylinder as a result of combustion and the mass forces of the moving parts. That is, changing the crankshaft rotational speed causes velocity fluctuations, hence torsional vibrations [19,20]. Therefore, torsional vibrations can contain information about engine malfunctions that affect gas pressure, such as misfires and valve clearance. Fig. 2 shows angular velocity fluctuations for a misfire in a cylinder of an inline 6-cylinder engine with a 1-5-3-6-2-4 ignition pattern. There are six uniform fluctuations in normal operation. As shown in the figure, if one of the cylinders misfires, the speed drops significantly and must be gradually rebuilt by the following cylinders [19].

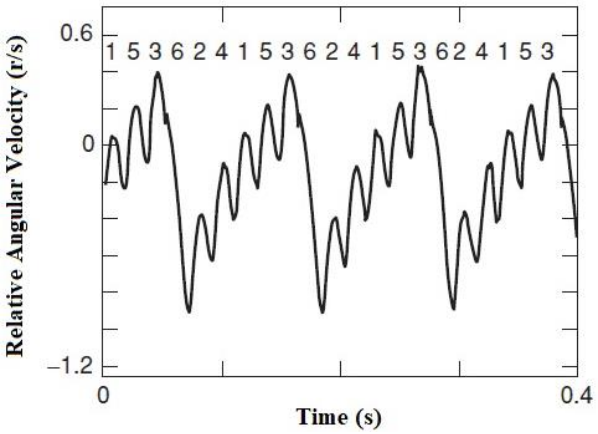

Fig. 2 The misfire in one cylinder and angular velocity fluctuates [19].

3.2 Experimental data

In this study, vibration signals obtained from 3 different cases of a 6-cylinder internal combustion engine were used [19]. Vibration signals were obtained from the engine block with an accelerometer located near the 6th cylinder. In the first case, the engine runs normally. In the second case, there is a misfire fault in one cylinder. In the third case, there are misfire faults in two cylinders. Misfire faults were achieved by removing the ignition cables. The firing order is 1–5–3–6–2–4. The sampling frequency for measurements in all cases is 24 000 Hz. Since the engine speed fluctuates, especially for faulty conditions, the signals containing the cycles are divided into shorter segments (32x1024). The average engine speed is nominally 1500 rpm. More detailed information can be found in the relevant reference [19].

3.3. Methodology

In this study, we applied two different methods for the detection of a healthy internal combustion engine (H) and faulty internal

combustion engines (single-cylinder misfire-F1, two-cylinder misfire-F2). In the first method, we extracted classical features from engine vibration signals and used them in training ANN and SVM. These features are mean (M), root mean square (RMS), standard deviation (SD), variance (VAR), kurtosis (K), and skewness (S). In the second method, we used CNNs, a deep learning method, to detect engine faults. We utilized spectrograms of engine vibration signals to train pre-trained CNNs with different structures. We used the short-time Fourier transform (STFT) to obtain the spectrograms.

3.3.1. The first method based on classical machine learning algorithms

The main purpose of feature extraction is to determine a set of quantitative coefficients to describe the distinctive abilities of the vibration signal characteristics in order to diagnose internal combustion engine faults. The features extracted from the signals are shown in Table 1.

Table 1 Features of the engine vibration signals

Property Name	Formula
Mean (M)	$M = \frac{1}{N}\sum_{i=1}^{N} x_i$
Root mean square (RMS)	$RMS = \sqrt{\frac{1}{N}\sum_{i=1}^{N} x_i^2}$
Standard deviation (σ, SD)	$SD = \sigma = \sqrt{\frac{1}{N}\sum_{i=1}^{N}(x_i - \bar{x})^2}$
Variance (σ^2, VAR)	$VAR = \sigma^2 = \frac{1}{N}\sum_{i=1}^{N}(x_i - \bar{x})^2$
Skewness (S)	$S = \frac{\sum_{i=1}^{N}(x_i - \bar{x})^3}{(N-1)\sigma^3}$
Kurtosis (K)	$K = \frac{\sum_{i=1}^{N}(x_i - \bar{x})^4}{(N-1)\sigma^4}$

ANN and SVM, which are used to detect engine faults using features in the first method, are among the most well-known modern machine-learning algorithms. ANN was developed with inspiration from the human brain and nervous system. In the ANN algorithm, artificial neurons process the features determined as input in the hidden layer and produce output about the engine faults. A two-layer feedforward neural network is used for the detection of engine faults. The number of hidden neurons was determined as 10 and the network was trained with the Levenberg-Marquardt backpropagation algorithm. SVM is also applied to classification and fault detection problems. This study, it is aimed to minimize the loss function while classifying the engine faults with SVM and to obtain the optimal hyperplane separating the classes in the best way. Since there is a lot of work in the literature on the mathematical details of SVM and ANN [21], no further information is given here. Input and target data for both ANN and SVM were randomly divided into three partitions. 70% of the data was used for training and 15% for validation. Finally, 15% of the data was used for a completely separate test.

3.3.2. The second method based on deep learning

Traditional machine learning methods rely on predefined features, while deep learning techniques, especially Convolutional Neural Networks (CNNs), excel at automatically learning complex data structures. CNNs effectively extract hierarchical features from raw data without extensive manual feature engineering, enhancing accuracy and reducing processing time. Their capability to handle large datasets makes them ideal for applications like fault detection, leading to more accurate and reliable results. Consequently, CNNs are increasingly favored for engine fault detection tasks over classical approaches.

The second method applied in this study is based on the STFT, which is one of the time-frequency analysis methods. We obtained the spectrograms from the motor vibration signals with STFT and used them to generate the dataset for the deep learning algorithm.

STFT is a Fourier-based transform used to determine the frequency and phase of local parts of the signal that change over time. With STFT, a long-time signal is split into short segments and the Fourier transform is implemented for each short segment separately to obtain the spectrogram. Finally, spectrograms are plotted as a function of time. In Eq. 1, x(t) represents the time signal, τ is the time axis, and ω is the frequency [22].

$$P_{Spektrogram,x}(\tau,\omega) = \left|STFT_x(\tau,\omega)\right|^2 \quad (1)$$

We used the spectrograms obtained with STFT to train pre-trained CNNs with different structures to detect engine faults. CNNs are a special subclass of ANNs, and classification with CNN is mostly performed on images. CNNs are a specially developed version of multilayer perceptrons. In multilayer perceptrons, each neuron in one layer is connected to all neurons in the next layer. CNN consists of convolutional and subsampling layers. Each of these layers has a specific topographic structure, and each layer contains different clusters of neurons. Each neuron is also linked to neurons in previous layers [22]. In Fig. 3, a typical CNN architecture is given. The input layer in the figure represents the spectrograms in our problem, and the output layer is the engine fault. The mathematical details of CNNs will not be given here as they have been extensively discussed in the literature [22].

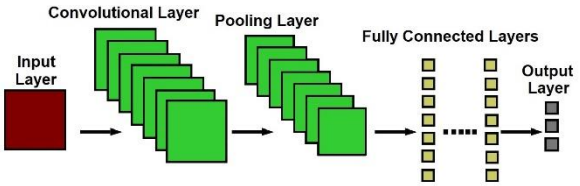

Fig. 3 Typical CNN architecture

Pre-trained CNNs are modified and applied to new classification problems. In this way, the time and effort required to train a network is much less than to train a network from scratch [23]. Detailed features of the pre-trained CNNs used in this study are given in Table 2. Also, Table 3 shows the training parameters.

Spectrograms of vibration signals for an healthy internal combustion engine (H) and faulty internal combustion engines (single-cylinder misfire-F1, two-cylinder misfire-F2) were obtained separately. The spectrograms obtained for each engine were divided into three groups as training (50%), test (25%), and validation (25%). CNN outputs are modified and changed to classify healthy and faulty engines. Using training and validation data, CNNs were trained on deep features, and faults were classified. Finally, the trained network was tested, and faults were diagnosed based on data labels.

4. Results and Discussion

4.1. Signal analysis

The representations of vibration signals obtained from H, F1, and F2 engines in the time and frequency domain can be seen in Fig. 4. Since the signal data is divided into 32 segments, these representations contain 1 out of 32 of the measurements used in the calculations. Accordingly, the frequency amplitudes of the vibration signals of the H engine are lower than the faulty engines. However, a more detailed examination can be made to extract the features of the signals.

Table 2 Features of the pre-trained CNNs

	GoogleNet	**ResNet-50**
Layer depth	22	50
Layer Number	144	177
Connection Number	170	192
Type of Input	Spectrogram	Spectrogram
Size of Input	224x224x3	224x224x3
Type of Output	Classification	Classification
Size of Output	3	3
Weight learning rate factor	10	10
Bias learning rate factor	10	10
The Loss Function	Cross-entropy	Cross-entropy

Table 3. Training parameters of pre-trained CNNs

	GoogleNet	**ResNet-50**
Frequency of Validation	5 Hz	
Rate of Learning	0.001	
Maximum Epoch	5	
Size of Mini Batch	10	
Input Data Resolution	483 x 430 pixel	

4.2. The Results of the First Method

Fig. 5 shows the different features of vibration signals of healthy and faulty internal combustion engines. Accordingly, looking at the M values, it can be seen that the F2 engine produces the highest features. The H engine produced the lowest M values. Looking at the RMS values, it can be seen that the H engine produces the highest features. The F1 engine produced the lowest RMS values. There is a similar trend for SD and VAR features. Looking at the S values, it can be seen that the F2 engine produces the highest features. The F1 engine produced the lowest S values. K features were close to each other for all three engines.

All these features are used to create the dataset that is organized to detect motor failure with ANN and SVM.

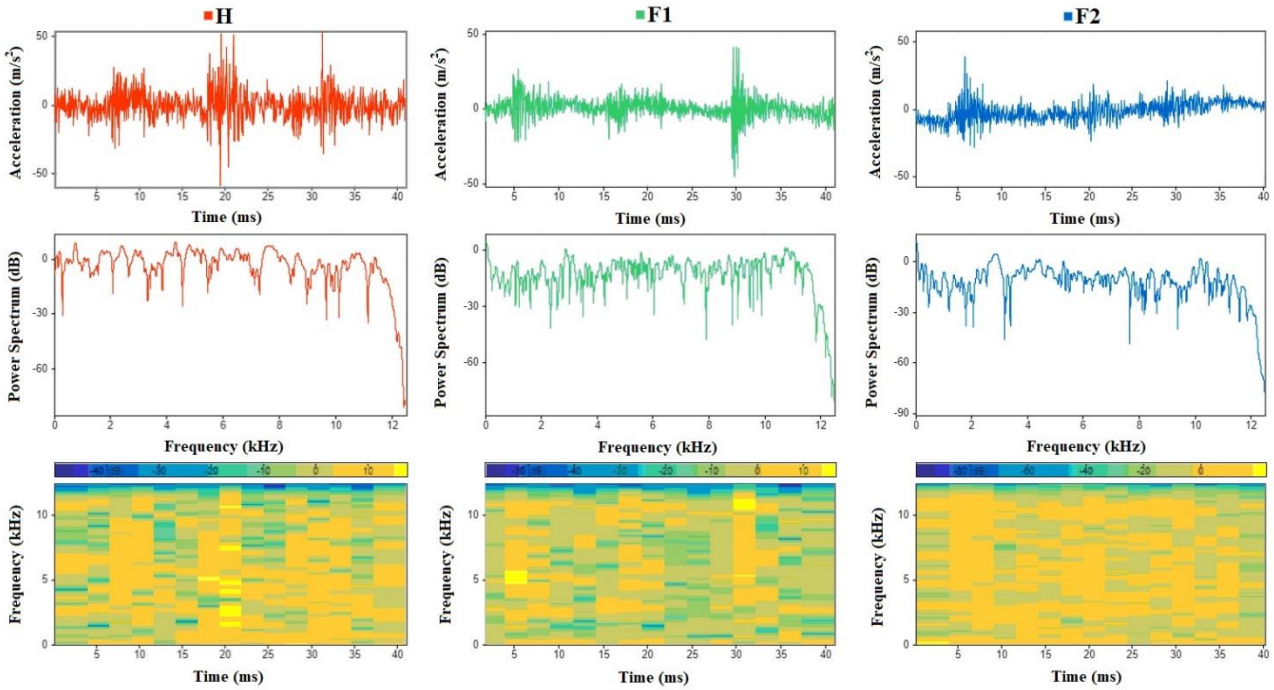

Fig. 4 Time and frequency domain representations and spectrograms of internal combustion engines vibration signals

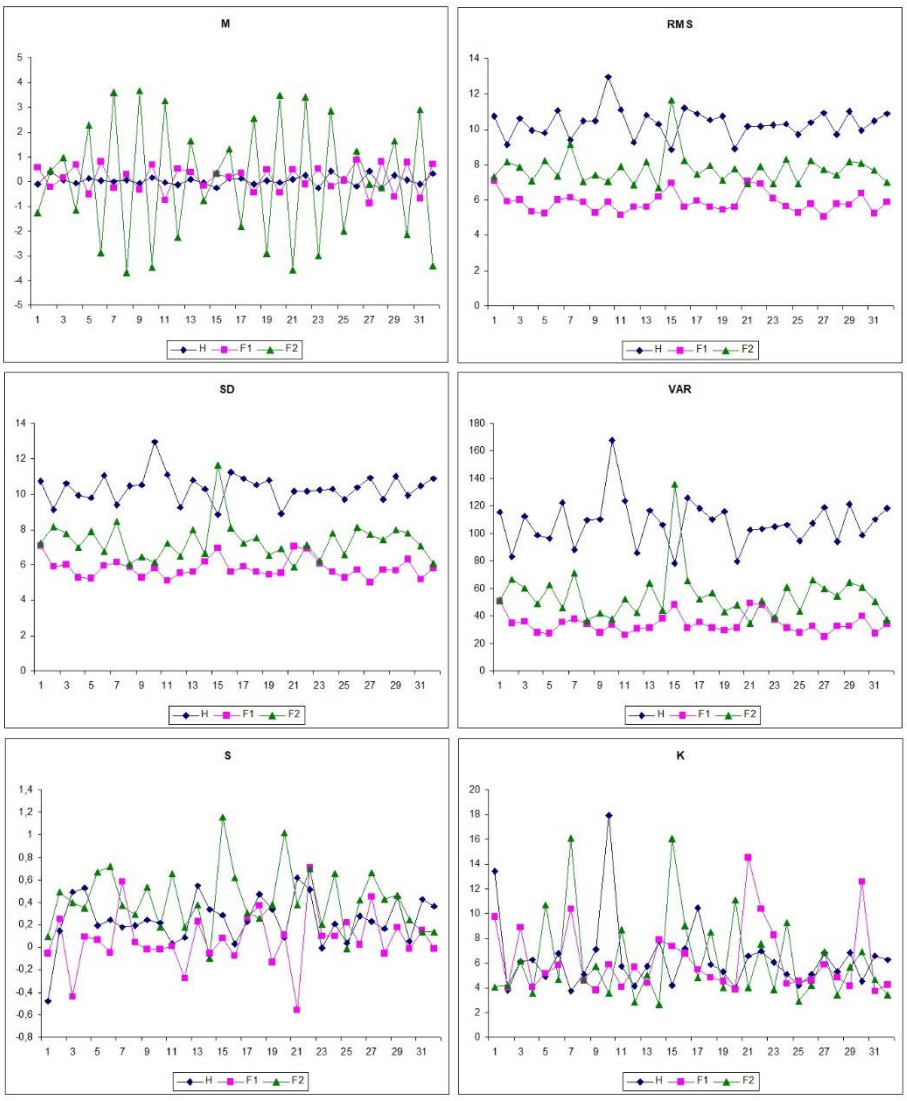

Fig. 5 Different features of vibration signals of healthy and faulty internal combustion engines

Fig. 6 shows the training, validation, and test performances of the ANN model. Accordingly, the best validation performance is 0.043846 at epoch 11. Fig. 7 shows the training, validation, and test confusion matrices of the ANN model. Looking at the all confusion matrix, it can be seen that the overall success rate of the model is 97.9%.

In this study, features extracted from the vibration signals of engines are also used in training SVM models. In order to avoid figure redundancy, the results of the SVM models are given directly. As can be seen from Table 4, all SVM models achieved a validation success of 95.8%.

4.3. The results of the second method

The CNNs used in this study were adapted to the problem of engine diagnostics and trained with spectrograms obtained from vibration signals. At the end of the training, validation success, loss, and gradient values were calculated. Finally, the successes of the tested CNNs with the data set reserved for the test were compared with each other. For CNN models, the goal is to identify healthy and faulty engines. Table 5 shows the class labels of the engines and the number of samples utilized for the training, validation, and test of different CNN models.

Table 4. Results of training of SVM models

SVM Models	Validation Accuracy (%)
Linear	95.8
Quadratic	95.8
Cubic	95.8
Gaussian	95.8

Table 5. Class labels and sample numbers

Class Label	H	F1	F2
Training Samples	22	22	22
Validation Samples	10	10	10
Test Samples	10	10	10

Fig. 8 demonstrates the accuracy rates for two different CNN models. Accordingly, GoogleNet and ResNet-50 models reached a 100% validation rate at the end of the training process. Since the number of layers and connections of the ResNet-50 model is higher, the training time is longer. With all other conditions remaining the same, the increase in complexity in the CNN architecture positively affects the accuracy rate and increases the training time.

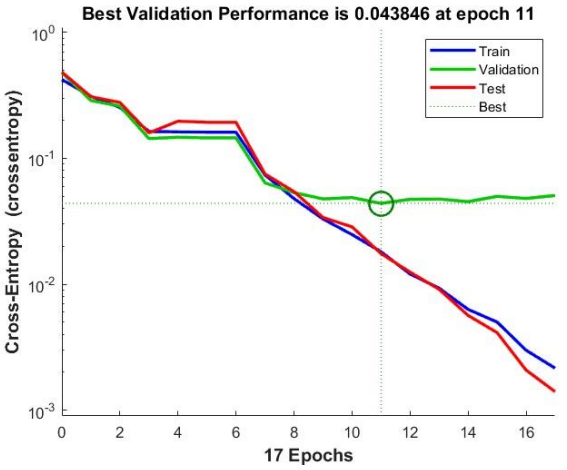

Fig. 6 Training, validation, and test performances of the ANN model

Fig. 7 Training, validation, and test confusion matrices of the ANN model

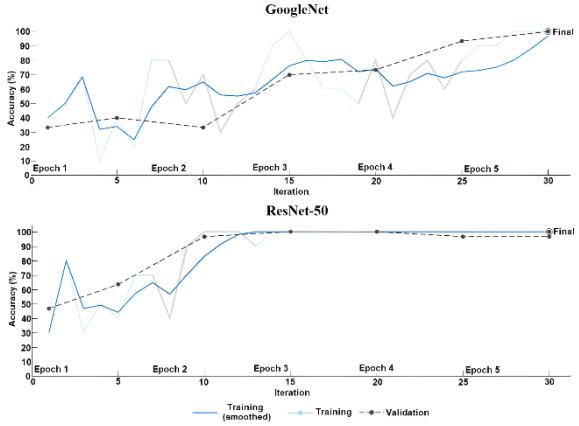

Fig. 8 Accuracies for different CNN models

The losses in training and validation processes

for different CNN models can be seen in Fig. 9. Losses are a measure of the difference between the estimated output and the actual output. Losses decrease with the number of iterations. The loss values of the models decreased over time due to the variation in the validation rates during the training period.

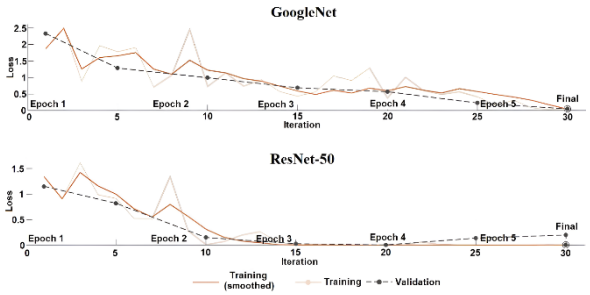

Fig. 9 Losses for different CNN approaches

The success rates of CNN models trained and tested with different numbers of samples can be seen in Table 6. Accordingly, as the number of samples increases, the validation and test successes, and training times of the two CNN models increase. It can be seen from the table that the training time of CNNs with more complex architecture such as Resnet-50 will be longer.

The performance of the CNN models, as shown in the table, indicates that both GoogleNet-CNN and ResNet-CNN achieve 100% validation success with an increase in training samples, which is a promising result. However, strong correlations between input and output data can sometimes lead to success without overfitting, especially with smaller datasets—this raises concerns about the models' generalization ability. The tendency of the models to memorize training data may limit their performance on different engine types or fault conditions. Therefore, it is crucial to consider strategies that enhance robustness and generalizability, such as adding more data or employing regularization techniques, to ensure reliable performance across diverse scenarios and validate results against various datasets.

In this context, the study contributes to the diagnosis of internal combustion engine faults by utilizing both classical machine learning methods (SVM and ANN) and deep learning techniques (CNN). It was observed that ANN achieved a success rate of 97%, outperforming SVM, while the ResNet-50 architecture also achieved a diagnostic performance of 100%. This underscores the potential of deep learning methods in this field. In contrast to most existing literature, such as Jafarian et al. [2] and Moosavian et al. [4], which primarily focus on classical machine learning approaches, this study suggests that integrating both classical and modern methods may enhance fault detection capabilities.

5. Conclusions

In this study, classical machine learning methods and CNNs were used for the diagnosis of internal combustion engines with different faults. While SVM and ANN are applied for fault diagnosis, classical features obtained from vibration signals are used for training purposes. Spectrograms were preferred when applying CNN models. The results obtained from the ANN and SVM models were compared. Accordingly, ANN performed better than SVM (97%). Two CNN models with different architectures showed similar diagnostic performance (100%). However, higher test success was achieved with the more complex Resnet-50. This model, which has a more complex architecture, has a longer training duration. As a result, it is seen that classical machine learning and deep learning algorithms can effectively classify the misfire faults of internal combustion engines.

Table 6 Sample number effect on CNN performance

CNNs	Number of Training Samples	Validation Success (%)	Test Success (%)	Training Duration (s)
GoogleNet-CNN	11	85	80	40
GoogleNet-CNN	22	100	95	81
GoogleNet-CNN	44	100	100	160
ResNet-50-CNN	11	90	90	90
ResNet-50-CNN	22	100	100	180
ResNet-50-CNN	44	100	100	160

6. References

1. Aliramezani, M., Koch, C.R. and Shahbakhti, M., "Modeling, diagnostics, optimization, and control of internal combustion engines via modern machine learning techniques: A review and future directions", Progress in Energy and Combustion Science, 88, 100967, 2022. https://doi.org/10.1016/j.pecs.2021.100967
2. Jafarian, K., Mobin, M., Jafari-Marandi, R. and Rabiei, E., "Misfire and valve clearance faults detection in the combustion engines based on a multi-sensor vibration signal monitoring", Measurement, 128, pp. 527-536, 2018. https://doi.org/10.1016/j.measurement.2018.04.062
3. Li, Z., Yan, X., Yuan, C., and Peng, Z. "Intelligent fault diagnosis method for marine diesel engines using instantaneous angular speed", Journal of Mechanical Science and Technology, 26, pp. 2413-2423, 2012. https://doi.org/10.1007/s12206-012-0621-2
4. Moosavian, A., Khazaee, M., Najafi, G., Kettner, M. and Mamat, R., "Spark plug fault recognition based on sensor fusion and classifier combination using Dempster–Shafer evidence theory", Applied Acoustics, 93, pp. 120-129, 2015. https://doi.org/10.1016/j.apacoust.2015.01.008
5. Sharma, A., Sugumaran, V. and Devasenapati, S.B., "Misfire detection in an IC engine using vibration signal and decision tree algorithms", Measurement, 50, pp. 370-380, 2014. https://doi.org/10.1016/j.measurement.2014.01.018
6. Devasenapati, S.B., Sugumaran, V. and Ramachandran, KI., "Misfire identification in a four-stroke four-cylinder petrol engine using decision tree", Expert systems with applications, 37, 3, pp. 2150-2160, 2010. https://doi.org/10.1016/j.eswa.2009.07.061
7. Castresana, J., Gabiña, G., Martin, L., Basterretxea, A. and Uriondo, Z., "Marine diesel engine ANN modelling with multiple output for complete engine performance map", Fuel, 319, 123873, 2022. https://doi.org/10.1016/j.fuel.2022.123873
8. Wang, W., Li, Y. and Song, Y., "Fault diagnosis method of vehicle engine via HOSVD–HOALS hybrid algorithm-based multi-dimensional feature extraction", Applied Soft Computing, 116, 108293, 2022. https://doi.org/10.1016/j.asoc.2021.108293
9. Cai, B., Sun, X., Wang, J., Yang, C., Wang, Z., Kong, X. and Liu, Y., "Fault detection and diagnostic method of diesel engine by combining rule-based algorithm and BNs/BPNNs", Journal of Manufacturing Systems, 57, pp. 148-157, 2020. https://doi.org/10.1016/j.jmsy.2020.09.001
10. Kowalski, J., Krawczyk, B. and Woźniak, M., "Fault diagnosis of marine 4-stroke diesel engines using a one-vs-one extreme learning ensemble", Engineering Applications of Artificial Intelligence, 57, pp. 134-141, 2017. https://doi.org/10.1016/j.engappai.2016.10.015
11. Karatuğ, Ç. and Arslanoğlu, Y., "Development of condition-based maintenance strategy for fault diagnosis for ship engine systems", Ocean Engineering, 256, 111515, 2022. https://doi.org/10.1016/j.oceaneng.2022.111515
12. Flett, J. and Bone, G.M., "Fault detection and diagnosis of diesel engine valve trains", Mechanical Systems and Signal Processing, 72, pp. 316-327, 2016. https://doi.org/10.1016/j.ymssp.2015.10.024
13. Wang, X., Liu, C., Bi, F., Bi, X. and Shao, K., "Fault diagnosis of diesel engine based on adaptive wavelet packets and EEMD-fractal dimension", Mechanical Systems and Signal Processing, 41, 1-2, pp. 581-597, 2013. https://doi.org/10.1016/j.ymssp.2013.07.009
14. Basurko, O.C. and Uriondo, Z., "Condition-based maintenance for medium speed diesel engines used in vessels in operation", Applied Thermal Engineering, 80, pp. 404-412, 2015. https://doi.org/10.1016/j.applthermaleng.2015.01.075
15. Küçüksarıyıldız, H., Çarman, K., Sabancı, K. "Prediction of specific fuel consumption of 60 HP 2WD tractor using artificial neural networks", International Journal of Automotive Science And Technology, 5, 4, pp. 436-444, 2021. https://doi.org/10.30939/ijastech..1010318

16. Togun, N. K., Baysec, S. “Prediction of torque and specific fuel consumption of a gasoline engine by using artificial neural networks”, Applied Energy, 87, 1, pp. 349-355, 2010. https://doi.org/10.1016/j.apenergy.2009.08.016
17. Çay, Y., Çiçek, A., Kara, F., Sağiroğlu, S. “Prediction of engine performance for an alternative fuel using artificial neural network”, Applied Thermal Engineering, 37, pp. 217-225, 2012. https://doi.org/10.1016/j.applthermaleng.2011.11.019
18. Parlak, A., Islamoglu, Y., Yasar, H., Egrisogut, A. “Application of artificial neural network to predict specific fuel consumption and exhaust temperature for a diesel engine”, Applied Thermal Engineering, 26, 8-9, pp. 824-828, 2006. https://doi.org/10.1016/j.applthermaleng.2005.10.006
19. Randall, R.B., “Vibration-based condition monitoring: industrial, automotive and aerospace applications”, John Wiley & Sons, 2011. http://www.wiley.com/go/randall
20. Tharanga, K.P., Liu, S., Zhang, S. and Wang, Y., “Diesel engine fault diagnosis with vibration signal”, Journal of Applied Mathematics and Physics, 8, 9, pp. 2031-2042, 2020. https://doi.org/10.4236/jamp.2020.89151
21. Karabacak, Y.E., Özmen, N.G. and Gümüşel, L. “Intelligent worm gearbox fault diagnosis under various working conditions using vibration, sound and thermal features”, Applied Acoustics, 186, 108463, 2022. https://doi.org/10.1016/j.apacoust.2021.108463
22. Karabacak, Y.E., Gürsel Özmen, N. and Gümüşel, L., “Worm gear condition monitoring and fault detection from thermal images via deep learning method”, Maintenance and Reliability, 22, 3, pp. 544-556, 2020. http://dx.doi.org/10.17531/ein.2020.3.18
23. Karabacak, Y.E. and Gürsel Özmen, N. “Rulmanlarda titreşim verilerinden durum izleme ve arıza teşhisi için derin öğrenme yönteminin uygulanması”, Konya Journal of Engineering Sciences, 10, 2, pp. 346-365, 2022. https://doi.org/10.36306/konjes.1049489

e-ISSN: 2146 - 9067

International Journal of Automotive Engineering and Technologies

journal homepage:
https://dergipark.org.tr/en/pub/ijaet

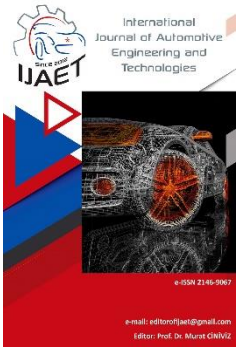

Original Research Article

Investigation of the role of methane injection timing and pressure on engine performance, emissions and environmental impact in a diesel engine

Halil Erdi Gülcan [1*]

[1,*] Mechanical Engineering Department, Faculty of Technology, Selcuk University, Konya, 42250, Türkiye.

ARTICLE INFO

Orcid Numbers

1. 0000-0002-2328-5809

Doi: 10.18245/ijaet.1554225

* Corresponding author
halil.gulcan@selcuk.edu.tr

Received: Sep 22, 2024
Accepted: Oct 30, 2024

Published: 31 Dec 2024

Published by Editorial Board Members of IJAET

ABSTRACT

Methane diesel dual-fuel engines are gaining increasing interest because they offer lower emissions and higher efficiency compared to conventional single-diesel fuel engines. However, due to the low combustion efficiency and combustion stability of the methane-diesel dual-fuel application, there are still unresolved issues that need to be addressed. In this study, the effects of methane gas injection timing and pressure on engine performance and exhaust emissions are investigated in order to overcome problems related to the application of methane gas in dual-fuel engines. Additionally, the environmental and economic impacts of the exhaust emissions resulting from combustion are analyzed. The study is conducted with 5 different methane gas injection timings (25, 35, 45, 55, and 65 degrees after TDC) and 4 different methane gas injection pressures (1 bar, 1.5 bar, 2 bar, and 2.5 bar). In the experiments, the engine torque (5 Nm) and operating speed (1850 1/min) are kept constant. The results show that increasing the methane gas injection pressure (GIP) from 1 bar to 2.5 bar and delaying the methane gas injection timing (GIT) from 25° aTDC to 65° aTDC leads to an average reduction of 8.5% in SFC values and a 4% increase in thermal efficiency compared to diesel operation. Similarly, increasing GIP and delaying GIT results in an average reduction of 46% in NO emissions and an average reduction of 48% in soot emissions.

Keywords: Diesel-methane dual fuel, Engine performance, Emissions, Gas injection timing and pressure, environmental impacts

1. Introduction

The use of internal combustion engines (ICE) in transportation, agriculture, maritime sector, and industrial areas significantly contributes to the formation of greenhouse gas emissions (especially carbon dioxide) and air pollution [1-3]. The primary cause of this situation is the use of fossil-derived fuels in ICE [4]. Today, in many countries, stringent emission standards are enforced to reduce the release of harmful gases resulting from the use of fossil-derived fuels. This situation compels motor manufacturers and researchers to make various improvements in both pre-combustion and post-combustion in ICE [5, 6]. At the forefront of these improvements is the use of alternative

fuels that do not involve significant structural changes for the engine [7]. Among the alternative fuels, gaseous fuels like methane [8, 9], H_2 [10, 11], and liquid fuels like biodiesel [12-15], alcohols [16-18], and wastes [19] are prominent.

Due to the potential for methane gas to be produced from biomass such as municipal waste, sludge, and trash, it is becoming increasingly important for both electricity generation and use in ICEs in the coming years [20]. Consequently, various studies are being conducted to increase the use of methane in both gasoline and diesel engines. Methane can be used directly in gasoline engines because it can be ignited by an external ignition source. However, in diesel engines, methane can either be used directly through a special injection system or, alternatively, in a dual-fuel mode without significant modifications to the engine [21]. In diesel engines, the use of methane is primarily implemented in dual-fuel mode due to its economic advantages and minimal modification requirements. In dual-fuel mode, methane is introduced into the combustion chamber during the intake phase and is injected onto the gas-air mixture at the end of the compression phase to create the diesel ignition source [22, 23].

In literature, it is possible to find various studies on the use of methane gas in diesel engines. Some of these studies are summarized as follows: Krishnan and colleagues [24] investigated the effects of different natural gas additions on performance in a diesel engine. They reported that as the natural gas ratio increased from 0% to 90% in the dual-fuel application, the engine efficiency tended to decrease. However, it was also noted that the increase in natural gas ratio led to a reduction in NO_x and smoke emissions. Papagiannakis and Hountalas [25] conducted an experimental study on the effects of natural gas ratio on performance and emissions in a natural gas-diesel dual-fuel engine. The experiments were carried out under different load conditions and natural gas energy ratios. The results showed that increasing the percentage of natural gas reduced NO and smoke emissions but significantly increased HC and CO emissions. Additionally, it was reported that the BSFC values tended to increase with a higher natural gas percentage. Di Blasio and colleagues [26] reported that increasing the methane energy ratio from 0% to 50% in a methane-diesel dual-fuel application resulted in a threefold increase in HC emissions and a tenfold increase in CO emissions. The study also highlighted those changes in the compression ratio that had a significant impact on HC and CO emissions. Chen and colleagues [27] investigated the effects of water injection on the performance and emissions of an engine operating on a diesel-methane fuel mix. The methane energy ratio in the study varied from 0% to 50% in five different configurations. The results indicated that an increase in the methane content of the mixture significantly reduced NO_x emissions, but HC and CO emissions increased. It was also emphasized that water port injections did not significantly affect HC and CO emissions. Ouchikh and colleagues [28] investigated the effects of diesel injection parameters on the performance and emissions of a diesel engine operating with a methane-diesel dual-fuel system. The results indicated that while thermal efficiency decreased with the diesel injection timing in dual-fuel operation, thermal efficiency increased with the split injection strategy. Additionally, it was noted that the split injection strategy resulted in a 20% reduction in brake specific fuel consumption (BSFC). However, HC and CO emissions showed significant increases compared to baseline diesel fuel. Tripathi and colleagues [29] found that in a diesel engine, increasing the methane energy ratio from 0% to 75% resulted in a gradual decrease in thermal efficiency. Additionally, it was observed that HC emissions increased by approximately 10 times and CO emissions by about 5 times with the rise in methane energy ratio. On the other hand, a maximum reduction of around 50% in NO_x emissions was also reported. Ahmad and colleagues [30] focused on the effects of using different proportions of ethane gas on the performance and emissions in a methane-diesel dual-fuel application. Ethane gas was used at 10% and 20% concentrations in the dual-fuel system. The results showed that the addition of ethane gas improved thermal efficiency, which had decreased with the use of methane gas. While the addition of ethane contributed to a reduction in HC emissions, it

also led to an increase in NO_x emissions. Liu and colleagues [31] reported that increasing the diesel fuel ratio in a methane-diesel dual-fuel application would be beneficial for methane oxidation by raising the high-temperature regions within the cylinder. Di lorio et al. [32] reported in their study on methane-diesel dual fuel application that methane gas uses significantly reduced NO_x and smoke emissions compared to diesel-only operation. Khedkar et al. [33] focused on the effects of control parameters such as diesel injection timing, EGR control, and intake throttling on the low thermal and combustion efficiency of a methane-diesel engine. The results showed that with 55% EGR, 50% premix, and advanced diesel injection timing, thermal efficiency (TE) improved by approximately 10%, and combustion efficiency also increased. Additionally, it was emphasized that HC and NO_x emissions were significantly reduced. Zarrinkolah and Hosseini [34] utilized both the traditional methane-diesel dual-fuel mode and early and late injection RCCI modes to reduce methane emissions. The results indicated a reduction in methane emissions ranging from 12% to 33% in early and late RCCI modes compared to traditional operation. However, it was also found that the early and late RCCI modes produced soot particulate emissions approximately 417% and 67% higher, respectively. Cameretti and colleagues [35] conducted a numerical analysis of a hydrogen-methane mixture in a marine diesel engine. The results indicated that using hydrogen instead of methane reduces CO_2 emissions by 54%, while increasing NO_x emissions by 76%. Yin and colleagues [36] conducted experimental and numerical studies on a diesel/methane/hydrogen fueled engine. They reported that an increase in the hydrogen fraction within the triple mixture enhances the combustion process, reducing both ignition delay and combustion duration. It was also noted that this leads to an increase in NO_x emissions while resulting in a decrease in CO and CH_4 emissions. Zhang and colleagues [37] studied the diesel injection timing in a natural gas-diesel engine. They reported that advancing the diesel injection timing resulted in improved performance and enhanced flame development. However, it was also noted that this condition increased CH_4 emissions by approximately 4% and NO_x emissions by about 6%.

Based on the summaries of the studies presented in the literature, it is evident that the use of methane in diesel engines significantly reduces NO_x and smoke emissions, while increasing HC and CO emissions. Additionally, some studies report a deterioration in thermal efficiency and fuel consumption with methane gas usage. This indicates that engines utilizing methane-diesel fuel are still open to improvements and have unresolved issues that need to be addressed. Also, while some studies contribute to the reduction of HC emissions, this simultaneously leads to an increase in NO emissions. Therefore, it appears that research will continue to improve the operational efficiency of methane in diesel engines. In the current study, the effects of varying gas injection timing and pressure on engine performance, exhaust emissions, and environmental impact are investigated to enhance the usability of methane gas in diesel engines. When reviewing other studies, it is observed that very few focus on gas injection timing, and most of these studies primarily emphasize performance. However, the significant reduction of NO emissions resulting from the use of methane in diesel engines necessitates an examination from the perspective of environmental and economic impact analysis to enhance environmental sustainability and raise awareness. Additionally, there is a significant gap in literature regarding this area. The aim of this study is to examine performance, emissions, and environmental impact parameters under various conditions of methane gas injection timing and pressure in diesel engines.

2. Experimental Setup and Method

2.1. Experimental setup

The methane-diesel dual-fuel application conducted at different gas injection timings and pressures is carried out on a single-cylinder, air-cooled, 4-stroke diesel engine. The single-cylinder, 315 cc volume diesel engine used in the study is selected based on contemporary 4-cylinder diesel engines. When

the total volume of the 4-cylinder diesel engine (1248 cc/4 cylinders = 312 cc) is divided by the number of cylinders, the resulting volume is nearly equivalent to the volume of the single-cylinder engine used in the study. Additionally, due to the CRDI systems present in modern diesel engines, the fuel system on the existing engine is similarly modified. This adaptation ensures that the findings are more realistic, as the current single-cylinder engine has been tailored to align with more modern diesel engines. Therefore, the air-cooled AD320 Anadolu engine was chosen for experimentation as the most suitable single-cylinder engine for both modification and the dual-fuel concept. A summary of the engine's technical specifications is presented in Table 1. Additionally, the experimental equipment and engine installation view are presented in Fig. 1. In the air-cooled engine, a common rail fuel system and an ECU are used to control the amount, pressure, and injection timing of the diesel fuel. The gas fuel system injected fuel into the combustion chamber through port injection. The gas pressure is adjusted to the desired level using a two-stage pressure regulator on the methane gas cylinder. Additionally, the gas injection timing was controlled by the gas ECU. Detailed stages of both the diesel fuel system and the gas fuel system have been presented in previous studies [6, 8]. For the performance and emission tests of the engine used in the experiments, the engine is first mounted on an ABB brand DC dynamometer capable of measuring up to 50 kW of power and 6000 1/min. Methane gas consumption is measured instantaneously and cumulatively using a gas flow meter. Similarly, air consumption is also measured instantaneously and cumulatively with an air flow meter. Diesel fuel consumption is calculated based on the rate set through the ECU in mg/cycle. Details of the measurement equipment used in the experiments are presented in Table 2.

Table1. Technical details of the dual-fuel engine used at variable gas injection timing and pressure variations [38].

Technical details	Value/AD320 diesel engine
Cylinder number	1-cylinder
Displacement	0.315 lt
Bore diameter	78 mm
Stroke diameter	66 mm
Compression ratio	17.3
Peak engine torque (at speed)	11 Nm (at 1850 1/min)
Diesel fuel system	**Common rail** Injection timing: 11° bTDC Injection pressure: 400 bar
Gas supply system	**Port injection** Injection timing: 25°, 35°, 45°, 55°, and 65° aTDC Injection pressure: 1, 1.5, 2, and 2.5 bar

Emission data measurements are conducted using a Bosch-branded emission system.

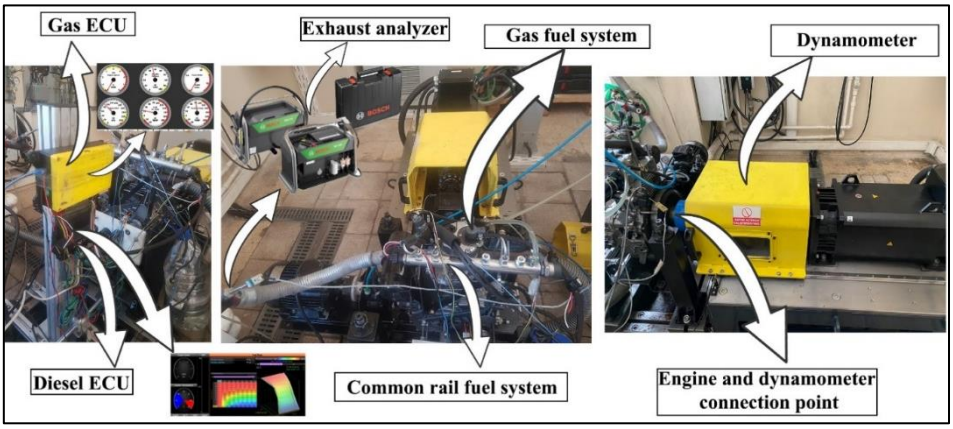

Fig. 1. View of test equipment and engine installation

Table 2. Details of the measurement equipment.

Test Instruments	Measurement	Measure range	Sensibility
ABB DC Dynamometer	Load/speed	0..50 kW/0..6000 rpm	± 0.01 rpm
Sierra SmartTrak 100	Methane flow meter	0..50 slpm	± 1.0%
Pietro Fiorentini series-c	Air flow meter	0..4.4 liter/s	± 1.0%
K type thermocouple	Temperature	0..850 °C	± 1.0 °C

Table 3. Technical specifications of the Bosch brand emission device utilized in the experiments [6].

Data type(method)	Measure range	Sensibility
CO (Non-dispersive infrared)	0..10% volume	±0.001%
HC (Flame ionization detector)	0..9999 ppm	±1 ppm
NO (Chemiluminescence detector)	0..5000 ppm	±1 ppm
Soot (Optical meter)	0..9.99 1/m	±0.01 1/m

Table 4. The physicochemical details of diesel and methane fuels [6].

Physicochemical details	Euro diesel	Methane (purity 99.5%)
Density, g/cm^3	0.83–0.84	0.000678
Lower calorific value, kJ/kg	42500	50000
Octane number	-	<120
Cetane number	50-55	-
Air/fuel (Stoichiometric)	14.6	17.4

Table 5. The detailed test matrix for the study.

Case	Fuel	Torque/Speed	Gas injection timing (GIT)	Gas injection pressure (GIP)
1	Euro Diesel	5 Nm/1850 rpm	-	-
2	Dual fuel	5 Nm/1850 rpm	25º aTDC	1, 1.5, 2, and 2.5 bar
3	Dual fuel	5 Nm/1850 rpm	35º aTDC	1, 1.5, 2, and 2.5 bar
4	Dual fuel	5 Nm/1850 rpm	45º aTDC	1, 1.5, 2, and 2.5 bar
5	Dual fuel	5 Nm/1850 rpm	55º aTDC	1, 1.5, 2, and 2.5 bar
6	Dual fuel	5 Nm/1850 rpm	65º aTDC	1, 1.5, 2, and 2.5 bar

The Bosch Bea060 model is used to quantify HC, CO, and NO emissions, while the Bea070 model measures soot opacity levels. Detailed specifications and sensitivities of these devices are thoroughly presented in Table 3.

For the experimental study, diesel fuel and pure methane gas are sourced from local suppliers. The physicochemical details of these fuels are presented in Table 4.

2.2. Method

Before conducting experiments on methane injection timing and pressure, the engine is run on baseline diesel fuel at idle condition until it reaches a stable combustion. Subsequently, the load and speed for the engine tests are set using a computer-controlled dynamometer, and the experiments commence. Additionally, during the experiment process, careful attention is given to managing the engine's surface temperature, considering the possibility of excessive temperature (>200ºC) increases that could affect the reliability of the test results. Before the experiments, the calibration of the Bosch emission device, ABB DC dynamometer, and other measurement equipment is prepared and ensured to be ready. The experiments are initially conducted using EURO diesel fuel at 5 Nm and a constant speed of 1850 1/min. The engine speed determined in the study is also the speed at which maximum engine torque is achieved. Additionally, a vehicle equipped with a diesel engine (either passenger or light commercial) generally operates in the range of 1500 to 2200 rpm under daily traffic conditions. Considering this speed range, an engine speed of 1850 rpm aligns with the movement speed of a vehicle in daily traffic. The engine torque is defined as medium load, as most vehicles operate under low to medium loads in traffic conditions. Subsequently, methane-diesel dual-fuel experiments are carried out. In these experiments, methane gas injection timing (GIT) occurs 25º aTDC through port injection at a pressure of 1 bar. Following this, experiments for GIT25 are completed at gas injection pressures (GIP) of 1.5 bar, 2 bar, and 2.5 bar. The same procedures are then followed for the experiments at GIT35, GIT45, GIT55, and GIT65, respectively. Previous studies [6, 8] have identified that early injection of methane causes various problems such as low volumetric efficiency and combustion temperatures. Therefore, it was decided to delay the GIT from 25º aTDC to 65º aTDC, considering that later injection could address the low volumetric efficiency issue. The flow diagram of the experimental process is presented in Fig. 2. Also, the detailed test matrix for the study is presented in Table 5.

In the methane-diesel dual-fuel combination,

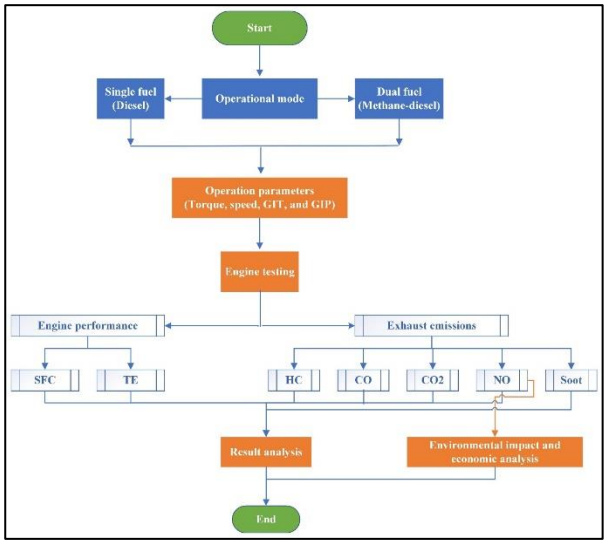

Fig. 2. The flow diagram of the experimental process

the percentage of methane gas sent to the combustion chamber, referred to as gas energy percentage (GEP), can be calculated using Eq. (1) [39]. Fig. 3 presents the contribution to total fuel energy of methane and diesel fuel corresponding to different GIT and the associated GIP.

$$GEP = \left[\frac{\dot{m}_{gas} LCV_{gas}}{\dot{m}_{gas} LCV_{gas} + \dot{m}_{diesel} LCV_{diesel}}\right] x100 \quad (1)$$

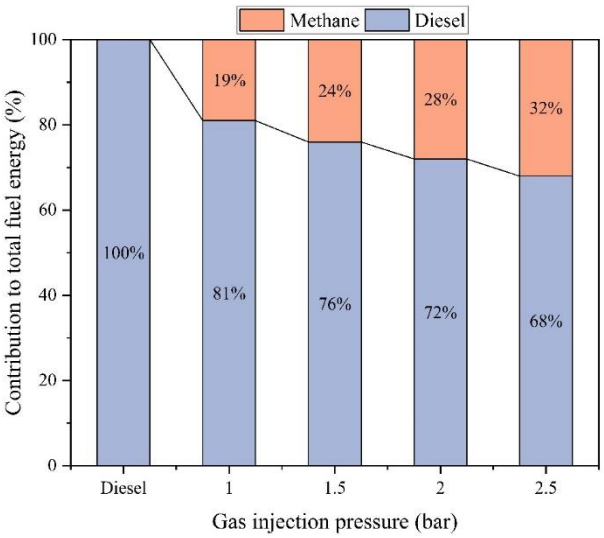

Fig. 3. The contribution to total fuel energy of methane and diesel fuel.

2.3. Environmental and economic impact analysis

A significant issue with diesel engines is the high levels of NO_x emissions they release into the environment. However, the use of methane gas as a dual fuel in diesel engines contributes to minimizing this problem. Evaluating such an important development from both environmental and economic perspectives is crucial for understanding its impacts. The analysis of these environmental and economic impacts is crucial for enhancing environmental awareness and sustainability. This study evaluates the environmental and economic effects of NO_x emissions generated from both diesel and methane-diesel combustion. To determine the environmental impact of NO_x emissions (EN_{NOx}), Eq. (2) [40] can be used. Here, $\dot{m}_{exh}$ represents the exhaust mass flow (kg/s) and en_{Nox} denotes the environmental impact coefficient.

$$EN_{NOx} = \dot{m}_{exh}\, x\, en_{Nox} \quad (2)$$

In addition, the economic impact of NO_x emissions (EC_{NOx}) can be calculated using Eq. (3) [41], where eco represents the environmental-economic impact coefficient of NO_x emissions (eco_{Nox}).

$$EC_{NOx} = \dot{m}_{exh}\, x\, eco_{Nox} \quad (3)$$

The en_{Nox} and eco_{Nox} coefficients given in Eq. (2) and Eq. (3) are used in the calculations as 2.749 mPts/g and 693.7 €/g, respectively [42].

3. Results and discussion

3.1. Impact of GIT and GIP on performance

Fig. 4 shows the variation of specific fuel consumption (SFC) corresponding to different GIT and GIP. Both methane gas injection timing (GIT) and methane gas injection pressure (GIP) positively affect SFC. The lowest SFC values are obtained in dual-fuel mode with GIP 2.5 bar operation, while the highest SFC outputs are obtained with diesel fuel. For instance, under GIP 1 bar conditions, GIT 25 reduces SFC by 1% compared to diesel fuel, while delaying GIT to 65° aTDC contributes to a 3.5% reduction in SFC. Similarly, under GIP 2.5 bar conditions, GIT 25° reduces SFC by 6% compared to diesel fuel, and delaying GIT to 65° aTDC increases the SFC reduction to 12%. The main reasons for the reduction in SFC with methane use in the dual-fuel concept are the combined energy utilization of diesel and methane gas, as well as methane's higher lower heating value compared to diesel. Overall, when GIT changes from 25° to 65°, SFC decreases by an average of 2.5%, 6%, 7%, and 8.5% compared to diesel combustion for GIP 1 bar, GIP 1.5

bar, GIP 2 bar, and GIP 2.5 bar operations, respectively.

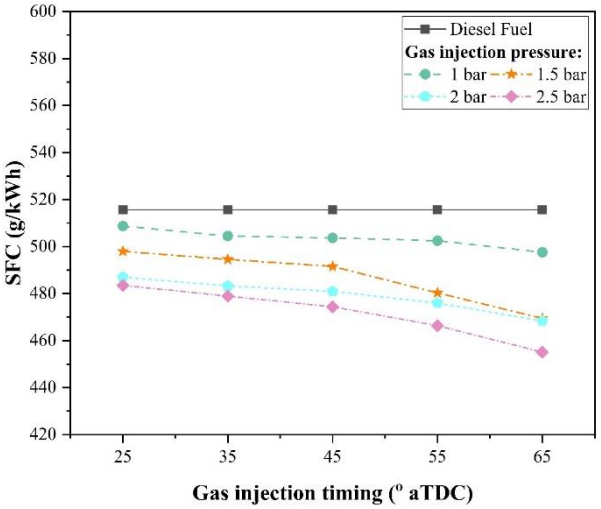

Fig. 4. The variation of SFC at different GIT versus GIP.

Fig. 5 shows the variation of thermal efficiency (TE) corresponding to different GIT and GIP. The use of methane in diesel engines contributes to an increase in TE. Additionally, the gradual delay of GIT also supports the increase in TE. The highest TE is obtained under GIP 2.5 bar conditions, and the TE outputs of GIP 2.5 bar and GIP 2 bar operations are quite similar. The lowest TE is observed under GIP 1 bar conditions (except for GIT 65). The implementation of the methane-diesel dual-fuel system based on energy ratio contributes to the reduction of SFC values. This also affects the reduction in TE. The reason for the lower TE in the GIP 1 bar operation between GIT 25 and GIT 55 compared to diesel fuel is that the fuel consumption amounts are quite similar. As the reduction rate in fuel consumption increases, TE gradually improves. Additionally, advancing the GIT causes the methane gas to block the incoming air into the cylinder, resulting in less air entering the combustion zone for the reaction. This is one of the factors that lowers TE. Delaying GIT from 25° aTDC to 65° aTDC allows more air to enter the combustion zone, leading to higher combustion efficiency and increased TE. Yuvenda and colleagues [43] reported that delaying gas injection timing in dual-fuel mode increases volumetric efficiency due to more air intake into the cylinder, resulting in lower fuel consumption and higher TE achieved. Overall, when GIT changes from 25° to 65°, TE increases by an average of 2%, 3%, and 4% compared to diesel combustion for GIP 1.5 bar, GIP 2 bar, and GIP 2.5 bar operations, respectively. The TE output of the GIP 1 bar operation decreases by an average of 1% compared to diesel fuel.

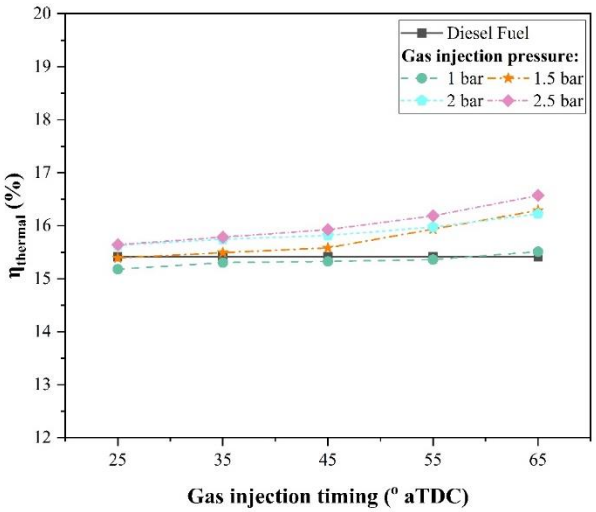

Fig. 5. The variation of thermal efficiency at different GIT versus GIP.

3.2. Impact of GIT and GIP on emissions

Fig. 6 shows the variation of HC emission corresponding to different GIT and GIP. Although the gradual increase of GIP from 1 bar to 2.5 bar significantly causes an increase in HC emissions, the gradual increase of GIT from 25° aTDC to 65° aTDC contributes to a decreasing trend in HC emissions. In experiments conducted under constant load and speed conditions, the lowest HC emissions are obtained with diesel fuel (25 ppm). Under GIP25 and GIP 1 bar conditions, HC emissions increase by 456% compared to diesel combustion, while this increase rate drops to 340% when the gas injection timing is delayed to 65° aTDC. Early injection of methane gas interrupts the mass flow rate of air taken into the cylinder and occupies some of the air volume inside the cylinder. This reduces the amount of air available for combustion and leads to the direct release of unburned CH4 gas. Overall, when GIT changes from 25° to 65°, HC emissions increase by an average of 414%, 455%, 522%, and 562% compared to diesel combustion for GIP 1 bar, GIP 1.5 bar, GIP 2 bar, and GIP 2.5 bar operations, respectively. Tripathi et al. [29] reported that as the amount of methane supplied to the cylinder increases, the oxygen concentration

decreases, thereby slowing down the combustion reaction and increasing HC emissions by up to 1000 times. However, in the current study, despite the increase in HC owing to increase in methane energy ratio, it is observed that the transition from 25º aTDC to 65º aTDC contributes to a decrease in HC emissions according to MIT.

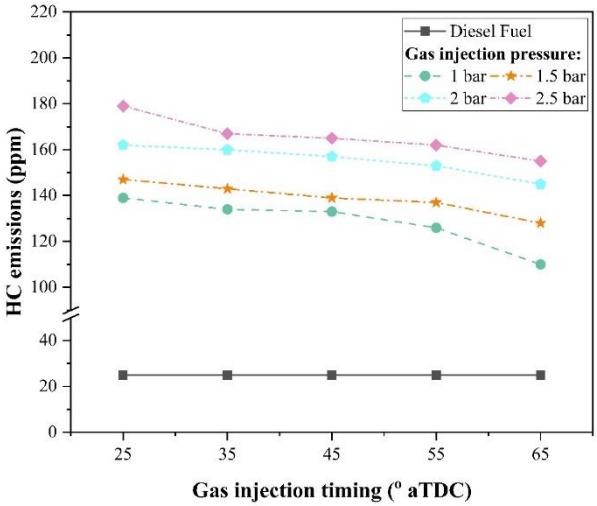

Fig. 6. The variation of HC emission at different GIT versus GIP.

Fig. 7 shows the variation of CO emission corresponding to different GIT and GIP. Similar to the results of HC emissions, CO emissions show an increasing trend with the rise in GIP. However, the rate of this increase slows down as GIT changes from 25º aTDC to 65º aTDC. The lowest CO emissions are obtained with diesel fuel (0.067%), while the highest CO emissions occur with early gas injection timing (GIT25) and high methane energy ratio (GIP 2.5 bar). The increase in methane energy ratio in dual-fuel mode raises the mass of methane entering the cylinder, causing the air inside the cylinder to cool down (due to methane's physicochemical properties). This chain reaction lowers combustion temperatures, stopping the oxidation of CO into CO_2, leading to higher CO emissions. Additionally, the increase in methane mass reduces the available O_2 in the combustion zone, which also contributes to the rise in CO emissions. Compared to diesel fuel, the highest increase in CO emissions is 137% under GIT 25 and GIP 2.5 bar conditions, while the lowest increase is 51% under GIT 65 and GIP 1 bar conditions. Overall, when GIT changes from 25º to 65º, CO emissions increase by an average of 64%, 78%, 94%, and 111% compared to diesel combustion for GIP 1 bar, GIP 1.5 bar, GIP 2 bar, and GIP 2.5 bar operations, respectively. Bora and colleagues [44] reported that methane gas reduces volumetric efficiency, leading to increased CO emissions in dual-fuel mode, which is consistent with the findings obtained in this article.

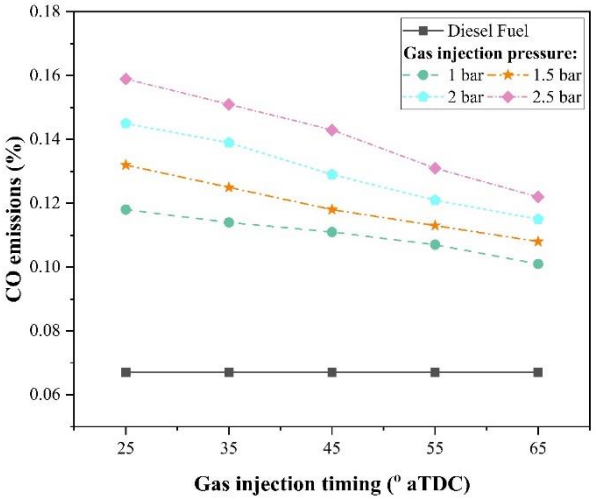

Fig. 7. The variation of CO emission at different GIT versus GIP.

Fig. 8 shows the variation of CO_2 emission corresponding to different GIT and GIP. The use of methane gas in diesel engines contributes to a reduction in CO_2 emissions. The lowest CO_2 emissions are obtained in the GIP 2.5 bar operation, while the highest CO_2 emissions are observed in diesel operation. For instance, at GIP 2.5 bar, where the lowest CO_2 emissions are recorded, the GIT 25 operation shows approximately a 13% reduction in CO_2 emissions compared to diesel operation, with an average reduction of 11.5% between GIT25 and GIT65 operation conditions. In the GIP 1 bar operation, which has a low methane energy ratio, GIT25 reduces CO_2 emissions by about 7% compared to diesel fuel, while the change in GIT from 25º aTDC to 65º aTDC results in a 3.5% reduction in CO_2 emissions compared to diesel combustion. As seen, an increase in the methane energy ratio contributes to a reduction in CO_2 emissions, while delaying methane injection timing tends to increase CO_2 emissions. Nevertheless, all CO_2 outputs obtained in the dual-fuel concept are lower than those produced by diesel combustion. The main reason for this is that with the increase in methane energy ratio, the carbon content of the mixture decreases. Additionally, the decrease

in combustion efficiency (as HC and CO emissions rise) also contributes to the reduction in CO_2 emissions. Another significant factor is that as CO emissions increase, CO_2 emissions decrease. Prabhu and colleagues [45] reported that an increase in the methane content in biogas reduces CO_2 emissions, and their findings are consistent with the results obtained in this article. Overall, when GIT changes from 25º to 65º, CO_2 emissions decrease by an average of 5%, 6%, 10%, and 11.5% compared to diesel combustion for GIP 1 bar, GIP 1.5 bar, GIP 2 bar, and GIP 2.5 bar operations, respectively.

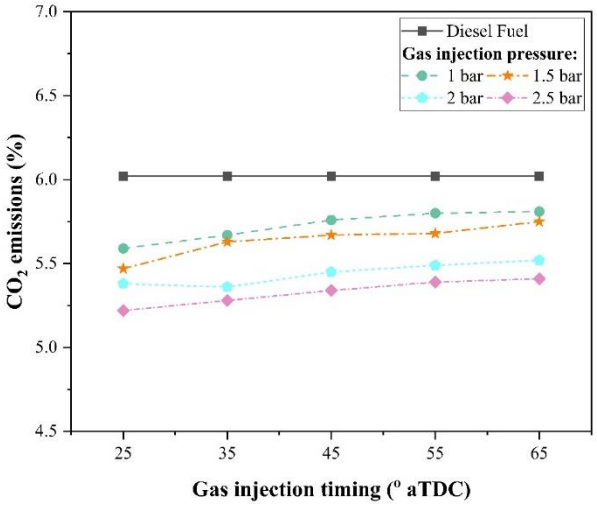

Fig. 8. The variation of CO_2 emission at different GIT versus GIP.

Fig. 9 shows the variation of NO emission corresponding to different GIT and GIP. One of the most significant problems in diesel engines is the formation of NO emissions due to the high compression ratio and high lambda value. However, the use of methane gas in diesel engines significantly contributes to the reduction of NO emissions. As seen in Fig. 9, NO emissions gradually decrease as GIP increases from 1 bar to 2.5 bar. The lowest NO emissions are obtained in the GIP 2.5 bar operation, while the highest NO emissions occur in diesel operation. For instance, in the GIP 1.5 bar operation, GIT 25 reduces NO emissions by 36% compared to diesel, while in the GIP 2.5 bar operation, GIT 25 reduces NO emissions by 47% compared to diesel. As GIT increases from 25º aTDC to 65º aTDC, NO emissions tend to increase, but they still remain lower than the NO emission outputs from diesel combustion. For example, in the GIP 1.5 bar operation, GIT 65 reduces NO emissions by 33% compared to diesel, while in the GIP 2.5 bar operation, GIT 25 reduces NO emissions by 44% compared to diesel. NO emissions are formed in conditions of high O_2 availability and high combustion temperatures. In the present study, the use of methane gas lowers the intake air temperature and also reduces the amount of air entering the cylinder. This significantly contributes to the reduction of NO emissions. Allouis and colleagues [46] reported that using methane in a diesel engine reduces the air-fuel ratio, thereby contributing to the reduction of NO_x emissions. In the current article, methane quantity increases with GIP change. Therefore, the decrease in NO emissions with an increase in GIP from 1 bar to 2.5 bar in this article is consistent. Overall, when GIT changes from 25º to 65º, NO emissions decrease by an average of 35%, 37%, 40%, and 46% compared to diesel combustion for GIP 1 bar, GIP 1.5 bar, GIP 2 bar, and GIP 2.5 bar operations, respectively.

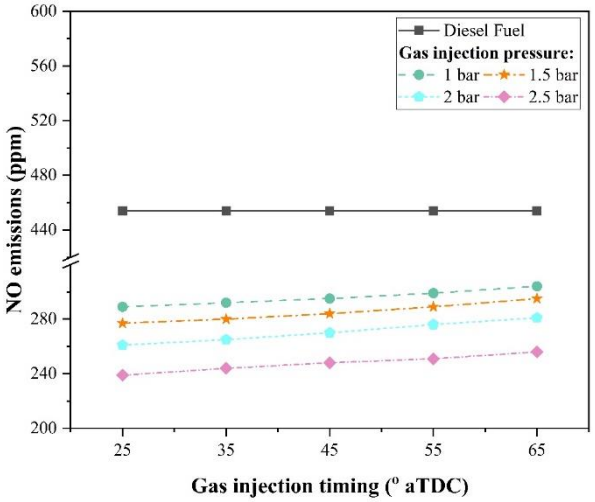

Fig. 9. The variation of NO emission at different GIT versus GIP.

Fig. 10 shows the variation of soot emission corresponding to different GIT and GIP. Soot formation from combustion is another major issue in diesel engines. In this study, the use of methane as a dual fuel significantly contributes to the reduction of soot emissions. For instance, in diesel operation, 1.21 1/m soot emissions are recorded, while in the dual-fuel mode, under GIP 2.5 bar conditions, GIT 65 reduces soot emissions by approximately 59.5% compared to diesel combustion. When GIT advances from 25º aTDC to 65º aTDC, the rate of reduction in soot emissions slows down. For example, under GIP 2.5 bar conditions,

GIT 25 reduces soot emissions by approximately 39% compared to diesel combustion. The highest soot emissions in dual-fuel operation are observed under GIP 1 bar conditions. The primary reason for the reduction in soot is that methane reduces diesel fuel energy (i.e., the amount of fuel injected into the combustion chamber). Additionally, methane's low C/H ratio is another important factor contributing to the reduction in soot formation. Overall, when GIT changes from 25° to 65°, soot emissions decrease by an average of 37%, 39%, 43%, and 48% compared to diesel combustion for GIP 1 bar, GIP 1.5 bar, GIP 2 bar, and GIP 2.5 bar operations, respectively. Liu and colleagues [47] reported that in CNG-diesel operation, increasing the amount of diesel fuel injected into the combustion chamber increases soot emissions, but the opposite occurs with an increase in CNG energy ratio. They also attribute this to the decrease in the amount of diesel fuel injected with an increase in CNG quantity. Consequently, in the current article, the increase in GIP from 1 bar to 2.5 bar results in an increase in the CH_4 energy ratio and a decrease in the amount of diesel fuel injected. This contributes to a decrease in soot emissions, aligning the results with the literature.

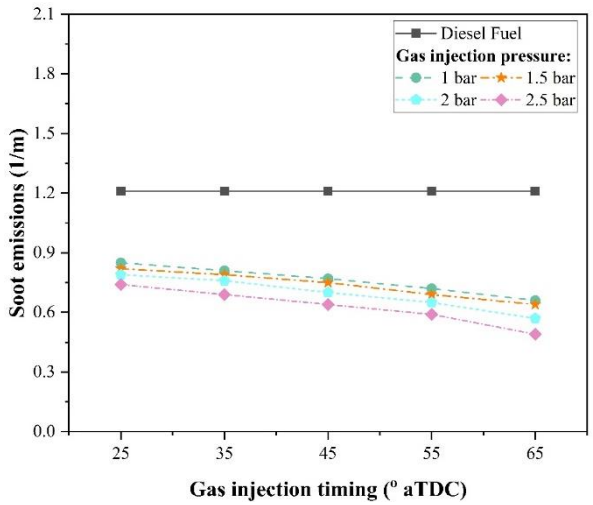

Fig. 10. The variation of soot emission at different GIT versus GIP.

3.3. Impact of GIT and GIP on environmental and economic of NO emissions

Fig. 11 shows the variation of environmental impact of NO (EN_{NOx}) corresponding to different GIT and GIP. When evaluating the EN_{NOx} outputs of both diesel and dual-fuel operations, the high NO emissions from diesel fuel result in higher EN_{NOx} compared to the dual-fuel application. The lowest EN_{NOx} is obtained with the GIP 2.5 bar operation. This is because the increase in GIP raises the GEP, which in turn reduces NO emissions. The EN_{NOx} value for diesel-only operation is recorded at 33.77 mPts/kWh. Under the GIP 2.5 bar conditions, where the lowest EN_{NOx} values are obtained, the EN_{NOx} values for GIT 25, GIT 35, GIT 45, GIT 55, and GIT 65 are 17.1 mPts/kWh, 17.5 mPts/kWh, 17.8 mPts/kWh, 17.9 mPts/kWh, and 18.4 mPts/kWh, respectively. In the dual-fuel concept, the highest EN_{NOx} values are obtained under GIP 1 bar conditions, where the EN_{NOx} values for GIT 25, GIT 35, GIT 45, GIT 55, and GIT 65 are 20.7 mPts/kWh, 20.9 mPts/kWh, 21.4 mPts/kWh, 21.4 mPts/kWh, and 21.8 mPts/kWh, respectively. Overall, when GIT changes from 25° to 65°, EN_{NOx} decreases by an average of 37%, 39.5%, 42.5%, and 47.5% compared to diesel combustion for GIP 1 bar, GIP 1.5 bar, GIP 2 bar, and GIP 2.5 bar operations, respectively.

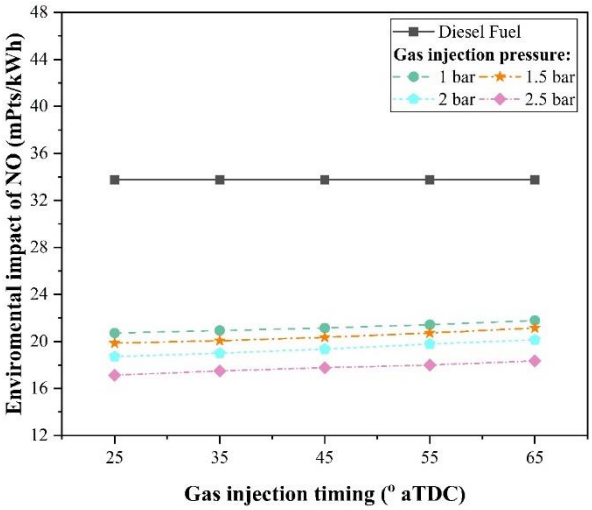

Fig. 11. The variation of environmental impact of NO at different GIT versus GIP.

Fig. 12 shows the variation of economic impact of NO (EC_{NOx}) corresponding to different GIT and GIP. As seen in the figure, the highest EC_{NOx} is obtained with diesel operation, while increasing GIP from 1 bar to 2.5 bar contributes to reducing the EC_{NOx}. The primary reason for the reduction in EC_{NOx} is the decrease in NO pollutants as the methane

gas energy ratio increases. The lowest EC_{NOx} values in the GIP 2.5 bar operation for GIT 25, GIT 35, GIT 45, GIT 55, and GIT 65 are 43.3 Euro/kWh, 44.2 Euro/kWh, 44.9 Euro/kWh, 45.5 Euro/kWh, and 46.4 Euro/kWh, respectively. As the results show, changing GIT from 25 aTDC to 65 aTDC causes a slight increase in EC_{NOx}. The main reason for this is that delaying GIT improves combustion stability and efficiency, which increases NO emissions and, consequently, the EC_{NOx}. In the dual-fuel concept, the highest EC_{NOx} values are obtained under GIP 1 bar conditions, where the EC_{NOx} values for GIT 25, GIT 35, GIT 45, GIT 55, and GIT 65 are 52.4 Euro/kWh, 52.9 Euro/kWh, 53.4 Euro/kWh, 54.2 Euro/kWh, and 55.1 Euro/kWh, respectively.

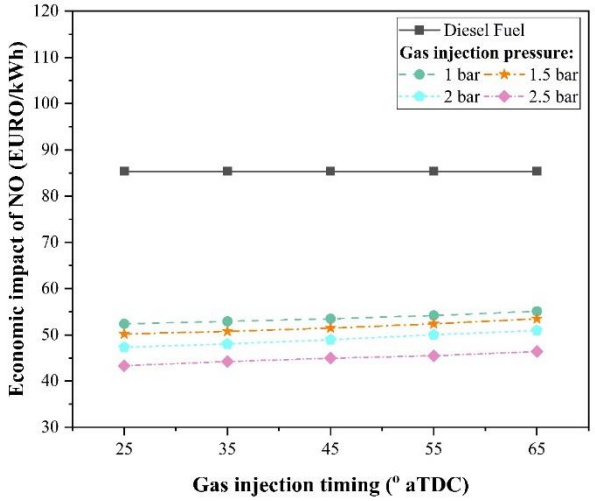

Fig. 12. The variation of economic impact of NO at different GIT versus GIP.

4. Conclusions

In this experimental study, the effects of GIT and GIP variations on performance and emissions are examined. Additionally, since one of the main problems of diesel engines is NO emissions, environmental impact and economic analysis are conducted using NO emission data from the experimental results. The outcomes obtained from both the experiments and the analysis are summarized below:

- The use of methane gas in diesel engines based on its energy fraction provides significant improvements in engine performance and exhaust emissions.
- An increase in GIP from 1 bar to 2.5 bar, along with a change in GIT from 25 aTDC to 65 aTDC, significantly contributes to the reduction of SFC. The lowest SFC is obtained under GIP 2.5 bar and GIT 65 conditions, with a maximum reduction of 12% compared to diesel. Under GIP 2.5 bar conditions, the average reduction in SFC between GIT 25 and GIT 65 is 8.5%.
- Increasing GIP and delaying GIT contribute to an increase in TE. The later injection of methane allows for more O_2 in the combustion zone and results in lower intake temperatures, leading to improved combustion efficiency and stability. Consequently, TE improves. The highest TE is obtained in the GIP 2.5 bar and GIT 65 setup, showing a 7.5% increase compared to diesel. Additionally, operating under the same GIT and GIP conditions shows an average increase of approximately 4% in TE compared to diesel operation.
- HC and CO emissions increase significantly with the rise of GIP from 1 bar to 2.5 bar. The replacement of some air by methane in the combustion zone contributes to the increase of both HC and CO. Additionally, due to the physicochemical properties of methane, its cooling effect on the intake air temperature causes the reactions of HC and CO to halt.
- However, delaying the GIT under all GIP conditions contributes to a reduction in HC and CO emissions. For example, the operation at GIP 1 bar and GIT 65 shows an approximately 21% reduction in HC emissions compared to GIT 25. Similarly, the operation at GIP 2.5 bar and GIT 65 demonstrates a 13% reduction in HC emissions compared to GIT 25.
- Also, the operation at GIP 1 bar and GIT 65 shows an approximately 14% reduction in CO emissions compared to GIT 25. Similarly, the operation at GIP 2.5 bar and GIT 65 demonstrates a 23% reduction in CO emissions compared to GIT 25.
- The methane-diesel dual-fuel combustion applied using the energy fraction reduces fuel consumption and decreases the C/H ratio as the methane content increases. This contributes to a reduction in CO_2 emissions, or in other words, the carbon footprint. For example, the lowest CO_2 emissions are achieved under GIP 2.5 bar conditions, with an average reduction rate of

11% compared to diesel operation.

- NO and soot emissions decrease significantly with the rise of GIP from 1 bar to 2.5 bar. NO emissions show a reduction of 47% at earlier GIT and higher GIP conditions. Delaying GIT allows more air to enter the combustion zone, resulting in a more homogeneous mixture. This improves combustion development, which in turn increases NO emissions.
- Soot emissions decrease by 59.5% under GIT 65 and GIP 2.5 bar conditions compared to diesel operation. The increase in the share of methane in the energy ratio leads to a reduction in the share of diesel, thereby decreasing the regions of rich mixtures. Additionally, as the gas energy fraction increases, the C/H ratio further decreases.
- The use of methane gas in an energy fraction in diesel engines significantly reduces the environmental and economic impact of NO. Under high GIP and early GIT conditions, both the environmental and economic effects decrease by approximately 48% compared to diesel.

In methane-diesel studies, while the increase in GIP leads to higher HC and CO pollutants, this issue can be mitigated by delaying GIT. Under high GIP conditions, sending heated gas fuel or heated intake air to the combustion chamber can overcome the problem of reduced intake air temperature due to the physicochemical properties of methane. Future studies could involve preheating the intake air or gas fuel before combustion. Additionally, the reduced air quantity in the combustion zone due to methane usage can lead to slower combustion reactions and a decrease in flame speed. This situation may cause the flame to extinguish before reaching the cylinder walls, resulting in the formation of high amounts of HC and CO. To address this issue, future studies could utilize nanoparticle additives that increase the surface-to-volume ratio and reaction rate within the diesel fuel.

Declaration of Competing Interest

The authors declare that they have no known competing financial interests or personal relationships that could have appeared to influence the work reported in this paper.

CRediT authorship contribution statement

Halil Erdi Gülcan: Conceptualization, Data curation, Formal analysis, Investigation, Methodology, Software, Validation, Visualization, Writing – original draft, Writing – review & editing.

Acknowledgement

I would like to thank Selçuk University and Karamanoğlu Mehmetbey University for their support in the experimental study.

5. References

1. Van Fan Y, Perry S, Klemeš JJ, Lee CT. A review on air emissions assessment: Transportation. Journal of cleaner production, 194:673-84, 2018.
Doi:
https://doi.org/10.1016/j.jclepro.2018.05.151
2. Chintala V, Subramanian K. A comprehensive review on utilization of hydrogen in a compression ignition engine under dual fuel mode. Renewable and Sustainable Energy Reviews, 70:472-91, 2017.
Doi: https://doi.org/10.1016/j.rser.2016.11.247
3. Altun Ş, Adin MŞ, Ilcin K. Monohydric aliphatic alcohols as liquid fuels for using in internal combustion engines: A review. Proceedings of the Institution of Mechanical Engineers, Part E: Journal of Process Mechanical Engineering, 238(4):1941-75, 2024.
Doi:
https://doi.org/10.1177/09544089231160472
4. Erol D, Yeşilyurt MK, Yaman H, Doğan B. Evaluation of the use of diesel-biodiesel-hexanol fuel blends in diesel engines with exergy analysis and sustainability index. Fuel, 337:126892, 2023.
Doi:
https://doi.org/10.1016/j.fuel.2022.126892
5. Deheri C, Acharya SK, Thatoi DN, Mohanty AP. A review on performance of biogas and hydrogen on diesel engine in dual fuel mode. Fuel, 260:116337, 2020.
Doi:
https://doi.org/10.1016/j.fuel.2019.116337
6. Gulcan HE, Ciniviz M. Experimental study on the effect of piston bowl geometry on the combustion performance and pollutant emissions of methane-diesel common rail dual-fuel engine. Fuel, 345:128175, 2023.
Doi:

https://doi.org/10.1016/j.fuel.2023.128175
7. Akcay M, Yilmaz IT, Feyzioglu A. The influence of hydrogen addition on the combustion characteristics of a common-rail CI engine fueled with waste cooking oil biodiesel/diesel blends. Fuel Processing Technology, 223:106999, 2021.
Doi:
https://doi.org/10.1016/j.fuproc.2021.106999
8. Gülcan HE, Ciniviz M. The effect of pure methane energy fraction on combustion performance, energy analysis and environmental-economic cost indicators in a single-cylinder common rail methane-diesel dual fuel engine. Applied Thermal Engineering, 230:120712, 2023.
Doi:
https://doi.org/10.1016/j.applthermaleng.2023.120712
9. Feroskhan M, Ismail S. Investigation of the effects of biogas composition on the performance of a biogas–diesel dual fuel CI engine. Biofuels, 7(6):593-601, 2016.
Doi:
https://doi.org/10.1080/17597269.2016.1168025
10. Demir U, Çelebi S, Özer S. Experimental investigation of the effect of fuel oil, graphene and HHO gas addition to diesel fuel on engine performance and exhaust emissions in a diesel engine. International Journal of Hydrogen Energy, 52:1434-46, 2024.
Doi:
https://doi.org/10.1016/j.ijhydene.2023.08.007
11. Zhang Z, Wang S, Pan M, Lv J, Lu K, Ye Y, et al. Utilization of hydrogen-diesel blends for the improvements of a dual-fuel engine based on the improved Taguchi methodology. Energy, 292:130474, 2024.
Doi:
https://doi.org/10.1016/j.energy.2024.130474
12. Lawrence KR, Anchupogu P, Reddygari MR, Gangula VR, Balasubramanian D, Veerasamy S. Optimization of biodiesel yield and performance investigations on diesel engine powered with hydrogen and acetylene gas injected with enriched Jojoba biodiesel blend. International Journal of Hydrogen Energy, 50:502-23, 2024.
Doi:
https://doi.org/10.1016/j.ijhydene.2023.09.166
13. Solmaz H, Calam A, Yılmaz E, Şahin F, Ardebili SMS, Aksoy F. Evaluation of MWCNT as fuel additive to diesel–biodiesel blend in a direct injection diesel engine. Biofuels, 14(2):147-56, 2023.
Doi:
https://doi.org/10.1080/17597269.2022.2122154
14. Uyaroğlu A, Uyumaz A, Çelikten İ. Comparison of the combustion, performance, and emission characteristics of inedible Crambe abyssinica biodiesel and edible hazelnut, corn, soybean, sunflower, and canola biodiesels. Environmental Progress & Sustainable Energy, 37(4):1438-47, 2018.
Doi: https://doi.org/10.1002/ep.12794
15. Erol D, Yaman H, Doğan B, Yeşilyurt MK. The assessment of fusel oil in a compression-ignition engine in the perspective of the waste to energy concept: investigation of the performance, emissions, and combustion characteristics. Biofuels;13(10):1147-64, 2022.
Doi:
https://doi.org/10.1080/17597269.2022.2111779
16. Gürbüz H, Demirtürk S. Investigation of dual-fuel combustion by different port injection fuels (Neat Ethanol and E85) in a DE95 diesel/ethanol blend fueled compression ignition engine. Journal of Energy Resources Technology;142(12):122306, 2020.
Doi: https://doi.org/10.1115/1.4047328
17. Doğan B, Erol D, Yaman H, Kodanli E. The effect of ethanol-gasoline blends on performance and exhaust emissions of a spark ignition engine through exergy analysis. Applied Thermal Engineering, 120:433-43, 2017.
Doi:
https://doi.org/10.1016/j.applthermaleng.2017.04.012
18. Adin MŞ, Altun Ş, Adin MŞ. Effect of using bioethanol as fuel on start-up and warm-up exhaust emissions from a diesel power generator. International Journal of Ambient Energy;43(1):5711-7, 2022.
Doi:
https://doi.org/10.1080/01430750.2021.19773

87
19. Uyar M, Aydın H. Production of low sulfur diesel-like fuel from crude oil wastes by pyrolytic distillation and its usage in a diesel engine. Energy, 244:122683, 2022.
Doi: https://doi.org/10.1016/j.energy.2021.12268
20. Rosha P, Dhir A, Mohapatra SK. Influence of gaseous fuel induction on the various engine characteristics of a dual fuel compression ignition engine: a review. Renewable and Sustainable Energy Reviews, 82:3333-49, 2018.
Doi: https://doi.org/10.1016/j.rser.2017.10.055
21. Wei L, Geng P. A review on natural gas/diesel dual fuel combustion, emissions and performance. Fuel Processing Technology, 142:264-78, 2016.
Doi: https://doi.org/10.1016/j.fuproc.2015.09.018
22. Park H, Shim E, Bae C. Improvement of combustion and emissions with exhaust gas recirculation in a natural gas-diesel dual-fuel premixed charge compression ignition engine at low load operations. Fuel, 235:763-74, 2019.
Doi: https://doi.org/10.1016/j.fuel.2018.08.045
23. Hernández JJ, Lapuerta M, Barba J. Separate effect of H2, CH4 and CO on diesel engine performance and emissions under partial diesel fuel replacement. Fuel, 165:173-84, 2016.
Doi: https://doi.org/10.1016/j.fuel.2015.10.054
24. Krishnan S, Biruduganti M, Mo Y, Bell S, Midkiff K. Performance and heat release analysis of a pilot-ignited natural gas engine. International Journal of Engine Research, 3(3):171-84, 2002.
Doi: https://doi.org/10.1243/14680870260189280
25. Papagiannakis R, Hountalas D. Experimental investigation concerning the effect of natural gas percentage on performance and emissions of a DI dual fuel diesel engine. Applied Thermal Engineering, 23(3):353-65, 2003.
Doi: https://doi.org/10.1016/S1359-4311(02)00187-4
26. Di Blasio G, Belgiorno G, Beatrice C. Effects on performances, emissions and particle size distributions of a dual fuel (methane-diesel) light-duty engine varying the compression ratio. Applied energy, 204:726-40, 2017.
Doi: https://doi.org/10.1016/j.apenergy.2017.07.103
27. Chen Z, Wang L, Wang X, Chen H, Geng L, Gao N. Experimental study on the effect of water port injection on the combustion and emission characteristics of diesel/methane dual-fuel engines. Fuel, 312:122950, 2022.
Doi: https://doi.org/10.1016/j.fuel.2021.122950
28. Ouchikh S, Lounici M, Loubar K, Tarabet L, Tazerout M. Effect of diesel injection strategy on performance and emissions of CH4/diesel dual-fuel engine. Fuel, 308:121911, 2022.
Doi: https://doi.org/10.1016/j.fuel.2021.121911
29. Tripathi G, Nag S, Sharma P, Dhar A. Effect of methane supplementation on the performance, vibration and emissions characteristics of methane-diesel dual fuel engine. Frontiers in Thermal Engineering, 3:1101333, 2023.
Doi: https://doi.org/10.3389/fther.2023.1101333
30. Ahmad Z, Kaario O, Karimkashi S, Qiang C, Vuorinen V, Larmi M. Effects of ethane addition on diesel-methane dual-fuel combustion in a heavy-duty engine. Fuel, 289:119834, 2021.
Doi: https://doi.org/10.1016/j.fuel.2020.119834
31. Liu J, Guo Q, Guo J, Wang F. Optimization of a diesel/natural gas dual fuel engine under different diesel substitution ratios. Fuel, 305:121522, 2021.
Doi: https://doi.org/10.1016/j.fuel.2021.121522
32. Di Iorio S, Magno A, Mancaruso E, Vaglieco BM. Diesel/methane dual fuel strategy to improve environmental performance of energy power systems. International Journal of Heat and Technology, 34(2):581-8, 2016.
Doi: https://doi.org/10.18280/ijht.34S254
33. Khedkar ND, Sarangi AK, Sreedhara S. Impact of engine control variables on low load

combustion efficiency and exhaust emissions of a methane-diesel dual fuel engine. Proceedings of the Institution of Mechanical Engineers, Part D: Journal of Automobile Engineering, 09544070231197613, 2023.
Doi: https://doi.org/10.1177/09544070231197613
34. Zarrinkolah MT, Hosseini V. Methane slip reduction of conventional dual-fuel natural gas diesel engine using direct fuel injection management and alternative combustion modes. Fuel, 331:125775, 2023.
Doi: https://doi.org/10.1016/j.fuel.2022.125775
35. Cameretti MC, De Robbio R, Palomba M. Numerical Analysis of Dual Fuel Combustion in a Medium Speed Marine Engine Supplied with Methane/Hydrogen Blends. Energies, 16(18):6651, 2023.
Doi: https://doi.org/10.3390/en16186651
36. Yin C, Wang C, Shen X, Zhang Z. Experimental and simulation study of diesel/methane/hydrogen triple-fuel combustion progression in a heavy-duty optical engine. International Journal of Hydrogen Energy, 62:562-78, 2024.
Doi: https://doi.org/10.1016/j.ijhydene.2023.10.198
37. Zhang X, Gao J, Fan D, Yang Q, Han F, Yu H. Impact of pilot diesel injection timing on performance and emission characteristics of marine natural gas/diesel dual-fuel engine. Scientific Reports, 14(1):10713, 2024.
Doi: https://doi.org/10.1038/s41598-024-61672-5
38. Gülcan HE, Gültekin N, Ciniviz M. Experimental investigation of the effect of variable valve lift on combustion stability and exhaust emissions in a diesel/methane CRDI engine. Energy, 300:131603, 2024.
Doi: https://doi.org/10.1016/j.energy.2024.131603
39. Zheng J, Wang J, Zhao Z, Wang D, Huang Z. Effect of equivalence ratio on combustion and emissions of a dual-fuel natural gas engine ignited with diesel. Applied Thermal Engineering, 146:738-51, 2019.
Doi: https://doi.org/10.1016/j.applthermaleng.2018.10.045
40. Gürbüz H, Akçay İH. Evaluating the effects of boosting intake-air pressure on the performance and environmental-economic indicators in a hydrogen-fueled SI engine. International Journal of Hydrogen Energy, 46(56):28801-10, 2021.
Doi: https://doi.org/10.1016/j.ijhydene.2021.06.099
41. Gürbüz H, Akçay H, Aldemir M, Akçay İH, Topalcı Ü. The effect of euro diesel-hydrogen dual fuel combustion on performance and environmental-economic indicators in a small UAV turbojet engine. Fuel, 306:121735, 2021.
Doi: https://doi.org/10.1016/j.fuel.2021.121735
42. Gülcan HE. Effect of methane injection strategy on combustion, exergetic performance, and enviro-economic analyses in a diesel/methane CRDI engine. Applied Thermal Engineering, 243:122654, 2024.
Doi: https://doi.org/10.1016/j.applthermaleng.2024.122654
43. Yuvenda D, Sudarmanta B, Wahjudi A, Muraza O. Improved combustion performances and lowered emissions of CNG-diesel dual fuel engine under low load by optimizing CNG injection parameters. Fuel, 269:117202, 2020.
Doi: https://doi.org/10.1016/j.fuel.2020.117202
44. Bora BJ, Saha UK, Chatterjee S, Veer V. Effect of compression ratio on performance, combustion and emission characteristics of a dual fuel diesel engine run on raw biogas. Energy conversion and management, 87:1000-9, 2014.
Doi: https://doi.org/10.1016/j.enconman.2014.07.080
45. Vijin Prabhu A, Manimaran R, Jeba P, Babu R. Effect of methane enrichment on the performance of a dual fuel CI engine. International Journal of Ambient Energy, 42(3):325-30, 2021.
Doi: https://doi.org/10.1080/01430750.2018.1550017
46. Allouis C, De Robbio R, Mancaruso E, Vaglieco B. Effect of hydrogen and methane in dual fuel mode in light diesel engine by VIS

and IR imaging. International Journal of Hydrogen Energy, 52:1491-501, 2024. Doi: https://doi.org/10.1016/j.ijhydene.2023.08.163

47. Liu J, Yang F, Wang H, Ouyang M, Hao S. Effects of pilot fuel quantity on the emissions characteristics of a CNG/diesel dual fuel engine with optimized pilot injection timing. Applied Energy, 110:201-6, 2013. Doi: https://doi.org/10.1016/j.apenergy.2013.03.024

e-ISSN: 2146 - 9067

International Journal of Automotive Engineering and Technologies

journal homepage:
https://dergipark.org.tr/en/pub/ijaet

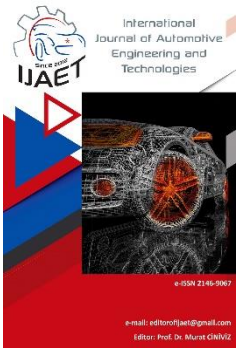

Original Research Article

The hydrogen injection strategy's influence on the performance and emissions (exhaust, vibration, and noise) of a dual-fuel engine

Nurullah Gültekin [1*]

[1,*] Mechanical Engineering Department, Tokat Gaziosmanpaşa University, 60250, Tokat, Türkiye.

ARTICLE INFO

Orcid Numbers

1. 0000-0002-0139-1352

Doi: 10.18245/ijaet.1553377

* Corresponding author
nurullah.gultekin@gop.edu.tr

Received: Sep 20, 2024
Accepted: Nov 24, 2024

Published: 31 Dec 2024

Published by Editorial Board Members of IJAET

ABSTRACT

The new trend in the search for alternative fuels for compression ignition engines is the hydrogen-diesel dual fuel (HDDF) mode. In order for dual fuel mode to provide maximum benefit in compression ignition engines, ECU-controlled fuel systems should be used, and their settings should be optimized. In this study, the effects of hydrogen energy ratio and hydrogen injection timing on engine performance, exhaust, noise, and mechanical vibration emissions in an ECU-controlled HDDF system compression ignition engine were investigated. The experiments were carried out at constant speed (1850 rpm), constant load (5 Nm), different hydrogen ratios (11, 14, 17, 20%), and different hydrogen injection timings (20, 30, 40, 50, and 60 °CA aTDC). The specific energy consumption decreased by 8.4%, NOx emissions decreased by 68.4%, and mechanical vibrations increased by 16.6% at a 14% hydrogen energy ratio and a 30°CA aTDC hydrogen injection timing. The main objective of the study is to determine the optimum hydrogen energy ratio and hydrogen injection timing in a compression ignition engine using HDDF.

Keywords: H_2-diesel dual fuel engine; H_2 ration; H_2 injection timing; Engine performance; Emission (exhaust, noise, and mechanical vibration)

1. Introduction

The transportation sector around the world is growing rapidly. This growth increases the demand for fuel and leads to rising fuel prices. Additionally, the emission standards implemented by countries have raised questions about the future of internal combustion (IC) engines. Consequently, several nations have implemented prohibitions on the commercialization of automobiles equipped with compression ignition (CI) engines that rely on diesel fuel. Manufacturers and researchers have turned to alternative energy sources to overcome these problems [1, 2]. Electric vehicles are at the forefront of vehicles using alternative energy. However, it will take some time for these vehicles to become widespread due to charging time, battery life, and infrastructure problems [3]. Because of these things, it is a given that IC motors, which have been used by people for the past 150 years, will continue to be the most common type for a long time [4-6]. Therefore, studies to develop IC motors continue at a great pace [7-9].

CI engines used in most of today's vehicles

have many advantages over their equivalent spark ignition engines [10]. Almost all of the engines used, especially in freight road vehicles, railway vehicles, and ships, are CI engines. The primary reason for this is because these motors have excellent torque and thermal efficiency [11, 12]. However, the pressure on these engines due to emissions has increased in recent years. As a result of printing, some automobile companies stopped the production of vehicles using CI engines [13]. To solve this problem, it is possible to use different fuel mixtures in diesel engines. Biodiesel in particular has been around for a long time. At the same time, the use of bio-based alcohols is an ideal way to reduce emissions [12]. In recent years, along with the use of biofuel-diesel, studies on the combined use of liquid and gaseous fuels have accelerated [14]. Hydrogen fuel is an ideal fuel for this. The use of H_2 with diesel fuel will contribute to these engines meeting emission standards. Studies on the dual fuel mode for H_2-diesel indicate that due to H_2's lack of carbon atoms, it can reduce carbon dioxide, carbon monoxide, particulate matter, and hydrocarbon (CO_2, CO, PM, and HC) emissions [15-17]. At the same time, it is also possible to improve engine efficiency [18, 19]. Furthermore, it is anticipated that H_2 may be derived from sustainable energy sources such as wind, wave, solar, and biomass, hence diminishing reliance on conventional oil-based fuels [20-22]. Akçay et al. [23] conducted experiments on a common rail diesel injection (CRDI) engine. Researchers discovered a correlation between the increase in H_2 rate and engine load and the decrease in CO_2 emissions. Many studies have found that this is due to the fact that the fuel used in the burning chamber has less carbon in it. [24-26]. Koten [27], looked at the emissions in dual-fuel mode and how adding H_2 at different loads affected the emissions. According to the study's results, CO, HC, and PM pollution all went down by a lot, no matter how much the load there was.

Many researchers have examined how HDDF mode affects exhaust pollutants. However, today, studies on mechanical vibration and noise emissions, which have proven to have many negative effects on humans, nature, and engines, are limited [28, 29]. Nag, Dhar [30] discovered that adding H_2 to the HDDF mode decreased mechanical vibration and noise at low loads while increasing it at high loads. In a similar study, Nag, Sharma [31] conducted tests with H_2 energy ratios (HER) of 5%, 10%, and 20% utilizing the dual fuel method. They witnessed an increase in the HER at low loads reduced mechanical vibration and noise emissions, while it increased them at high loads. Barelli, Bidini [32], who examined the relationship of in-cylinder pressure with mechanical vibration and noise, determined that these emissions were related to in-cylinder pressure.

In the HDDF mode, the fuel energy ratio is critical. This is mostly due to the fact that the energy ratio is the critical factor impacting emissions and engine performance. The small molecular structure of H_2 causes its volume per unit mass to be higher [33, 34]. Because of this circumstance, the H_2 that is supplied to the cylinder takes up more space and blocks the entry of air. Akçay at al. [18] investigated the biodiesel-H_2 mixture in a CRDI engine. The study discovered that increasing the H_2 ratio increased the maximum cylinder pressure. However, in this study, the H_2 ratio was limited to a certain level. In another similar study, Yılmaz and Gümüş [35] looked at how adding H_2 to the intake air affected CI engine combustion performance. According to the study, the in-cylinder pressure increased as the volume of H_2 in the cylinder increased. In a similar study, Sharma and Dhar [36] altered the HER in dual fuel mode to 5, 10, and 20% and fed it into the intake manifold. At all engine conditions, the addition of H_2 was found to reduce the thermal efficiency (BTE) and increase the in-cylinder pressure. Whereas in another research variable H_2 ratios were studied experimentally; Qin et al. [37] found that raising the amount of H_2 energy to 20% raised the highest pressure in the cylinder by about 8%. The study also discovered that the rate of heat (HRR) increases and appears at earlier points. In another study where different HER were tested, Koten [27] revealed that augmenting the levels of H_2 and engine load led to a notable enhancement in thermal efficiency, while simultaneously causing a reduction in specific fuel consumption. The fact that the HER can't be raised to high levels

is the most important problem with the dual fuel system. This causes a reduction in volumetric efficacy and a deterioration of combustion. In their research, Morais et al. and Geo et al. [25, 38], found that increasing the HER and engine load had a detrimental effect on volumetric efficiency. The H_2 that is packed in the cylinder stops air from being drawn into it, which is why volumetric efficiency has decreased, according to researchers [39].

As significant as the impact of fuel energy ratios on engine output and emissions is how the H_2 is supplied to the cylinder in the HDDF mode. Especially with the high diffusion rate of H_2, the injection timing time is important. In engines with port injection, the timing of H_2 injection should be adjusted, taking into consideration the timings at which the intake valves and the exhaust valves open. Otherwise, the H_2 will ignite with the exhaust gases and cause blowback. Studies on the H_2 injection strategy are limited. Focusing on this issue, Saravanan, Nagarajan [40], investigated the injection approach utilized by a single-cylinder CI engine when operating in HDDF mode. In addition, diethyl ether was utilized in this investigation as a source of ignition. The researchers determined the optimum timing for H_2 injection to be 5° CA bTDC of the gas exchange and 40° CA aTDC for diethyl ether injection. The same researchers, in another study, in their experimental study to optimize H_2 injection in HDDF mode, stated that the optimum timing of port injection is 30° CA aTDC and the injection should be during gas exchange [41].

When research is assessed in aggregate, it is shown that the HER in HDDF mode as well as the injection methods of H_2 fuel have an influence on the overall performance of the engine as well as the pollutants it produces [31, 42, 43]. As a result, the ratio of hydrogen to diesel fuel and the time of hydrogen injection were the primary focuses of this research. Another important point study's conclusion is that the H_2 and diesel fuel systems are ECU-controlled and programmable. In this respect, it has a different importance from other studies.

In the course of this investigation, using a CI engine with a single cylinder, constant speed (1850 rpm), constant load (5 Nm), different H_2 injection ration (11, 14, 17, 20%), and different H_2 injection timing (20, 30, 40, 50, and 60 °CA aTDC) were performed. Engine performance, exhaust, mechanical vibration, and noise emissions were investigated as a consequence of the studies, and the optimal HER and optimum H_2 injection timing was identified. The primary objective of the research is to develop a suitable replacement for CI engines, which are banned in many countries and whose production has been stopped by companies. With just a few tweaks (H_2 fuel system), these motors can run on both diesel and hydrogen. Thus, performance and emissions can be improved, and usage can be continued.

2. Instrumentation and Methodology

The system set up to the schematic view of the experimental engine test setup is shown in Fig. 1. In the system, there is an ANTOR AD320 model single-cylinder CI engine with an ECU-controlled dual fuel system. To load the engine, an ABB brand active dynamometer is used, and an AVL brand pressure measurement system is employed to measure in-cylinder pressure. For measuring emission values, Bosch BEA 60-70 emission devices are used. To measure mechanical vibrations, a PCE-VD 3 brand vibration device is utilized, and for noise measurements, a Geratech DT 8820 model noise measuring device is used. Additionally, there is a fuel measuring system available for precise fuel measurements. MOTEC ECUs are used in the control of diesel fuel systems, whilst Spark EMS ECU are put to use in the management of hydrogen fuel systems. Thanks to the interface of this system on the computer, the open time of the hydrogen injector and the injection timing can be changed. In this way, different amounts of hydrogen can be sent to the cylinder at any time.

Diesel fuel has been used with the CRDI fuel system. Thanks to the ECU and the interface loaded onto the computer in the system, various parameters such as fuel pressure, fuel timing, and pre-injection can be adjusted instantly. The H_2 injector is placed behind the intake port, enabling the implementation of a port injection system. In addition, the hydrogen consumption data was recorded using a flowmeter from Sierra Instruments that

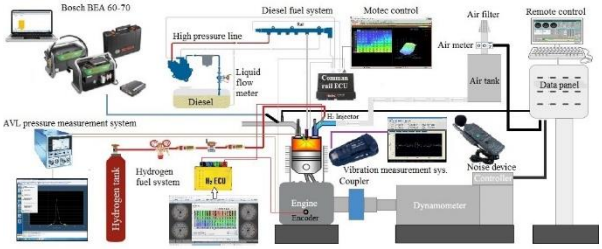

Fig. 1. Schematic view of experimental engine test setup.

was installed in the hydrogen fuel system. In the experiments, changes in cylinder pressure were measured to assess the combustion in the cylinder. In order to get the necessary data, a pressure sensor is used alongside an amplifier that effectively filters the voltage produced by the sensor, converting it into a discernible pressure signal. Additionally, an encoder is utilized to detect fluctuations in cylinder pressure resulting from changes in crank angle. Throughout the experimental procedure, data points were meticulously documented for every 0.1 °CA increment of the crankshaft's rotational position. The average of 180 cycles was utilized to generate in-cylinder pressure readings.

2.1. Test fuels and methodology

In Table 1 we can see the chemical and physical characteristics of the H_2 and diesel fuel that was used in the tests. Diesel fuel meets the requirements of TS EN 590:2013+A1:2017. At 200 bar pressure, H_2 fuel was kept in high purity tubes (99.9995%).

Table 1 - Diesel and H_2 fuel physical and chemical properties [44].

Property	Unit	H_2	Diesel
Formula		H_2	$C_nH_{1,8n}$ $C_8 - C_{20}$
Ignition temperature	K	858	530
Minimum Ignition Energy	MJ	0.02	–
Ignition limits (% by volume)		4 – 75	0.7 – 5
Stoichiometric H/Y ratio (Mass)		34.3	14.5
Ignition limits (equity ratio)		0.1 – 71	
Net Calorific Value	MJ/kg	119.93	42.5
Density (at 15°C and 1.01 bar)	kg/m³	0.0838	832
Flame speed	cm/s	269 – 325	30
Diffusion in Air	cm²/s	0.63	–
Octane Number		130	30
Cetane Number		–	53.9

First, experiments with standard diesel were conducted in the study, and data were collected. The HER is calculated using the fuel consumption data from these tests. The H_2 electronic control unit (ECU) was used to adjust the injection duration and timing, while a flow meter measured the amount of H_2 utilized. The observed values and equations (1)-(3) were utilized in the computation of HERs [26, 35].

$$ES_H = E_H/(E_H + E_D) \quad (1)$$

$$E_H = LHV_H.\dot{m}_H \quad (2)$$

$$E_D = LHV_D.\dot{m}_D \quad (3)$$

In the formulae, LHV_H represents H_2's lower calorific value, and LHV_D represents diesel fuel's lower calorific value (MJ/kg). $\dot{m}_H$ and $\dot{m}_D$ signify H_2 and diesel mass fluxes (kg/h). The total energy acquired from H_2 (E_H) and diesel (E_D) the initial measurement was adjusted to match the energy content of normal diesel fuel. The observed values and equations (1)-(3) were utilized in the computation of HERs formed by calculations are 11%, 14%, 17% and 20%.

Eq. (4) was used to calculate the motor's thermal efficiency. BP denotes braking power (kW) in the equation.

$$BTE = BP/(E_H + E_D) \quad (4)$$

2.2. Experimental procedure

Following the necessary changes and calibrations, the test engine was then linked to the engine test center, as seen in Fig. 2. Before commencing the trials, preparatory tests were undertaken to ensure that the engine was brought to suitable operating conditions. The trials were performed three times to limit the margin of error in the data, and the averages of the values were recorded. Table 2 exhibits the technical specifications of the modified engine and the test parameters.

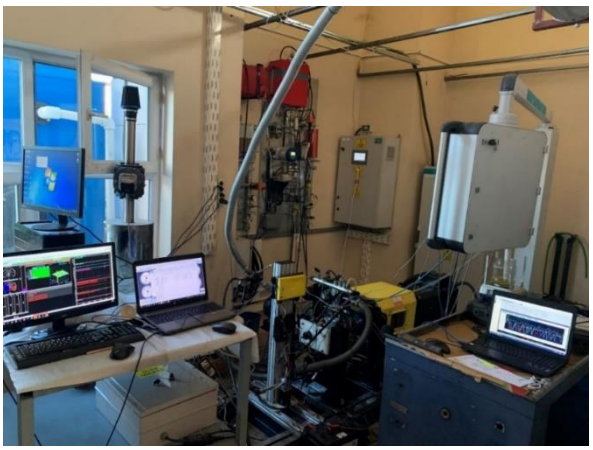

Fig. 2. The manner in which all systems attach to the engine test system.

Table 2- Characteristics of the engine and test

parameters.

Brand/Model	ANTOR / AD 320
Number of cylinders	1
Cylinder volume / Compression ratio	315 cm³ / 17.3/1
Max. torque	11 @1850 rpm
Engine speed	1850 rpm [constant]
Engine load	5 [Nm]
Fuel supply system	Dual-fuel
Diesel fuel system	Common rail
Diesel fuel system ECU	MoTeC M142
Diesel fuel system ECU software	GPR-DI
Diesel Injection timing	12 [°CA bTDC]
Diesel Injection pressure	400 [Bar]
H_2 fuel system	Port injection
H_2 fuel system ECU / software	Speeduino / TunerStudio MS
H_2 Injection timing	20, 30, 40, 50, 60 [°CA aTDC]
H_2 Injection pressure	1.5 [Bar]
H_2 injection duration / H_2 energy ratio	1.4, 1.6, 1.8, 2.0 [ms] / 11, 14, 17, 20 [%]
Ambient pressure / Ambient temperature	0.893 [bar] / 23.5 [°C]
Combustion chamber type	Standard

While selecting the test parameters, the operating conditions of the engine in the market, the results obtained from the preliminary tests, and the literature analysis were taken into consideration. 1850 rpm is the speed at which the maximum torque of the engine occurs. 5N load is the half-load condition where the engine is operated for a long time in operating conditions. The hydrogen energy ratio was determined as a result of the literature study. The hydrogen injection timing was determined according to the valve adjustment diagram of the engine.

3. Results and discussions

3.1. Volumetric efficiency

The decrease in volumetric efficiency in H_2-diesel dual-fuel engines is an important problem. Increasing the H_2 ratio reduces volumetric efficiency and has a negative impact on engine performance. The main reason for this problem is that H_2 occupies too much room in the cylinder [45-48]. The impact of the observed values and equations (1)-(3) were utilized in the computation of HER and timing of the H_2 injection on volumetric efficiency is shown in Fig. 3.

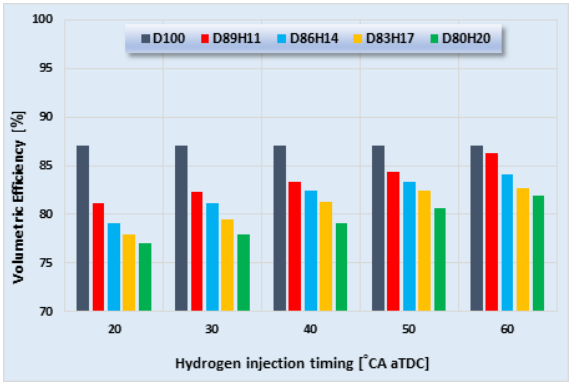

Fig. 3. Volumetric efficiency resulting from H_2 energy rate and injection timing.

A drop in volumetric efficiency was the result, as can be shown in Fig. 3, of a rise in the HER. The drop in volumetric efficiency, on the other hand, was mitigated by postponing the beginning of the H_2 injection. The main reason for this situation is that H_2 injection occurs close to the closing of the intake valve. Delaying the hydrogen injection ensures that there is enough time for most of the air to be taken into the cylinder [6, 49, 50].

3.2. Break thermal efficiency (BTE)

The thermal efficiency of a system is a significant measure of how effectively fuel is utilized, therefore it is desirable to have greater thermal efficiency. Fig. 4 shows how HER and injection timing affect thermal efficiency.

As can be clearly seen in Fig 4, a rise in the energy of H_2 ratio up to 14% caused an increase in BTE. In 17% and 20%, the rate of increase in BTE decreased. However, in experiments where the H_2 injection initiation was at 30 °CA aTDC, it was determined that the maximum rate of increase in BTE was achieved. At the same time, increasing the hydrogen energy rate prevents air from entering the cylinder by occupying too much space in the cylinder. This worsens combustion and causes the BTE to decrease.

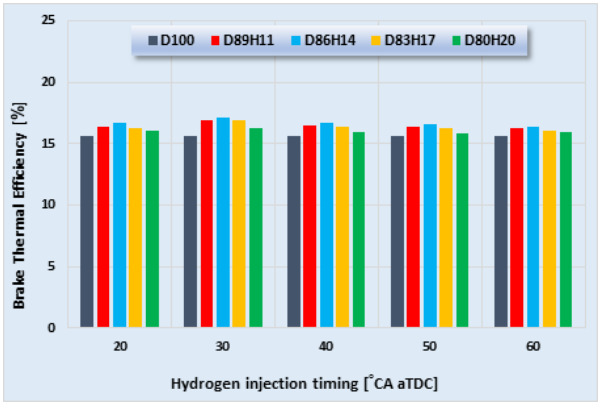

Fig. 4. BTE resulting from H_2 energy rate and injection timing.

3.3. Brake specific energy consumption (BSEC)

BSEC refers to the quantity of energy consumed per unit of output by an internal combustion engine. The aforementioned data source holds significant importance in the realm of fuel efficiency [51]. Fig. 5 shows the HER and the effect of H_2 injection initiation on BSEC.

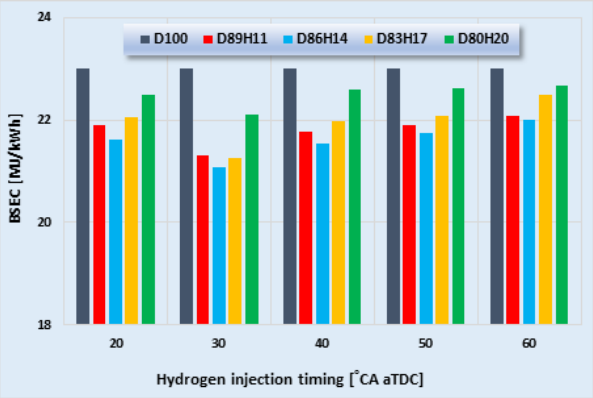

Fig. 5. BSEC resulting from H_2 energy rate and injection timing.

When Fig. 5 is evaluated, an increase in HER up to 14% has led to a decrease in BSEC. At 17% and 20% HER, the effect of H_2 on BSEC decreased. Additionally, in experiments where the H_2 injection initiation was at 30 °CA aTDC, it was determined that the BSEC decreased at the maximum rate. Elevating the HER to elevated levels has a detrimental impact on the BSEC. Volumetric efficiency is declining, and combustion is getting poorer, which is the major cause of this problem [25, 38, 52-54].

3.4. Peak cylinder pressure and heat release rate (HRR)

Fig. 6 shows how the amount of H_2 energy and the timing of H_2 injection affect the pressure inside the cylinder and the rate at which heat is released.

The rise in HER to as high as 14% has resulted in an increase in both the maximum pressure and the HRR of the cylinder. The maximum pressure within the cylinder rose by 9% in the experiment when the HER was 14% and the H_2 injection timing was 30 °CA aTDC. However, raising the H_2 ratio over 17% resulted in a slower rise in HRR and cylinder pressure. These results can be attributed to the insufficient air supply caused by injecting more H_2 into the cylinder. Inadequate air causes a drop in in-cylinder pressure and HRR. These findings are congruent with those of previous research published in the literature [4, 38, 45, 48, 55]. By advancing the timing of the H_2 injection, the maximum cylinder pressure as well as the maximum HRR were moved closer to the top dead center position. As a result, the maximum pressure created increased as well. The primary cause of this condition is that H_2 injection is made during air intake and a more homogeneous mixture is provided.

3.5. Exhaust emissions

Reducing the carbon atom in the fuel is an ideal method to decrease carbon-based emissions. However, increasing the H_2 concentration to high levels reduces the amount of oxygen entering the cylinder and worsens combustion. Fig. 7 demonstrates the impact of HER and H_2 injection timing on CO emissions.

The increase in the HER has reduced CO emissions. Adjusting the start of H_2 injection to 30 °CA aTDC and the HER to 17% resulted in a 53% reduction in CO emissions. The reduction in the fuel's carbon content is the primary cause of the drop in CO emissions.

By joining the combustion process, the HC emissions that come out of the exhaust without being burned tell us about the quality of the combustion. The increase in these emissions worsens the fuel economy as well as environmental pollution [56, 57]. Fig. 8 shows what happens to HC emissions when the ratio of H_2 energy and the start of H_2 input is changed.

Fig. 8 shows that increasing the HER resulted in a considerable drop in HC emissions. When the hydrogen injection timing was evaluated, increasing the time prevented the increase in HC emissions to some extent.

The NO emissions induced by high cylinder temperatures rise in tandem with the improvement in combustion quality [58-60]. The influence of HER and H_2 injection commencement on NO emissions is seen in Fig. 9. As can be seen in Fig. 9, the addition of H_2 resulted in an increase in the amount of NO emissions. Nevertheless, bringing the HER up to 20% mitigated the impact of the rise in NO emissions. The primary cause of this condition is that the high H_2 ratio decreases volumetric efficiency and worsens combustion. The maximum rate of increase in NO emissions was determined when the H_2 injection was set at 30 °CA aTDC.

Petroleum-derived fuels consist of H_2 and carbon.

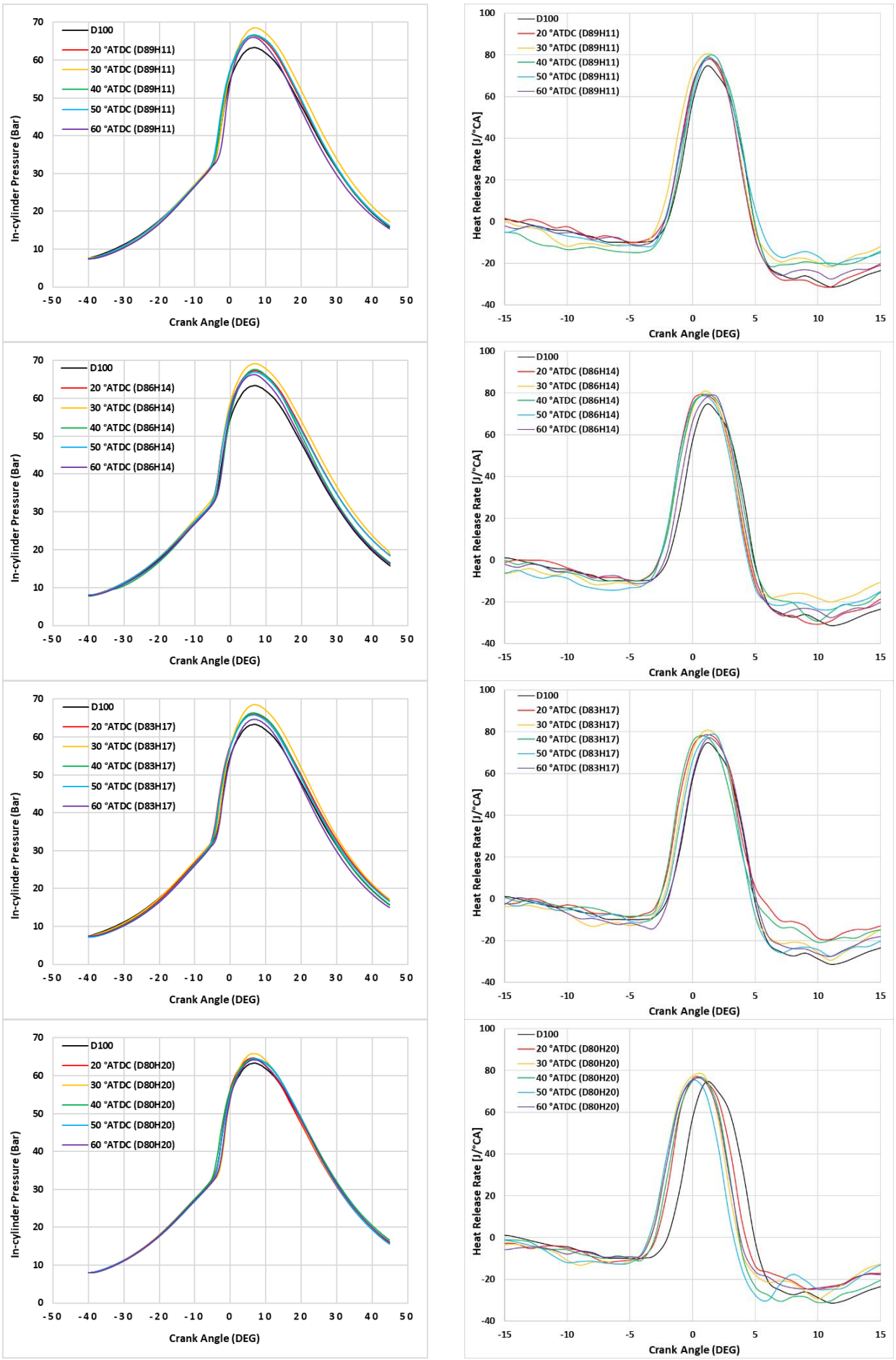

Fig. 6. Cylinder pressure and HRR resulting from H_2 energy rate and injection timing.

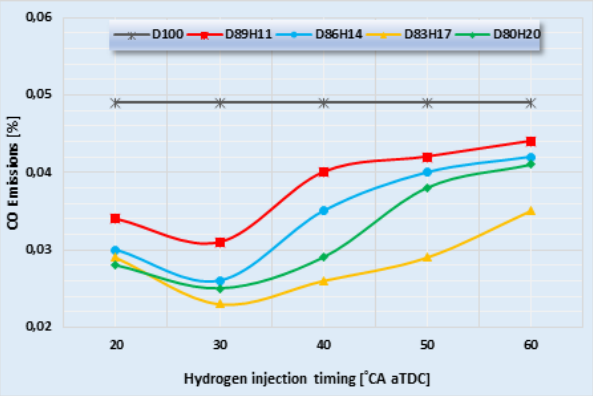

Fig. 7. CO emissions resulting from H_2 energy rate and injection timing.

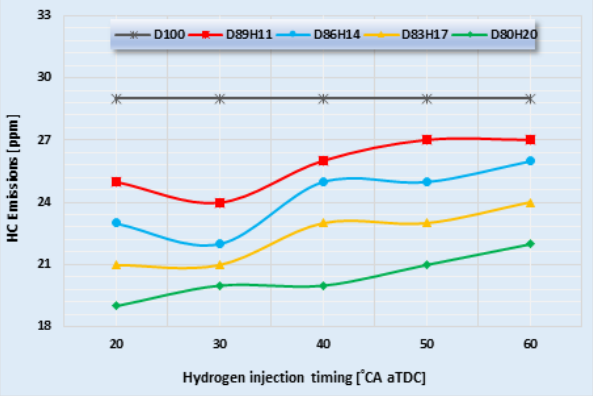

Fig. 8. HC emissions resulting from H_2 energy rate and injection timing.

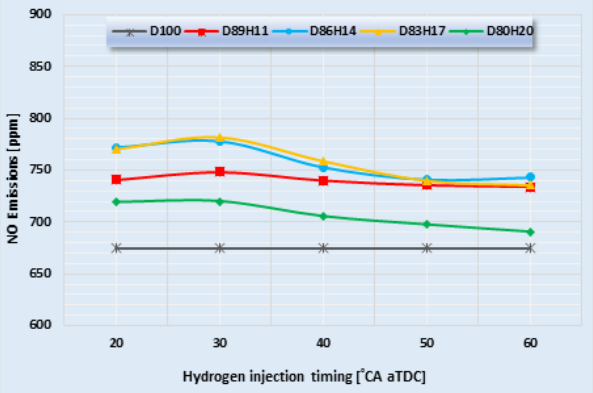

Fig. 9. NO emissions resulting from H_2 energy rate and injection timing.

The rapid combustion of H_2 with a high burning rate causes the carbon atoms to be deprived of oxygen, resulting in smoke [26, 61, 62]. Fig. 10 demonstrates how the ratio of H_2 energy and the timing of the start of H_2 injection impact smoke output.

The effectiveness of the HDDF mode in lowering smoke emissions may be noticed when Fig. 10 is reviewed. It was discovered that when the HER increased, the smoke emissions dropped. It was found that when H_2 injection was set at 30 °CA aTDC, the maximum reduction rate in smoke emissions was achieved.

Noise is undesirable in CI engines. The noise levels of these engines are quite high due to their high compression ratio [63]. Fig. 11 illustrates the impact of the HER and the timing of H_2 injection on noise emissions.

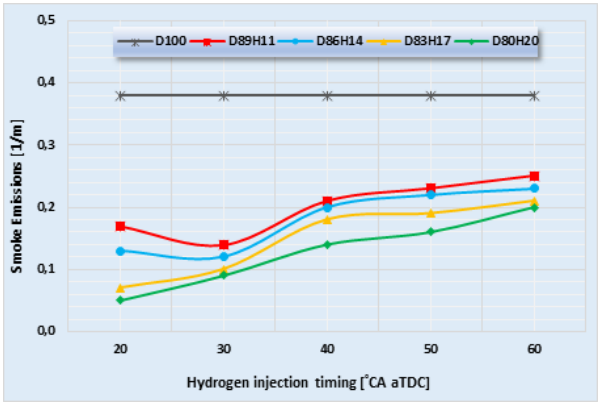

Fig. 10. Smoke emissions resulting from H_2 energy rate and injection timing.

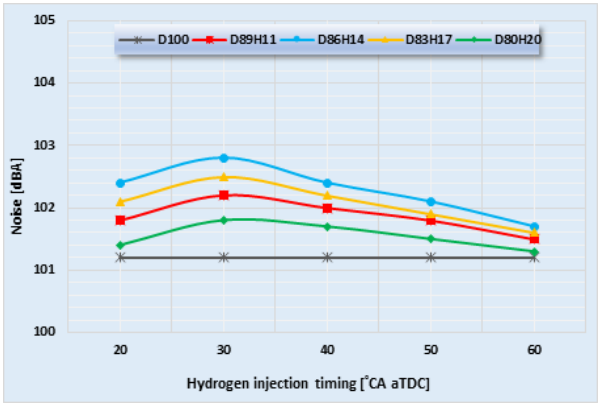

Fig. 11. Noise emissions resulting from H_2 energy rate and injection timing.

The introduction of H_2 resulted in an increase in the engine's noise levels. The reason for this situation can be shown by the increase in cylinder pressure [64]. The increments in the table are given in dBA. The highest increase was observed at 14% H_2 ratio and 30 °CA aTDC H_2 injection. In these test parameters, a 1.6 dBA increase in noise emissions was detected compared to D100 fuel.

The pressure created by the combustion in the engine causes vibration. The presence of a single-cylinder configuration in the test engine results in elevated levels of mechanical vibrations. Fig. 12 illustrates the impact of the HER and the timing of H_2 injection on mechanical vibrations.

With the addition of H_2, an increase in mechanical vibrations in the engine was seen. The most significant increase rate was

obtained when the H_2 ratio was set at 14% and the hydrogen injection timing at 30 °CA aTDC. In these test parameters, a 16.6% increase in mechanical vibrations was detected compared to D100 fuel. The in-cylinder pressure levels are the primary cause of these outcomes.

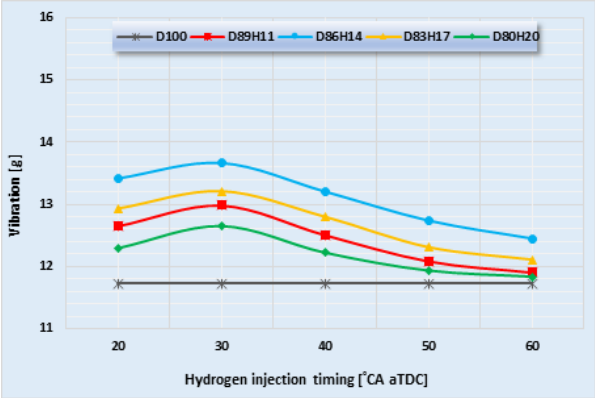

Fig. 12- Mechanical vibrations resulting from H_2 energy rate and injection timing.

4. Conclusions and recommendations

The following basic conclusions may be drawn from this study's investigation of the effects of HER and H_2 injection time on engine performance, exhaust, noise, and mechanical vibration emissions in an ECU-controlled HDDF system CI engine:

- HDDF mode reduces volumetric efficiency. Delaying the start of H_2 injection prevents this decrease to a certain extent.
- The thermal efficiency rose to 9.6% when the HER was adjusted to 14%. The amount of gain in thermal efficiency was reduced when the energy ratio was raised. Maximum thermal efficiencies were determined in experiments where the injection timing was 30 °CA aTDC.
- The dual fuel mode has positively affected BSEC. A decrease of 8.4% in BSEC was observed at a 14% H_2 ratio and an injection timing of 30 °CA aTDC.
- HRR and in-cylinder pressure have risen due to the usage of H_2. This increase is observed to be more effective up to a H_2 ratio of 14%. Because of the rise in H_2 ratio and the advancement of injection timing, in-cylinder pressure has increased and the maximum cylinder pressure point has approached TDC.
- It has been discovered that using H_2 may significantly lower emissions made up of carbon, such as CO, HC, and smoke. It has, however, increased noise, mechanical vibration, and NO emissions.
- It has been determined that the optimum H_2 injection timing for carbon-based emissions is 30 °CA aTDC.
- In the experiments, it was determined that bringing the H_2 injection timing to the open time of the exhaust valve causes kickback and jeopardizes combustion safety.
- The fact that the dual fuel system is ECU-controlled and can be programmed instantly contributed to obtaining high-quality test data and ensuring operational safety.
- In future studies, studies on engine modifications in HDDF mode will be beneficial.
- It is known that liquid and gas fuel pressures affect engine performance and emissions in the hydrogen-diesel dual fuel mode. Studies in this direction will contribute to the more efficient operation of dual fuel mode.

The operation of the gas fuel system with direct injection will help reduce the negative effect of hydrogen usage on volumetric efficiency.

Acknowledgments

The author would like to thank Selçuk University, Tokat Gaziosmanpaşa University and Karamanoğlu Mehmetbey University.

5. References

1. Polat S., "An experimental study on combustion, engine performance and exhaust emissions in a HCCI engine fuelled with diethyl ether–ethanol fuel blends", Fuel Processing Technology,143,140-50, 2016.
2. Cinar C., Uyumaz A., Solmaz H., Sahin F., Polat S., Yilmaz E., "Effects of intake air temperature on combustion, performance and emission characteristics of a HCCI engine fueled with the blends of 20% n-heptane and 80% isooctane fuels", Fuel Processing Technology,130, 275-81, 2015.
3. Gültekin N., Ciniviz M., "Experimental investigation of the effects of energy ratio and combustion chamber design on engine performance and emissions in a hydrogen-diesel dual-fuel CRDI engine", Atmospheric Pollution Research,102235, 1-12, 2024.
4. Gültekin N., Ciniviz M., "Examination

of the effect of combustion chamber geometry and mixing ratio on engine performance and emissions in a hydrogen-diesel dual-fuel compression-ignition engine", International Journal of Hydrogen Energy, 48, 2801-20, 2023.
5. Yang Y., Liu Z., Saydaliev H. B., Iqbal S., "Economic impact of crude oil supply disruption on social welfare losses and strategic petroleum reserves", Resources Policy, 77, 102689,2022.
6. Arabacı E., Öztürk Ş., Halis S.. "Simulation of the effects of valve timing misalignment on performance in spark ignition engines" Eng Perspect, 4, 47-53, 2024.
7. Cook P. J., "Resources and reserves in a carbon-constrained world", Mineral Economics, 35, 361-71, 2022.
8. Ediger V. Ş., "An integrated review and analysis of multi-energy transition from fossil fuels to renewables" Energy procedia,156, 2-6, 2019.
9. Shafiee S., Topal E., "An overview of fossil fuel reserve depletion time", 31st IAEE International Conference, Istanbul,. p. 18-20, 2008.
10. Kocakulak T., Uyumaz A., Arabacı E., Dağoğlu Y., Çamoğlu C., "Experimental Investigation of the Effects of Gasoline-Methyl Ethyl Ketone Fuel Blends on Engine Performance and Exhaust Emissions", Journal of Materials and Mechatronics: A., 4, 397-408, 2023.
11. Demir U., Çelebi S., Özer S., "Experimental investigation of the effect of fuel oil, graphene and HHO gas addition to diesel fuel on engine performance and exhaust emissions in a diesel engine", International Journal of Hydrogen Energy, 52, 1434-46, 2024.
12. Koçyiğit S., Özer S., Çelebi S., Demir U., "Bio-based solutions for diesel engines: Investigating the effects of propolis additive and ethanol on performance and emissions", Thermal Science and Engineering Progress, 48,102421, 2024.
13. Kumar C. B., Lata D., "Effect of di-tert butyl peroxide (DTBP) on combustion parameters and NOx in dual fuel diesel engine with hydrogen as a secondary fuel", International Journal of Hydrogen Energy, 46, 4507-25, 2021.
14. Çelebi S., Kocakulak T., Demir U., Ergen G., Yilmaz E., "Optimizing the effect of a mixture of light naphtha, diesel and gasoline fuels on engine performance and emission values on an HCCI engine.", Applied Energy, 330, 120349, 2023.
15. Liu X., Srna A., Yip H.L., Kook S., Chan Q.N., Hawkes E.R., "Performance and emissions of hydrogen-diesel dual direct injection (H2DDI) in a single-cylinder compression-ignition engine", International Journal of Hydrogen Energy, 46,1302-14, 2021.
16. Uludamar E., Yıldızhan Ş., Aydın K., Özcanlı M., "Vibration, noise and exhaust emissions analyses of an unmodified compression ignition engine fuelled with low sulphur diesel and biodiesel blends with hydrogen addition", International journal of hydrogen energy, 41, 11481-90, 2016.
17. Zhang Z., Lv J., Xie G., Wang S., Ye Y., Huang G., "Effect of assisted hydrogen on combustion and emission characteristics of a diesel engine fueled with biodiesel.", Energy, 254, 124269, 2022.
18. Akcay M., Yilmaz I.T., Feyzioglu A., "The influence of hydrogen addition on the combustion characteristics of a common-rail CI engine fueled with waste cooking oil biodiesel/diesel blends" Fuel Processing Technology, 223, 106999, 2021.
19. Lee C-f., Pang Y., Wu H., Hernández J.J., Zhang S., Liu F., "The optical investigation of hydrogen enrichment effects on combustion and soot emission characteristics of CNG/diesel dual-fuel engine", Fuel, 280,118639, 2020.
20. Elsemary I.M., Attia A.A., Elnagar K.H., Elaraqy A.A., "Experimental investigation on performance of single cylinder spark ignition engine fueled with hydrogen-gasoline mixture", Applied Thermal Engineering,106, 850-4, 2016.
21. Köse H., Ciniviz M., "An experimental investigation of effect on diesel engine performance and exhaust emissions of addition at dual fuel mode of hydrogen", Fuel processing technology, 114, 26-34, 2013.
22. Qi D., Chen H., Geng L., Bian Y., "Effect of diethyl ether and ethanol additives on the combustion and emission characteristics of biodiesel-diesel blended fuel engine",

Renewable energy, 36, 1252-8, 2011.
23. Akçay M., Yılmaz İ.T., Feyzioğlu A., Salih Ö., "Sıkıştırma ile Ateşlemeli Bir Motora Hidrojen İlavesinin Egzoz Emisyonlarına Etkisi", Çukurova Üniversitesi Mühendislik-Mimarlık Fakültesi Dergisi, 34, 21-34, 2019.
24. Ciniviz M., Köse H., "Hydrogen use in internal combustion engine: a review", International Journal of Automotive Engineering and Technologies,1,1-15, 2012.
25. De Morais A.M., Justino MAM., Valente O.S., de Morais Hanriot S., Sodré J.R., "Hydrogen impacts on performance and CO2 emissions from a diesel power generator", international journal of hydrogen energy, 38, 6857-64, 2013.
26. Wu H-W., Wu Z-Y., "Investigation on combustion characteristics and emissions of diesel/hydrogen mixtures by using energy-share method in a diesel engine", Applied Thermal Engineering, 42, 154-62, 2012.
27. Koten H., "Hydrogen effects on the diesel engine performance and emissions", International journal of hydrogen energy, 43, 10511-9, 2018.
28. Wongchai B., Visuwan P., Chuepeng S., "The vibration analysis of diesel engine with hydrogen-diesel dual fuel", American Journal of Applied Sciences,10, 8-14, 2013.
29. Barelli L., Bidini G., Buratti C., Mariani R., "Diagnosis of internal combustion engine through vibration and acoustic pressure non-intrusive measurements" Applied Thermal Engineering, 29, 1707-13, 2009.
30. Nag S., Dhar A., Gupta A., "Hydrogen-diesel co-combustion characteristics, vibro-acoustics and unregulated emissions in EGR assisted dual fuel engine", Fuel, 307, 1219-25, 2022.
31. Nag S., Sharma P., Gupta A., Dhar A., "Combustion, vibration and noise analysis of hydrogen-diesel dual fuelled engine" Fuel, 241, 488-94, 2019.
32. Barelli L., Bidini G., Buratti C., Mariani R., "Diagnosis of internal combustion engine through vibration and acoustic pressure non-intrusive measurements" Appl Therm Eng.,29, 2009.
33. Gültekin N., Gülcan H.E., Ciniviz M., "The impact of hydrogen injection pressure and timing on exhaust, mechanical vibration, and noise emissions in a CI engine fueled with hydrogen-diesel" International Journal of Hydrogen Energy, 78, 871-8, 2024.
34. Gültekin N., Gülcan H.E., Ciniviz M., "Investigation of the effects of hydrogen energy ratio and valve lift amount on performance and emissions in a hydrogen-diesel dual-fuel compression ignition engine", International Journal of Hydrogen Energy, 49, 352-66, 2024.
35. Yilmaz I., Gumus M., "Effects of hydrogen addition to the intake air on performance and emissions of common rail diesel engine", Energy,142,1104-13, 2018.
36. Sharma P., Dhar A., "Effect of hydrogen supplementation on engine performance and emissions", International Journal of Hydrogen Energy, 43, 7570-80, 2018.
37. Qin Z., Yang Z., Jia C., Duan J., Wang L., "Experimental study on combustion characteristics of diesel–hydrogen dual-fuel engine", Journal of Thermal Analysis and Calorimetry, 142, 1483-91, 2020.
38. Geo V.E., Nagarajan G., Nagalingam B., "Studies on dual fuel operation of rubber seed oil and its bio-diesel with hydrogen as the inducted fuel", International journal of hydrogen energy, 33, 6357-67, 2008.
39. Chintala V., Subramanian K., "A comprehensive review on utilization of hydrogen in a compression ignition engine under dual fuel mode", Renewable and Sustainable Energy Reviews, 70, 472-91, 2017.
40. Saravanan N., Nagarajan G., Sanjay G., Dhanasekaran C., Kalaiselvan K., "Combustion analysis on a DI diesel engine with hydrogen in dual fuel mode", Fuel, 87, 3591-9, 2008.
41. Saravanan N., Nagarajan G., "Experimental Investigation in Optimizing the Hydrogen Fuel on a Hydrogen Diesel Dual-Fuel Engine", Energy & Fuels, 23, 2646-57, 2009.
42. Talibi M., Hellier P., Morgan R., Lenartowicz C., Ladommatos N., "Hydrogen-diesel fuel co-combustion strategies in light duty and heavy duty CI engines", international journal of hydrogen energy, 43, 9046-58, 2018.
43. Karagöz Y., Güler İ., Sandalcı T., Yüksek L., Dalkılıç A.S., "Effect of hydrogen enrichment on combustion characteristics,

emissions and performance of a diesel engine", International journal of hydrogen energy, 41, 656-65, 2016.
44. Chong C.T., Hochgreb S., "Measurements of laminar flame speeds of liquid fuels: Jet-A1, diesel, palm methyl esters and blends using particle imaging velocimetry (PIV)", Proceedings of the Combustion Institute, 33, 979-86, 2011.
45. Wu Y., Devi P.B., Anbarasu A., Sołowski G., Chanh H.C., Chi N.T.L., "Estimation of the engine performance and emission characteristics of hydrogen feed vehicles with modified injection fuel system", Fuel, 329,125339, 2022.
46. Thiyagarajan S., Varuvel E., Karthickeyan V., Sonthalia A., Kumar G., Saravanan C., "Effect of hydrogen on compression-ignition (CI) engine fueled with vegetable oil/biodiesel from various feedstocks: A review", International Journal of Hydrogen Energy, 47, 37648-37667, 2022.
47. Dinesh M., Kumar G., "Effects of compression and mixing ratio on NH3/H2 fueled Si engine performance, combustion stability, and emission", Energy Conversion and Management: X,15,100269, 2022.
48. Arslan E., Kahraman N., "The effects of hydrogen enriched natural gas under different engine loads in a diesel engine", International Journal of Hydrogen Energy, 47,12410-20, 2022.
49. Dam Q.T., Haidar F., Mama N., "Chennapalli SJ. Modeling and simulation of an Internal Combustion Engine using Hydrogen: A MATLAB implementation approach" Engıneerıng Perspectıve,108, 2024.
50. Demir U., Coskun G., Soyhan H.S., Turkcan A., Alptekin E., Canakci M., "Effects of variable valve timing on the air flow parameters in an electromechanical valve mechanism–A cfd study" Fuel, 308, 121956, 2022.
51. Gülcan H.E., Gültekin N., Ciniviz M., "The Effect of Methanol-Dodecanol Addition on Performance and Smoke Emission in a CI Engine with Diesel Fuel", International Journal of Automotive Science And Technology, 6,207-13, 2022.
52. Ji C., Wang S., "Effect of hydrogen addition on the idle performance of a spark ignited gasoline engine at stoichiometric condition", International journal of hydrogen Energy, 34, 3546-56, 2009.
53. Nag S., Sharma P., Gupta A., Dhar A., "Experimental study of engine performance and emissions for hydrogen diesel dual fuel engine with exhaust gas recirculation", International Journal of Hydrogen Energy, 44, 12163-75, 2019.
54. Rocha H.M.Z., da Silva Pereira R., Nogueira M.F.M., Belchior C.R.P., de Lima Tostes M.E., "Experimental investigation of hydrogen addition in the intake air of compressed ignition engines running on biodiesel blend", International Journal of Hydrogen Energy, 42, 4530-9, 2017.
55. Sarıkoç S., Ünalan S., Örs İ., "Experimental study of hydrogen addition on waste cooking oil biodiesel-diesel-butanol fuel blends in a DI diesel engine", BioEnergy Research, 12, 443-56, 2019.
56. Pitchamuthu G., Gokulnath R., "Effect of additives on emissions of DI CI engine fuelled with algae/Mangifera indica blends" International Journal of Ambient Energy, 28, 1-7, 2020.
57. Gültekin N., "Experimental study of the effects of diesel, bioethanol, and hydrogen on combustion, emissions, mechanical vibration, and noise in a CI engine with different valve lift.", International Journal of Hydrogen Energy, 93, 1011-1021, 2024
58. Gülcan H. E., Ciniviz M., "The effect of pure methane energy fraction on combustion performance, energy analysis and environmental-economic cost indicators in a single-cylinder common rail methane-diesel dual fuel engine", Applied Thermal Engineering, 230, 1207-12, 2023.
59. Örs İ., Sarıkoç S., Atabani A., Ünalan S., "Experimental investigation of effects on performance, emissions and combustion parameters of biodiesel–diesel–butanol blends in a direct-injection CI engine" Biofuels,11,121-34, 2020.
60. Gürbüz H., "Optimization of combustion and performance parameters by intake-charge conditions in a small-scale air-cooled hydrogen fuelled SI engine suitable for use in piston-prop aircraft", Aircraft Engineering and Aerospace Technology, 93, 448-456, 2021.
61. Asokan M., Prabu S.S., Akhil V.S.,

Bhuvan P.S., Reddy Y.B., "Performance and emission behaviour of diesel and blends of watermelon seed oil biodiesel in direct injection diesel engine", Materials Today: Proceedings, 45, 3274-8, 2021.
62. Kumar V., "Experimental investigation of piston bowl geometry effects on performance and emissions characteristics of diesel engine at variable injection pressure and timings", International Journal of Ambient Energy, 39, 685-93, 2018.
63. Gültekin N., Mayda M., "Investigation of effects of spark plug gap on vibration, noise and HC emission in a gasoline engine", Int J Energy Appl Technol., 5.1, 56-60, 2018.
64. Gültekin N., Ciniviz M., "Investigation of the effect of advance angle on performance and emissions (exhaust, vibration, noise) in a single-cylinder diesel engine whose fuel system is converted to common rail", Environmental Progress & Sustainable Energy, 43, e14261, 2024.